Structure and Optical Properties of Complex Aggregate-Structures of Amphiphilic Dye-Systems

DISSERTATION

Zur Erlangung des akademischen Grades doctor rerum naturalium
(Dr. rer.-nat.) im Fach Physik
eingereicht an der

Mathematisch-Naturwissenschaftliche Fakultät I
der Humboldt-Universität zu Berlin
von

Dipl.-Phys. Omar Al-Khatib

Präsident der Universität: Prof. Dr. Jan-Hendrik Olbertz

Dekan der Fakultät: Prof. Dr. Elmar Kulke

Gutachter/in: 1. Dr. Stefan Kirstein

2. Prof. Dr. Matthias Ballauf

3. Prof. Dr. Regine von Klitzing

Tag der mündlichen Prüfung: 13.09.2012

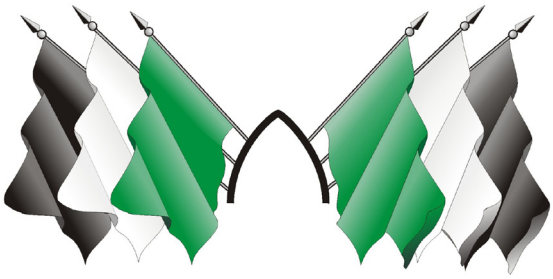

Zusammenfassung

In dieser Arbeit werden Untersuchungen an selbstorganisierten, tubulären J-Aggregaten amphiphiler Cyaninfarbstoffe, 3,3'-bis(2-sulfopropyl)-5,5',6,6'-tetrachloro-1,1'-dioctylbenzimidacarbocyanine, im Weiteren C8S3 genannt, dargestellt. Ziel der Arbeit ist es an die Aggregate eine Lage Polyelektrolyte zu adsorbieren, sowie nachzuweisen, dass diese Methode geeignet ist, um einen Energietransfers zwischen dem Aggregat und funktionellen Gruppen in der Adsorbatschicht zu erreichen.

Die tubulären Aggregate sind supramolekulare Strukturen, die sich spontan und selbstorganisiert aufgrund des amphiphilen Charakters der Cyaninfarbstoffe in wässrigen Lösungen bilden. Die Farbstoffe in den Wänden der Röhre ordnen sich in einer Art Doppelschicht an, die die Wand der röhrenförmigen Struktur bildet, wobei der gesamte Durchmesser der Röhre etwa 13 nm beträgt und die Längen mitunter 1 µm übersteigen. Die Farbstoffe bilden aufgrund der regelmäßigen und dichten Packung exzitonische Anregungen, die sich in einer typischen Rotverschiebung (J-Aggregat) der optischen Absorption sowie einer charakteristischen Aufspaltung in mehrere schmale Banden zeigt.

Aufgrund des amphiphilen Charakters der Farbstoffe besitzen die Aggregate in wässriger Lösung eine negative Oberflächenladung. Analog zu kolloidalen Systemen, wird dies genutzt um an die Aggregate durch elektrostatische Adsorption entgegengesetzt geladene Polyelektrolyte (PE) anzulagern. Dies wird exemplarisch für drei verschiedene PE gezeigt, die sich durch ihre Ladungsdichte als auch durch die mechanische Persistenzlänge unterscheiden. In allen drei Fällen ist es gelungen Aggregate mit einer 2-3 nm dicken Polyelektrolytschicht zu umhüllen, wobei, abhängig vom molaren Verhältnis der Polyelektrolyte im Vergleich zum Farbstoff, die Aggregate nur teilweise umhüllt werden. Die molekulare Ordnung der Aggregate wird durch die Adsorption der PE nicht oder nur geringfügig (bei PAH) gestört, was auf eine sehr lose, elektrostatische Bindung schließen lässt. Eine Umhüllung mit sehr gleichmäßiger Schichtdicke, aber nur stückweise entlang der Aggregate, ergibt sich für das PDADMAC, während PEI eine sehr unregelmäßig geformte Schicht und Vernetzungen zwischen einzelnen Aggregaten ausbildet. Eine optimale Umhüllung wurde für PAH gefunden, welches eine gleichmäßig dünne Schicht von ca. 2 nm

ausbildet. Mittels Mikroelektrophorese konnte gezeigt werden, dass die Adsorption der Polykationen zu einer Umladung der Oberfläche führt.

Durch Einsatz von Farbstoffdotierten Polyelektrolyten konnten Experimente zum Nachweis des Förster-Energietransfer durchgeführt werden. Die Farbstoffdotierungen sind kovalent an die PE gebunden, wodurch sie in der PE-Umhüllung lokalisiert sind. Durch Wahl geeigneter Farbstoffe konnte ein Energietransfer vom Farbstoff (Donator) zum Aggregat als auch umgekehrt vom Aggregat zum Farbstoff (Akzeptor) nachgewiesen werden. Aufgrund der Lokalisierung der Farbstoffe innerhalb der PE Schicht sind die typischen Abstände stets kleiner als die theoretisch berechneten Förster-Radien, wodurch sich eine hohe Effizienz für die Transferraten ergibt. Unter Berücksichtigung der verschiedenen Farbstoff-Dichten konnte keine nennenswerte Asymmetrie zwischen diesen beiden Experimenten gezeigt werden. Eine Asymmetrie hätte man erwartet, falls die elektronische Anregung in den Aggregaten stark delokalisert ist oder während der Anregungslebensdauer über weite Bereiche wandert. In dem Fall sollte die Transfereffizienz vom Aggregat zu einem lokalen Akzeptor deutlich erhöht sein gegenüber dem umgekehrten Fall.

Abstract

The following dissertation deals with investigation on tubular J-aggregates of amphiphile cyanine-dyes, 3,3'-bis(2-sulfopropyl)-5,5',6,6'-tetrachloro-1,1'-dioctyl-benzimidacarbocyanine (C8S3). Aim of this work is to adsorb a layer of polyelectrolyte on C8S3-aggregates and to proof the capability of this method to establish an energy-transfer between the aggregate and functional groups in the adsorbate-layer.

The tubular aggregates are supramolecular structures, that form entirely spontaneous and self-organized due to amphiphilic character of the investigated cyanine-dye derivative in aqueous solution. These dyes arrange themselves in a likewise double-layer, assembling the hull of the tubular structure, with outer tube-diameters of approximately 13 nm and length of more than 1 µm. Due to the regular and dense arrangement of the dyes excitonic excitation establishs with the structure, that causes a J-aggregate typical red-shift in absorption and a characteristic band-splitting.

The amphiphilic character of the dyes causes a negative surface-charge of the entire aggregates in aqueous solution. In analogy to colloidal systems this is utilized to adsorb oppositely charged polyelectrolytes (PE) by electrostatic adsorption. It is shown exemplarily for three different kinds of PE that differ in charge-density and persistence-length. In all three cases a successful PE-wrapping of 2-3 nm thickness has been performed. Depending on the molar ratio of PE related to the dye the aggregate is only partly wrapped. The molecular order within the aggregates has not been disturbed at all or only weakly, respectively, by the PE-adsorption, which indicates a loose, electrostatic binding. A wrapping with a homogeneous layer-thickness, but only part wise along the aggregate has been observed on PDADMAC-wrappings, whereas PEI provided very heterogeneous layers and interlinks between individual aggregates. The optimal coating was found with PAH attempts. The PAH-wrapping results in homogeneous thin layers of approximately 2 nm thickness. By means of microelectrophoresis it is shown, that the polycations overcompensate the aggregates surface-charge.

Dye-labelled PE experiments proof Förster-energytransfer. The dye-labels are covalently bound to PE, fixing and localizing the labels in the wrapping-layer. With appropriate dye-labels an energy-transfer from labels in the coating (donor) towards the aggregate and vice versa, from aggregate to the dye-labels (acceptor) has been

revealed. Caused by the localisation of the labels within the PE-coating, the distances of aggregate and label are always smaller than the theoretically calculated Förster-radii, resulting in a high efficiency of the transfer-rates. Considering the different label-densities, no significant difference in the transfer-directions has been observed. Such an asymmetry would indicate a strongly delocalised excitation of the aggregate or a delocalisation along vast areas during the excited-state lifetime. In this case the transfer-efficiency from aggregate towards a local acceptor would have been remarkably increased compared to the opposite case.

TABLE OF CONTENT

1 INTRODUCTION

„Aller Anfang ist leicht, und die letzten Stufen werden am schwersten und seltensten erstiegen.“

Every beginning is easy, the last steps are climbed hardest and hardly.

Johann Wolfgang von Goethe (1749-1832), german poet

In 1937 two chemists, Jelley and Scheibe, discovered independently from each other a new effect on cyanine dyes. A certain cyanine dye derivative, pseudo iso-cyanine or PIC, Figure 1-1, was used intensively in photography - a brand new research field in that time. Its ability as a light-sensitive oxidizer enforced the usage in photography development giving rise to further investigation [1]

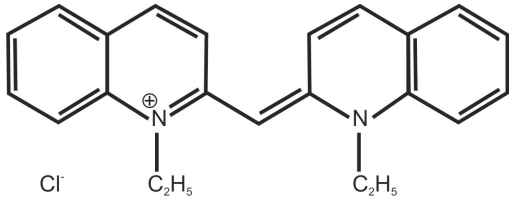

Figure 1-1:
Simplified sketch of pseudoisocyanine chloride (PIC).

This dye has been often stored in bottled solution. The dye causing the solution to have a characteristic color (orange-red) showed an interesting effect. Solutions of concentration above a certain level switched their color, see Figure 1-6. The color-shift could not be explained with simply intensification and therefore attracted attention. This obvious color-shift of the dye-solution was repeatable found when reaching a certain concentration of PIC [2,3,4,5,6,7]. The broad-banded monomer absorption located at around 525 nm wavelength was outpaced by an intense narrow absorption at 570 nm. This absorption band is called J- or S-band, after the mentioned chemists. The red-shift can be explained by the interaction of the transition-dipolemoment of each individual monomer in the theory of molecular excitons, known as Frenkel-excitons [8,9]. Red-shift and a narrow absorption band are characteristic for collective properties in J-bands [10,11,12,13,14,15,16].

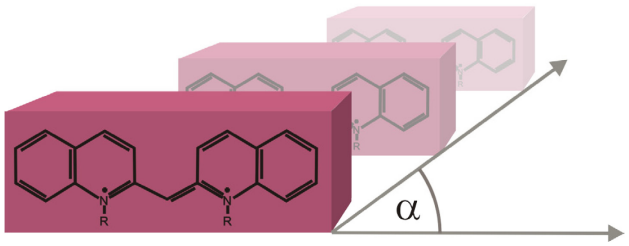

Figure 1-2:
Sketch of cyanine-dye dipole-stacking.

In solution the polarisable groundstate and the resulting van-der-Waals-forces lead to a self assembling aggregate. The resulting threads or sheets are one- or two-dimensional structures. The order in these sheets has been discussed as brick-layers and fish-bone-structures [17].

The color-shift is caused by the formation of a super-molecular structure within the solution. This structure forms under a self assembly process a very regular structure of threads, so called aggregates, see Figure 1-3.

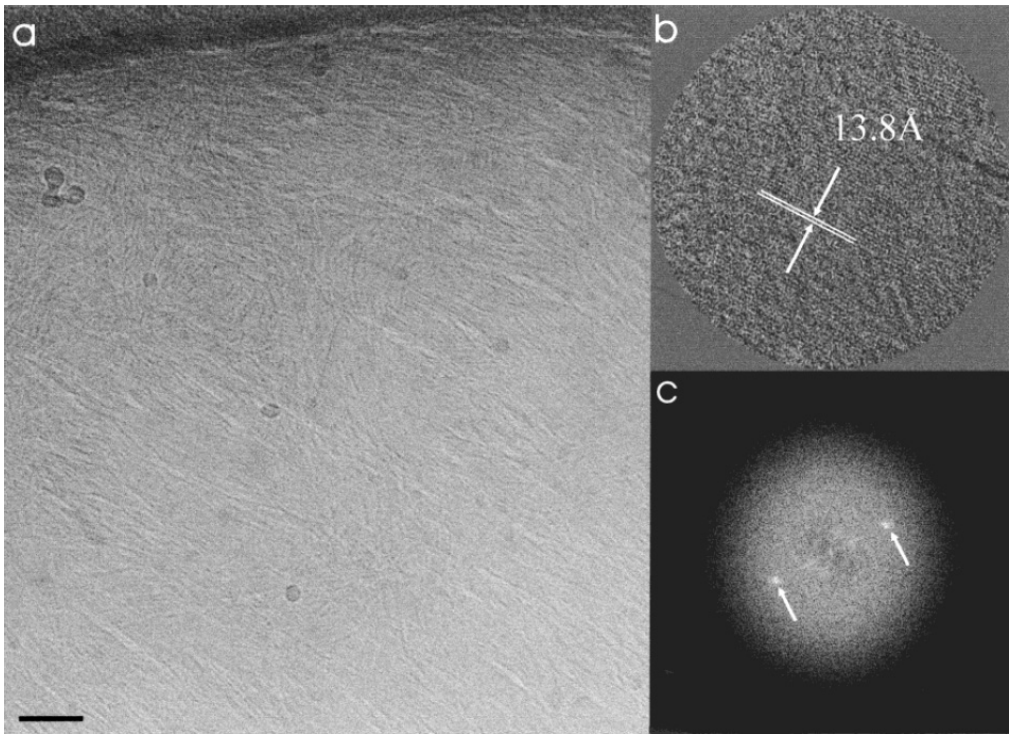

Figure 1-3:
a: Cryo-TEM image of a 30.0 x 10^{-3} mol/L aqueous PIC solution. The fibrous aggregates are closely packed, the fiber diameter is 2.3 nm. Bar = 50 nm.
b: Region of a cryo-TEM image of 30.0 x 10^{-3} mol/L aqueous PIC solution showing a pattern of fine parallel lines.
c: The Fourier transform taken from the line pattern in (b) gives a line repetition period of 13.8 Å. (taken from [17]).

Nowadays it is well accepted, that an energy-band is caused by extended electronic excitations [8,9]. In a PIC-aggregate and dye-aggregates in general the individual excited dyes combine to form Frenkel excitons. The overlap of all excited states leads to the characteristic absorption-band-shift [10,11,12,13,14,15,16]. In addition to that, these aggregates offer superradiation and energy migration.

The spectroscopic result of the aggregate is shown in Figure 1-4. Given spectra of PIC absorbance shows the characteristic red-shift and small-band absorption of a J-aggregate.

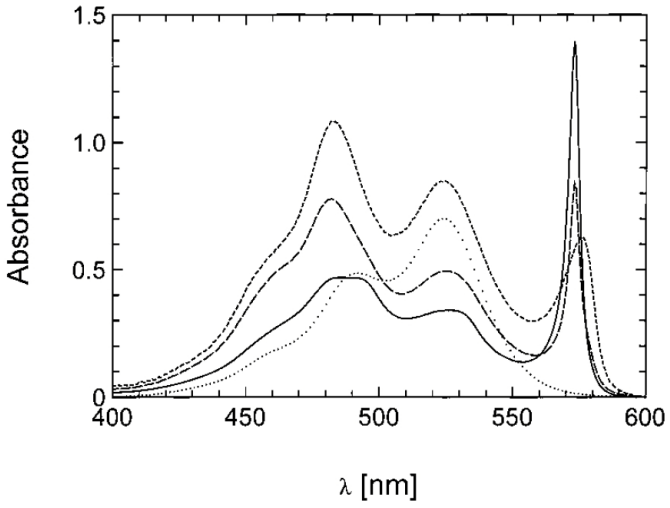

Figure 1-4:
Set of absorption spectra of PIC at various concentrations (taken from [17]) (dotted line) 2.35 x 10^{-5} M, (short dashed line) 2.82 x 10^{-3} M, (dashed line) 8.2 x 10^{-3} M, (solid line) 12.5 x 10^{-3} M.

Figure 1-4 shows the concentration-dependence of PIC-absorption. With increasing monomer-concentration the characteristic J-band peak increases. The assigned monomer-absorption declines with increasing monomer-concentration. The peak-position of the J-band is unaffected by the concentration.

1.1 Amphiphilic cyanine derivative (C8S3)

In the past 15 years J-aggregates of amphiphilic 5,5′,6,6′-benzimidacarbocyanines attracted much interest due to the discovery of their tubular structures [17]. Through the addition of polar and nonpolar side-chains to a cyanine-backbone the dye molecules gain an amphiphilic behavior in aqueous solution, enabling the formation of micellar structures [18,19]. Figure 1-5 illustrates the cyanine backbone and the positioning of the side-chains.

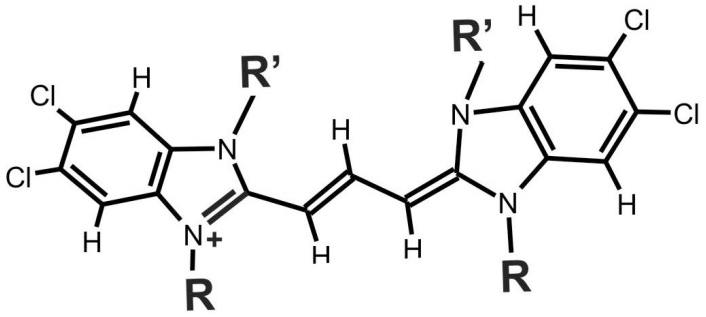

Figure 1-5:
Structure of cyanine dye, backbone with side-chains,
scheme of 5, 5', 6, 6'-tetrachlorobenzimidacarbocyanine.
R and R' indicate the 1, 1'- and 3, 3'-positions of the polar and nonpolar side-chains.

Table 1:
Side-chains of cyanine derivatives

R	R'	CounterIon	Abbrevation
C_2H_5	$(CH_2)_4SO_3^-$	Na^+	TDBC
C_8H_{17}	$(CH_2)_3COO^-$	Br^+	C8O3
C_8H_{17}	$(CH_2)_3SO_3^-$	Na^+	C8S3

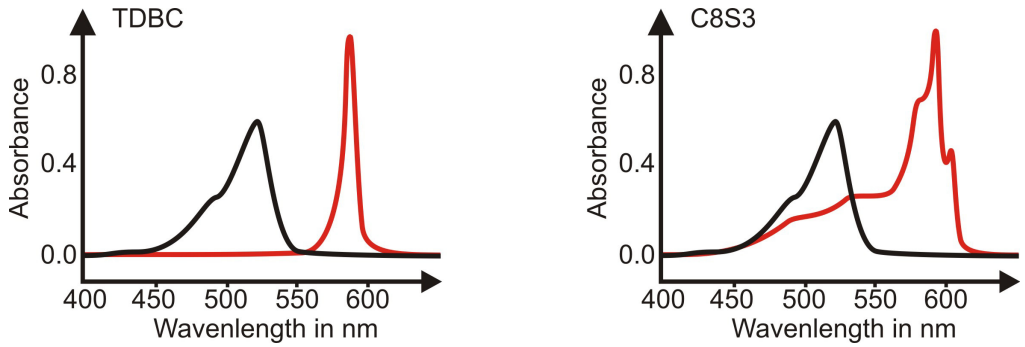

Figure 1-6:
Absorption spectra of TDBC and C8S3. Compared are monomer absorptions (black) and aggregates (red).

Among the many different derivatives of the surfactant dyes [20,21,22], two of them named with the abbreviation C8O3 and C8S3, see Figure 1-5 and Figure 1-6, are well investigated and known to form tubular aggregates [20,23]. Derivative C8O3 differs from C8S3 in type of hydrophilic side-chains (**R'**). The latter one, C8S3, is used throughout this work.

The C8S3 derivative is a zwitter-ionic surfactant, offering negative and positive charges at the same time. In aqueous solution the C8S3-molecules undergo the hydrophobic effect. This hydrophobic effect is known to force micelle formation of amphiphilic molecules such as surfactants.

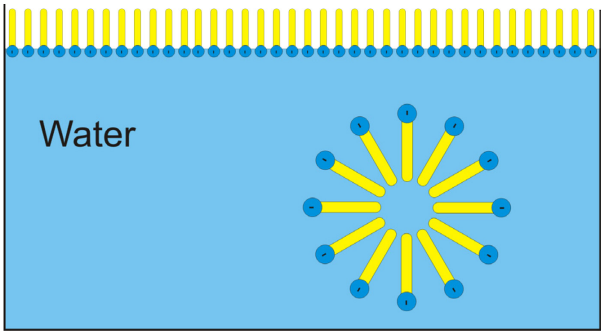

Figure 1-7:
Scheme of surfactant in water. Surfactants cover interfaces. i.e. air-liquid. Formation of micelles at higher concentration is enforced due to hydrophobic effect.

The polar side-chains are easily soluble in water, while the nonpolar side-chains repel from water [24]. If low concentrated, individual monomers are distributed at the surfaces of the aqueous phase, with the nonpolar chains pointing out of the water. Above a critical concentration the monomers are more and more driven into the volume, which causes the water to avoid the space around the nonpolar side-chains. This unfortunate increase of order among the water molecules is entropically unpropitious. More favorable is the formation of an ordered structure out of the amphiphilic molecules, causing the formation of micellar structures. These loosely bound supramolecular compounds hide the nonpolar side-chains from water and keep the water-molecules in disorder, see Figure 1-7. A smaller surface of nonpolar chains enables a larger entropy of the water.

The formation of micelles starts above certain monomer concentration in water, the critical micelle concentration (CMC). This concentration is dependent on the strength of the hydrophobic effect, which correlates with the length of the nonpolar chain.

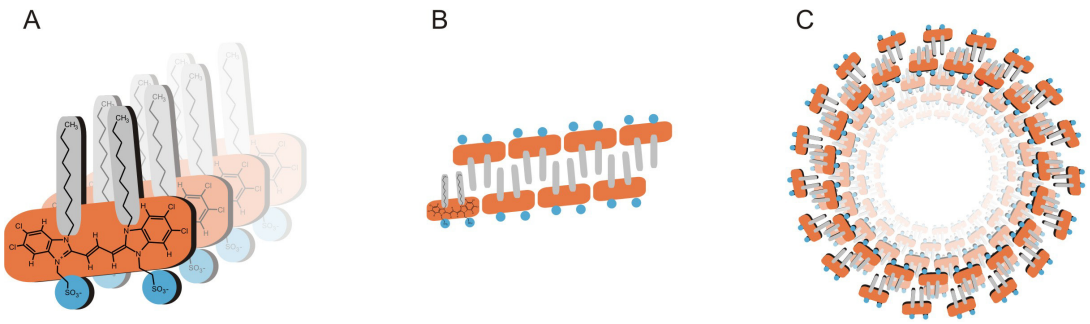

Figure 1-8:
Aggregation scheme of C8S3 to the formation of tubular aggregates.
A: Dipole-stacking due to dipole-dipole-attraction.
B: Formation of bi-layers due to hydrophobic forces.
C: Formation of double-walled tubes due to hydrophobic-forces bending bi-layers.

The hydrophobic effect is influencing the amphiphilic cyanine derivatives, too. First, the critical concentration to initiate the aggregate-formation on C8S3 is very low and starts at about 10^{-5} mol/l [25]. Second, the hydrophobic effect in combination with the structure of the dye molecule drives amphiphilic cyanine derivatives to form bi-layered structures. Obviously any edges of such bilayers are energetically very unfavourable and these bi-layers wrap into a double-walled tube. Actually, the proper mechanism of the tube formation is still under discussion. Another reasonable explanation could be bending of the double layers due to a sterically preferred curvature ending up in hollow tubes. In any case, the hydrophobic effect is forcing the formation of a tube with a double wall of dye molecules, where the polar groups point towards the outer side and towards the inner part, while the nonpolar side-chains are covered by the dyes. A sketch of such a structure is given in Figure 1-8 and Figure 1-9, respectively. As shown in Figure 1-10, the tubular structure is observable in cryo-TEM [26].

The resulting tubes show a constant diameter of about 13 nm and reach lengths exceeding 1 µm. The diameter has been found to be stable and reproducible. However, it is important to note, that the diameter changes upon variation of the volume fraction of alcohol in the aggregate solution [27,28].

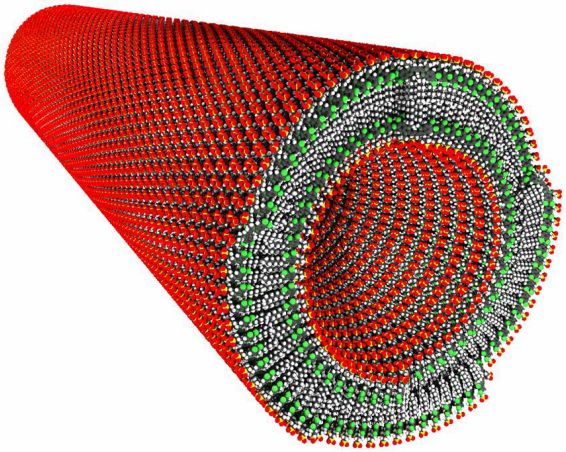

Figure 1-9:
3D-model of tubular C8S3-aggregate, taken from [29]. The model shows the double-wall, the inner and outer surface, both covered with sulfur-groups, and the multi-helical arrangement of the hollow tube.

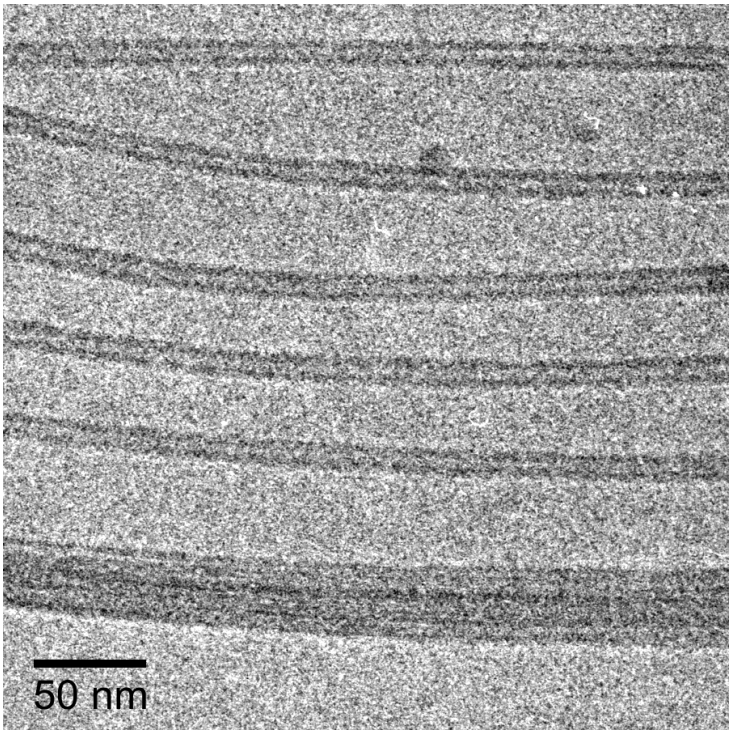

Figure 1-10:
Cryo-TEM image of vitrified C8S3-aggregates in aqueous solution.

Figure 1-10 shows C8S3 aggregates in vitrified solution. The image shows individual aggregates and a single aggregate-bundle in the lower region. The structure-formation leads to very significant and typical spectroscopical changes, as to be seen in the Figure 1-11.

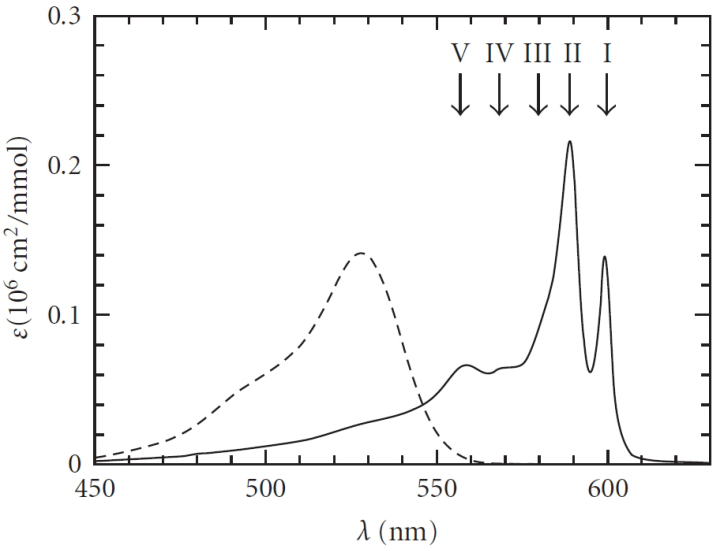

Figure 1-11:
Absorption spectra of C8S3. Dashed line shows the monomer-absorption, solid line shows the aggregate absorption ([c] = 6 X 10^{-5} M, taken from [20]).

The spectra, shown in Figure 1-11, show the monomer absorption in the dashed line and the aggregate absorption for monomer-concentration above the CMC in the solid line. This comparison reveals the former mentioned spectral shift due to formation of J-aggregates. In contrast to PIC aggregates, the spectra of the tubular J-aggregates show two major peaks (marks I and II in Figure 1-11). This double-peak is characteristic for the double-walled tubes [29]. Each wall of the double-tube provides one of these J-band transitions [30].

1.2 Functionalization of aggregates

At present time there are several attempts to utilize the C8S3-aggregates as templates for further growth of complex nanostructures. As an example one may mention the usage of the tube-structure as a template for the growth of ultrathin silver-nanowires within the aggregates [31].

The double-walled aggregates themselves are regular and well-defined structures. The surface on the outer and inner wall is covered with a large number of negative charges, provided by the polar sulfur-groups of C8S3. In other words, the aggregate is a nano-scaled, cylindrical, hollow structure of known diameter with a large number of equally distributed negative surface charges. Therefore the aggregate can be utilized as a microscopic template.

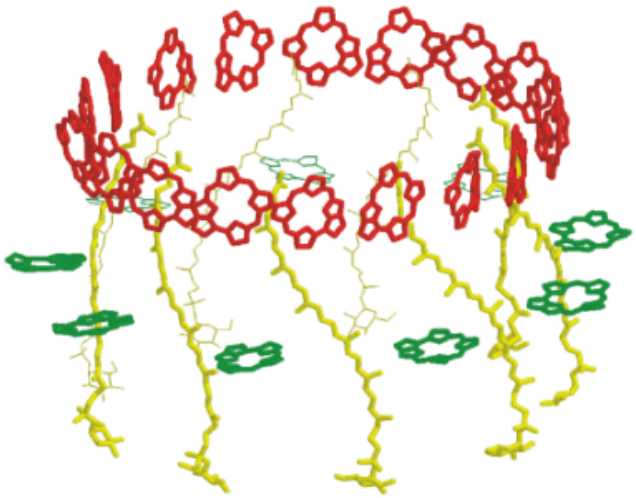

Figure 1-12:
The photoactive part of the light harvesting antenna complex, LH2, found in the purple bacterium *Rhodobacter sphaeraides*, which consist of two (BChl) ring systems, with 18 and 9 units (red and green rings, respectively) and 9 carotenoid molecules (yellow strings). The individual chromophores are confined in the shown geometry by the surrounding protein (not shown here) (Image taken from [32]).

The motivation of this work is based on the outstanding light-harvesting and energy-conducting properties of the J-aggregates. With addition of donor and/or acceptors to the aggregate-structure it ought to be possible to extend the optical absorption and emission beyond the limitations of the C8S3 J-bands [33,34]. To establish such a spectral extension it is necessary to provide an excitation energy-transfer between the aggregate and its functionalization. The latter ought to be dyes spectrally complement to the aggregate. While the functionalization labels, or antennas, are

only capable of light emission or absorption, the aggregate itself could provide the additional ability of energy migration along the structure. Such a combination of antenna-groups and energy conducting-structures is well known in biology. The photosynthesis of the purple bacteria for instance, is a 3-step-process, see Figure 1-12. Antenna-groups collect sunlight and deliver the collected energy to a conductor-ring, which is pumping a reaction-center, where the energy is finally converted into the desired product (collecting, conducting, converting). This is of course a crude simplification. Processes within plants or bacteria are very complex. From this point of view, the aimed functionalization is a biomimetic attempt [35]. The conducting-ring in the purple-bacteria consists of less than 20 molecules and fits the boundary-conditions of a ring-aggregate, whereas the C8S3-aggregate is a linear supramolecular structure in the order of a micrometer length, consisting of many 10 000 molecules. The comparison is therefore only partly valid. Both systems separate light-collection, energy-conduction and energy-conversion into different groups.

1.3 Challenges of functionalization

The well-ordered aggregate structure is very intolerant against direct implementation of other functional groups. For example, dyes placed directly into the well-ordered structure of the aggregate would lead to disorder within the tube and therefore disturb the optical properties and the energy-migration ability. An important advantage of the aggregates would be canceled.

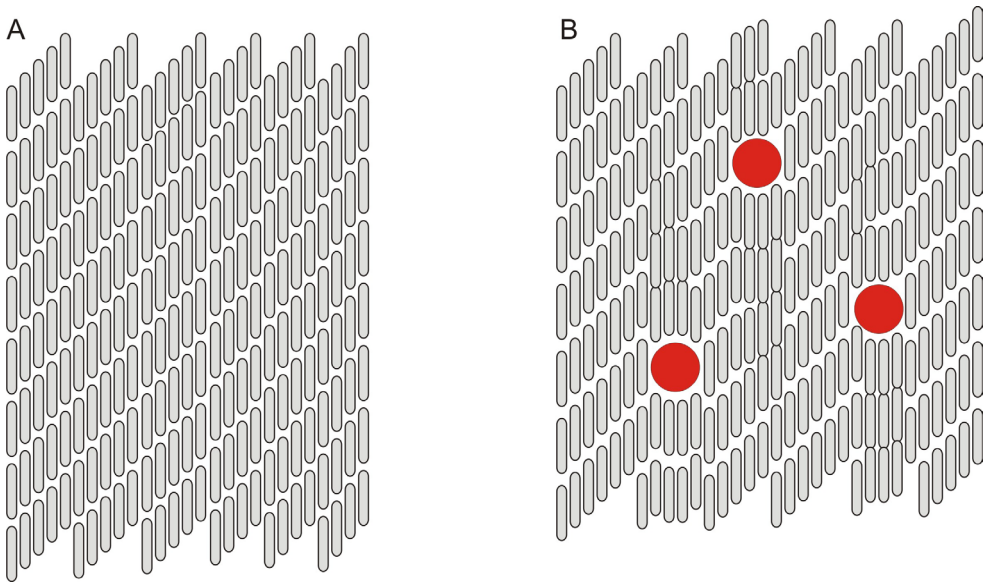

Figure 1-13:
Sketched order and disorder of molecular dipoles in aggregate walls.
A: Ordered structure, individual dipoles arranged under a certain distance and angle to neighbor.
B: Disorder induced by insertion of foreign modules (i.e. functional dyes). Variation of brick-size causes irregular displacement.

This disorder takes place in any case of mounting a foreign molecule within the well-ordered aggregate. While C8S3-monomers are brick-like arranged in the aggregate, each brick equals it's neighbors in size, polarisability, density and strength of the hydrophobic effect. Any insertion of bricks with deviating properties leads to displacement in the aggregate order. This structural fragility of the tubular aggregates was demonstrated by mixing of C8S3 with the only slightly different derivative C8S2 [36]. Significant changes in structure and spectra are, even for large excess of C8S3 observed. This shows that insertion of only slightly structural incompatible dyes leads to new structures with different spectra [36].

Another disadvantage of direct insertion of functional groups is the principally unknown distribution within the aggregate wall. It is unknown how much of the dye inserts and it is unknown if it is homogeneously distributed or if it separates into

larger clusters. The dyes differ from C8S3 in size, density, and solubility, which tends to drive functional dyes and C8S3-aggregates into a heterogeneous solution.
To bypass these problems the functional groups shall be attached on the outside of the aggregate while maintaining the well-ordered tubular structure. Therefore it is necessary to apply a suitable linker that is binding the functional groups loosely to the aggregate without disturbing the aggregate structure and its energy-migration ability. However, without a close connection between the aggregate and the dye-labels no energy-transfer via charge-migration is possible. The best suitable transfer mechanism that acts over longer distances of a few nanometers is Förster's resonant-energy-transfer (FRET). This mechanism is based on resonant coupling of donor-emission and acceptor-absorption and does require at least a small spectral overlap.

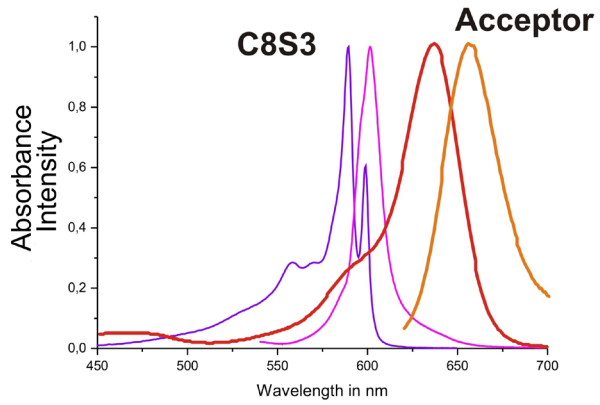

Figure 1-14:
Donor- and acceptor spectra of absortpion and emission. In this figure, the aggregate is depicted as donor (pink: C8S3 absorption, violet: C8S3 fluorescence). Acceptor is overlapping on the longer wavelengths, red side (red: acceptor-absorption, orange: acceptor-emission).

Figure 1-14 shows an exemplary composition of the aggregate and an arbitrary acceptor molecule. The aggregate in this figure acts as the donor and the donor-emission and acceptor-absorption show an overlap. In the same way, the aggregate may be used as an acceptor. In that case, the donor has to be blue-shifted to the aggregate, but providing again an overlap between donor-emission and aggregate-absorption.

1.4 Wrapped and functionalized aggregates

A possible linker between aggregate and functional-groups that maintains the well-defined tube-order is provided by a shell of a coating-layer. Such a coating provides fixed donor- or acceptor-molecules in proximity to the aggregate. The donor- or acceptor-concentration on the aggregate is given by the dye concentration within the coating-layer.

A remarkably adaptable approach, termed the layer-by-layer (LbL) self-assembly technique has been applied for coating of colloids. The basis of this method is the electrostatic association between alternately deposited, oppositely charged species. This technique enables coatings on nano-particles of various size and shape [37,38]. The surface charge of coated particles is dominated by the outermost polyelectrolyte [39].

The negative surface charge of the aggregates enables electrostatically driven adsorption of polycations [40,41,42,43] and hence becomes an important step in between the uncoated aggregates and the aimed functionalization, see Figure 1-15. Wrapping of the aggregates with polycations gives rise to utilization of the polycation-coating, because these polyelectrolytes easily can be labelled (doped) with various dye molecules. As long as the underlying aggregate-structure is maintained, the coating layer is appropriate for anchoring the dye-labels.

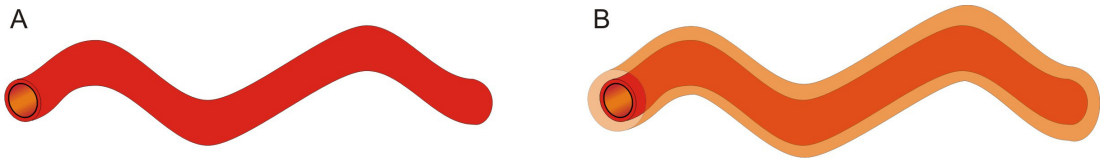

Figure 1-15:
Sketches of aggregates:
A: uncoated aggregate; uncoated, offering a negative surface.
B: wrapped aggregate; coating with layer of polyelectrolyte (no functionalization, therefore plain).

The coating of C8S3-aggregates is comparable to the wrapping of biological cells. Their lipid-shell is neither stiff, nor static and has similar properties to that of the tubular wall. It was shown that successful cell-wrapping is dependent on concentration-ratio of polyelectrolyte and membrane lipids, on size of vesicles (and hence curvature of the membrane), and other surfactant issues [44,45,46,47]. To conclude, the wrapping of C8S3-aggregates is not a trivial question. However, in contrast to biological cells or vesicles of lipids, the aggregates allow to probe the

molecular structure by optical spectroscopy. Already small changes of the molecular arrangement of this peculiar membrane can be monitored very sensitively.

As a first type of functionalization here the decoration of aggregates with dye-labeled polyelectrolytes is investigated. On behalf of mounting the functionalization directly in the aggregate the wrapping-layer is utilized. The aggregate has to be coated with prior functionalized polyelectrolytes to become functionalized itself. The dye-labels are covalently bound to the coating and therefore fixed within the shell, see Figure 1-16.

Figure 1-16:
Sketch of a functionalized aggregate. Acceptor-dyes are bound to the coating. Energy is transferred from aggregate via FRET to the dye.

The dye-labels on, respectively in, the aggregate-coating are statistically distributed. The energy-transfer distance, enabled via Förster-resonant-energy-transfer (FRET) up to a distance of several nanometer, is sufficient as long as the spectral-overlap is large enough.

Although in Figure 1-16 acceptor labels are shown, donor-labels can be distributed on the aggregate as well. Energy-transfer establishes in that case from the dye-labels to the aggregate. Effective energy-transfer leads to increased fluorescence of the acceptor, since the donor is pumping the acceptor. On the other hand, the donor-fluorescence is decreased – or quenched. This donor-quenching is caused by a reduced lifetime of the donor's excited states in presence of an acceptor. Therefore, energy-transfer can easily be detected by measuring static fluorescence spectra or time resolved fluorescence decay [48].

1.5 Aim of this work

It is the aim of this work to explore the possibilities of further functionalization of the tubular dye aggregates by wrapping them with dye labelled polyelectrolytes. As a first step of functionalization Förster resonance energy transfer is selected. These experiments are merely a "proof of principle" and not considered as completed.

This thesis will first describe the electrostatic properties of the tubular aggregates that lead to adsorption of polyelectrolytes (Chapter 5.1). In a second step, the wrapping of the aggregates by various polycations is described in order to find optimized material properties for homogeneous adsorption (Chapter 5.2). In a third step, dye-labelled polyelectrolytes are used for FRET experiments where the aggregates serve as donor or acceptor or both (Chapter 5.3). By spectroscopic investigations the energy transfer efficiency will be probed.

As experimental tools mainly cryogenic electron microscopy (cry-TEM) is utilized together with optical spectroscopy.

2 THEORETICAL BACKGROUND

"La Filosophia è scritta in questo grandissimo libro, que continuamente ci stà aperto innanzi à gli occhi (io dico l'vniuerso) ma non si può intendere se prima non s'impara à intender la lingua, e conoscer i caratteri, nei quali è scritto. Egli è scritto in lingua matematica, e i caratteri son triangoli, cerchi. & altre figure Geometriche ..."

Philosophy is written in this vast book, which lies entirely open before our eyes (I mean the universe). But it cannot be understood unless you have first learned to understand the language and recognise the characters in which it is written. It is written in the language of mathematics, circles, and other geometrical figures. Without such means, it is impossible for us humans to understand a word of it, and to be without them is to wander around in vain through a dark labyrinth...

(The book of nature is written in math.)

Galileo Galilei, Saggiatore (Assayer), 1623

2.1 J-aggregates of cyanine dyes

The J-aggregates discussed in this work are structures of cyanine dyes. The characteristic J-band as observed by optical spectroscopy establishes due to the coupling of the individual dyes. The optical properties are caused by the collective Frenkel excitons that describe the excited states and therefore the optical response of the aggregates.

The optical properties are highly sensitive to changes in the supramolecular structure, which can be utilized to testify if changes in the aggregate's order took place. Throughout this work I will refer to this spectral feature in order to proof the maintenance of the aggregate structure during the coating attempts [37,49,50,51]. The characteristic J-band is also an indicator for the possibility of exciton migration.

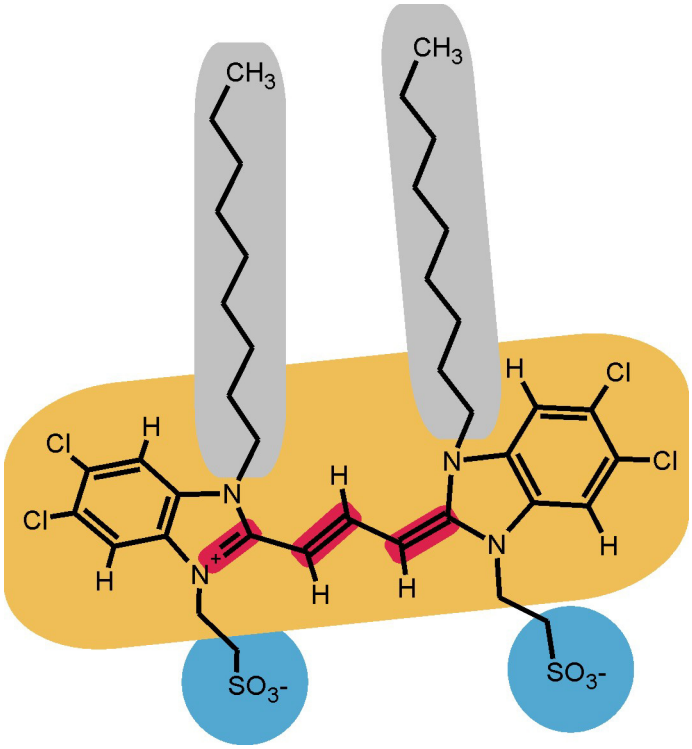

Figure 2-1:
C8S3-molecule, highlighted is the cyanine-backbone in yellow, the delocalized π-orbital-system consisting of several C-double-bonds (red). The nonpolar side-chains are highlighted in grey, while the polar sulfur-groups are depicted in blue.

The dye monomers offer a chromophore, given by the delocalized π-orbital-system along the polymethin-chain in the center of the molecule. The π-conjugated system is causing the optical response of the molecule and it's high polarisability. Optical excitation leads to the formation of strong transition dipoles that are oriented along

the polymethin-chain. This type of carbo-cyanines is sensitive to wavelength around 520 nm.

Cyanine dyes are naturally slightly hydrophobic, but polarisable. This leads to aggregation in aqueous solution. Due to the addition of hydrophobic side-chain (nonpolar), the solubility in water is further reduced, as the hydrophobic effect increases. Therefore the aggregation of C8S3 takes place at lower concentration. In other words, the CMC of C8S3 is lower than for common cyanines.

Additionally, the hydrophobic alkyl chains affect the structure of molecular packing. For surfactants and lipids a structural packing parameter was defined that is given by the ratio of the volume of the hydrophobic chains and the product of length of chains times cross sectional area of hydrophilic head group [52]. Depending on the size of this parameter, the morphology of the supramolecular structures above the CMC can roughly be predicted [53]. For the case of the amphiphilic cyanine dyes this parameter is less but close to 1 which corresponds to lamellar or cylindrical structures. Indeed, besides the tubular structures, also lamellar structures were found for a certain derivative of the dye above, named C8O4 [17,20,27,54,55,56].

2.1.1 Molecular optical response

The pure electronic absorption spectrum of a dye molecule is generally described by:

$$A(\omega) = A_0 \sum_f \left| \left\langle f \left| \vec{\mu} \cdot \vec{e} \right| g \right\rangle \right|^2 \delta(E_f - E_g - \hbar\omega) \qquad \text{(eq. 2-1)}$$

$\vec{e}$: polarisation of incident light, $\hbar$: Planck constant

E_g : energy of ground state, E_f : energy of excited state,

ω: frequency of electric field, $\vec{\mu}$: transition-dipole moment,

A_0 : prefactor,

$|g\rangle$: ground state, $|f\rangle$: excited states,

The absorption spectrum **A(ω)** can be understood as a superposition of sharp peaks with a natural Lorentz-broadening. One can derive the oscillator strength from that absorption spectrum, as the area under each peak gives the strength of the transition. Furthermore, the Frank-Condon-effect leads to progression of peaks due to consideration of vibrational and rotational levels. The strength of the absorption is

calculated within this linear approximation by the transition dipole moment $\boldsymbol{\mu}_{fg}$, given by

$$\vec{\mu}_{fg} = \langle f | \vec{\mu} | g \rangle \qquad \text{(eq. 2-2)}$$

The final absorption spectrum consists of a series of resonant frequencies that cause transitions from ground to excited states. Forbidden transitions do not contribute to the absorption spectrum, as their transition dipole results in $\boldsymbol{\mu}_{fg} = 0$.

The above given description neglects rotational and vibrational effects on the transition-energy. The environmental influence of a molecule causes an inhomogeneous broadening of the transition-energy. The result is a broadening of the absorption peak by a gaussian function.

These formulations are valid as long there is no interaction between the excited systems. So the discussed theory can by applied to single molecules or molecules in highly diluted solutions, where one assumes, that molecules are far away from each other.

2.1.2 Dimers

Compared to single or individual molecules, aggregates consist of a dense packing of molecules, causing an interaction between the excited states of each molecule. The easiest way to explain such an interaction is by considering a dimer. Such a dimer is the simplest kind of an aggregate and therefore an easy entry for description of the transition dipole coupling.

As the two monomers are identical, they have equal transition energies:

$$E_1 = E_2 = \hbar\omega_0 \qquad \text{(eq. 2-3)}$$

Both transitions have equal magnitudes of dipole moments.

$$|\mu_1| = |\mu_2| \qquad \text{(eq. 2-4)}$$

Excitation of the dimer leads to resonant coupling that describes the interaction from one excited molecule to a non excited neighbour. This excitation transfer can be described as

$$E_{resonant} = J\left(|2\rangle\langle 1| + |1\rangle\langle 2|\right) \qquad \text{(eq. 2-5)}$$

Where |**1**> and |**2**> describe excited states of molecule 1 or 2, respectively. The wave-functions of both monomers do not overlap. Their coupling is due to electrostatic attraction of the transition-dipoles. Therefore only excitation-energies are transferred. This is part of the tight-binding-approximation and it neglects exchange of charges between the monomers. Therefore the molecular orbitals of one molecule do not affect the orbitals of the neighbouring molecule, which is why their electronic ground-states are not coupling. Both molecules could be in the groundstate, molecule 1 or molecule 2 could be excited, or both could be excited. The latter combination requires very high intensities and is neglected further on. The strength of excitation transfer is given by the factor **J**, given by

$$J = J_{12} = \frac{\left[\left(\vec{\mu}_1 \cdot \vec{\mu}_2\right)\left|\vec{r}_{12}\right|^2 - 3\left(\vec{\mu}_1 \cdot \vec{r}_{12}\right)\left(\vec{\mu}_2 \cdot \vec{r}_{12}\right)\right]}{\left|\vec{r}_{12}\right|^5} \qquad \text{(eq. 2-6)}$$

As $\vec{\mu}_1$ and $\vec{\mu}_2$ are the dipole transition-moments and $\vec{r}_{12}$ is the relative vector between the dipole moments it is obvious that the excitation transfer is extremely sensitive to position and orientation of the two dipoles representing the molecules.
Furthermore the mixing of the eigenstates of the individual molecules enables two new system-eigenstates in case of resonant-coupling.

$$\left|\pm\right\rangle = \left(\left|1\right\rangle \pm \left|2\right\rangle\right)/\sqrt{2} \qquad \text{(eq. 2-7)}$$

The corresponding eigenvalues are the resulting excitation energies.

$$E_{\pm} = \hbar\omega_0 \pm J \qquad \text{(eq. 2-8)}$$

Referring to Figure 2-2, the linear splitted states are one-exciton state, as two molecules share one excitation quantum. The one-exciton is delocalized over both molecules. Such a phenomenon is known as a Frenkel exciton state [8,57].
As a result of this delocalized Frenkel exciton, the interaction with light depends on the transition dipoles of the excited states $\left|+\right\rangle$, $\left|-\right\rangle$, which are given by

$$\vec{M}_{\pm} = \vec{\mu}_1 \pm \vec{\mu}_2 \qquad \text{(eq. 2-9)}$$

One can show, that this gives rise to two transitions that are in general polarized perpendicular to each other. These two transitions are known as Davydov

components, if molecules are not parallel, and the frequency between them, 2|J|, is known as the Davydov splitting [8].

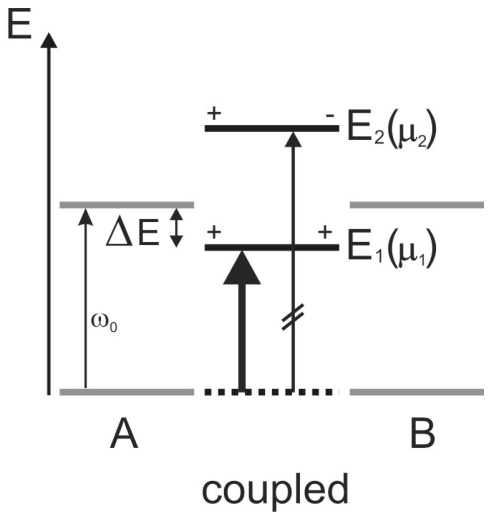

Figure 2-2:
Scheme of energy-splitting due to coupling of transition dipoles.

The resulting energy-shifts of the excited states depend on the geometric arrangement of the two monomers to each other due to the geometrical sensitivity of the coupling factor **J**. In case of two parallel dipoles the main factor on the energy shift can be ascribed a tilt or shift as indicated in Figure 2-3.

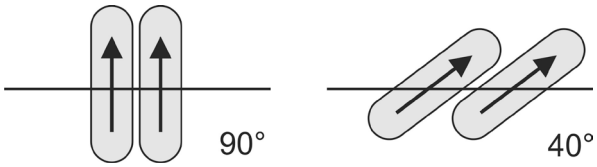

Figure 2-3:
Scheme of dipole tilt in dimer arrangement. Left: both dipoles oriented 90° to a virtual axis through the middle of the dipoles. Right: both dipoles tilted with about 40° against the middle-axis.

In reference to this tilt the selection rules for the allowed transition changes sign with decreasing tilt angle φ. As long as both dipoles are tilted with $\varphi = 90°$ (and close by) to the middle-axis the resulting transition is blue-shifted to the monomer-transition [58]. This is the case in so called H-aggregates (hypsochromic shift, heads close to heads). From tilting-angles below 53° the resulting transition is red-shifted, which is the case in J-aggregates (heads close to tails).

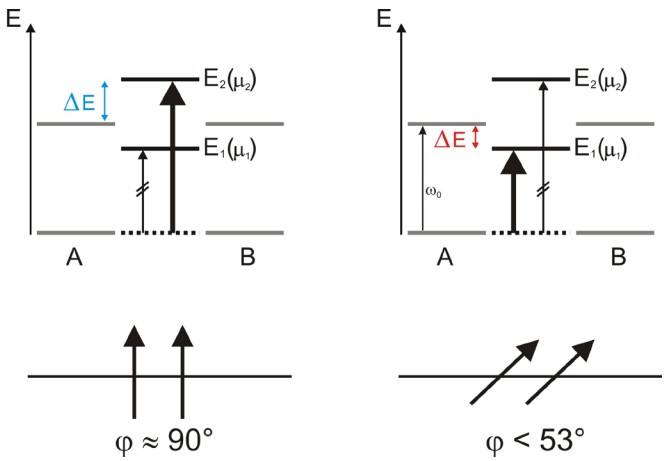

Figure 2-4:
Scheme of H- and J-aggregates. Variation of tilting angles causes dramatic changes in energy-shift.

2.1.3 Linear chain - homogeneous chain of N dye molecules

Expanding the case of the dimer to a chain of dyes the interaction strength is given by the same relation for **J** (see eq. 2-6). One has to consider, that the interactions in general are not restricted to interactions between neighbouring molecules.

All transition frequencies are supposed to be equal, $\omega_0 = \omega_n$, and the transfer-interaction J_{nm} is a function of the mutual orientation and distance of molecules at position **n** and **m**. As seen from equation (2.7) the indices 1 and 2 are replaced by **m** and **n** [59]. In the case of single excitons, **N** eigenstates are obtained and described by the wavevector $|k\rangle$. The dimer Eigenstates $|1\rangle$ and $|2\rangle$ are replaced with $|k\rangle$ in the chain of **N** dyes. The new Frenkel exciton Hamiltonian describes the excited states in the linear aggregate. It is a superposition of two Hamiltonians, one for the internal electronic coupling, the other for the exciton transfer interaction.

$$H = \sum_{n=1}^{N} \hbar\omega_0 b_n^+ b_n + \sum_{n,m=1}^{N} J_{nm} b_n^+ b_m \qquad \text{(eq. 2-10)}$$

The operators $\mathbf{b_n}^+$ create and $\mathbf{b_n}$ destroy excited states on a molecule on position **n** [57,60].

H is diagonalized by eigenfunctions $|k\rangle$ for the exciton-state that are given by

$$|k\rangle = \sum_{n=1}^{N} \sqrt{\frac{2}{N+1}} \sin\left(\frac{\pi k n}{N+1}\right) b_n^+ |g\rangle \qquad \text{(eq. 2-11)}$$

With open boundary conditions one derives the energy states for an endless linear chain of dipoles (**N** --> ∞). Periodic boundaries on the other hand are valid for ring-structures.

Figure 2-5:
Linear chain of aequidistant parts.

A linear chain can be described with a pointing-vector $\vec{n}$, pointing to the **n**-th part of the chain. The distance between the parts is **a** and there are up to **N** parts in the chain.

$$\vec{n} = n \cdot a \qquad \text{(eq. 2-12)}$$

If one restricts to nearest neighbor interactions, the band of energy eigenstates reads as:

$$E(k) = \Delta\varepsilon + 2J \cdot \cos(kna) \qquad \text{(eq. 2-13)}$$

The distinction into H- and J-aggregates is at this point necessary. It can be visualized by looking at the band structure of **E(k)** vs. **k**. In the case of positive values for **J** (J > 0) the energy-plot of **E(k)** differs from the case of negative **J** (J < 0), see Figure 2-6.

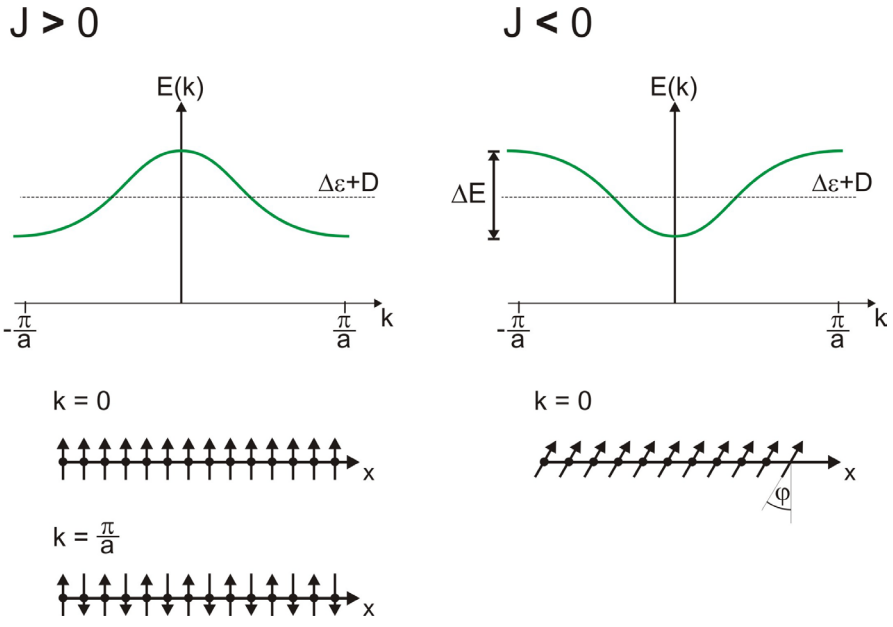

Figure 2-6:
Energy plots for H- and J-aggregates. Depicted are corresponding parallel and anti-parallel orientation of transition dipoles (at time t=0) for the case of H-aggregates. For J-aggregates only the dipoles in state k=0 are shown.

Optical transitions are only allowed for **k** = 0. For all other **k** the dipole-moment vanishes. Depending on value of **J**, one finds different results in spectrum shifting when aggregating, as it was the case for the dimer. For **J** >0, the aggregate is blue-shifted and literature names it H- or S-aggregates. For **J** <0, the aggregate is red-shifted and it is known as J-aggregate.

$$\Delta E = \pm 2J \qquad \text{(eq. 2-14)}$$

For the case of **N**=2 the equation (2-13) merges into the dimer-case, separating the states with 2| **J** |.

Nevertheless, the superposition of all interactions in the linear chain provides a non-symmetric energy-splitting **ΔE**. Furthermore, the non-periodic boundary conditions for real (finite) linear chain results in the following relation for the oscillator strength:

$$\left|\mu_k\right|^2 = \left\{ \frac{2\mu^2}{N+1} \cdot \tan^{-2}\left(\frac{\pi \cdot k}{2(N+1)} \right) \right\} \text{ if k is odd} \qquad \text{(eq. 2-15)}$$

$$\left|\mu_k\right|^2 = 0 \text{ if k is even} \qquad \text{(eq. 2-16)}$$

k = 1, 2, 3, ..., N

For a long linear chain of such dyes, **N**>>1, the highest oscillator-strength between the ground state and the single-exciton band is related to the transition states **k** = 1 and **k** = 3.

k = 1	81 %	of total oscillator-strength
k = 2	0	of total oscillator-strength
k = 3	9 %	of total oscillator-strength

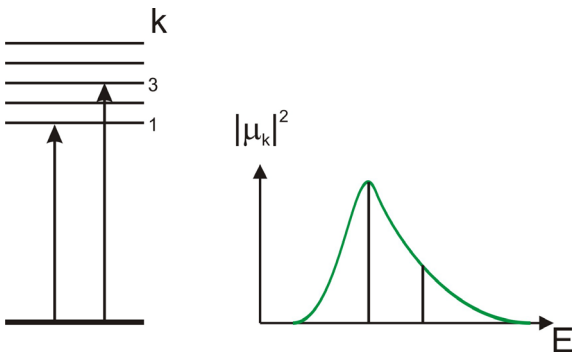

Figure 2-7:
Scheme of oscillator-strength contribution to absorbance of a linear chain of dye-molecules

The magnitude **μ** is in this case the value of a single molecule [61,62]. One then finds for the strengths of the exciton state with **k** = 1:

$$\text{k=1} \quad \Longrightarrow \quad \mu^2_{k=1,g} \approx 0{,}81(N+1)\mu^2 \qquad \text{(eq. 2-17)}$$

This means, that 81% of the total transition energy are located to that transition. The **k** = 1 state offers no nodes (except at **x** = 0, ..., N), which is why the dipoles of the individual molecules oscillate in maximum phase [10,14]. With this mathematical reflection, we have basically the reason for the characteristic J-band in absorption and emission of such aggregates. This transition is dominating the spectrum.

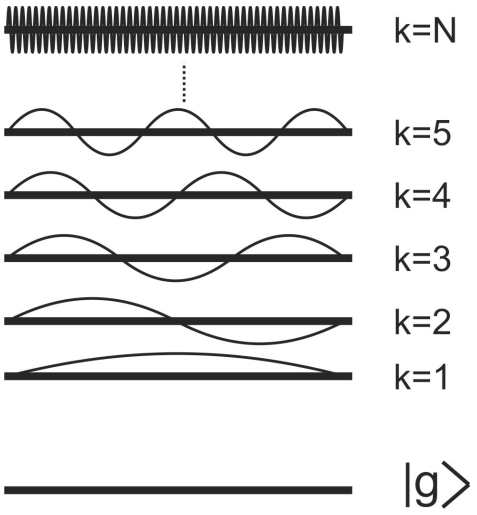

Figure 2-8:
Schematic view of excited states showing oscillation-loops for various k-values. The k-state offers k-1 nodes. The overlap of the wave-functions can be derived from this figure.

All states with even **k**-values produce no oscillator strength. Their wave-functions cancel out. The next contributing state is **k** = 3, providing 9% oscillator strength in long chains (**N**>>1). Under this consideration, **k** = 1 provides an oscillator strength in the order of **Nμ²**, which is generally referred as the giant oscillator strength [59].

2.1.4 Ring aggregate

Ongoing from the linear chain one sets new boundary conditions to derive a periodic or ring arrangement. The number **N** of dipoles ought to be limited (**N** << ∞). The geometry in such an arrangement of molecules highly effects the transfer interaction **J** between the molecules. As discussed before, the allowed states **k** in a linear chain

are not degenerated. In contrast to that, an aggregate offering cylindrical symmetry, leads to degeneration of the optical allowed states **k**, that gives a pair of **k** = ±1.
An approach for discussion is to describe ring aggregates as a circular arrangement of equally distributed 2-level molecules [63], see Figure 2-9.

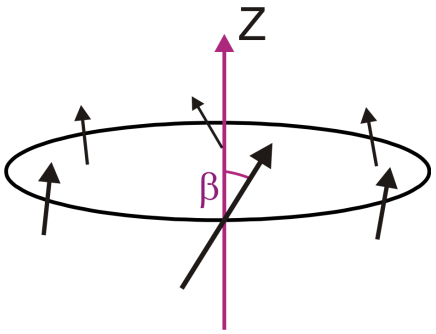

Figure 2-9:
Orientation of dipoles μ in projection. Z is the orientation of the aggregate-tube.

With the assumption, that the individual molecules on the ring, **n**= 1, 2, .., N, offer the transition dipole $\boldsymbol{\mu}_n$, and they are not in plane (projections of the dipoles may remain in the plane), the Frenkel exciton Hamiltonian can be described as in eq. 2-10. The dipoles are given by:

$$\vec{\mu} = \mu_0 \left(\cos\beta \cdot \cos\alpha, \cos\beta \cdot \sin\alpha, \sin\beta\right) \qquad \text{(eq. 2-18)}$$

$$\alpha = \frac{2\pi \cdot n}{N} \text{ and } n = 1,\ldots, N$$

From this one finds the relation:

$$\text{for k=0: } \vec{\mu}_0 = \frac{1}{\sqrt{N}} \sum_n \vec{\mu}(\alpha,\beta) = \sqrt{N} \cdot \mu_0 \cdot \sin\beta \cdot \vec{e}_z \qquad \text{(eq. 2-19)}$$

$$\text{for k=±1: } \vec{\mu}_{1,2} = \frac{\sqrt{N}}{2} \cos\beta \cdot \mu_0 \cdot \vec{e}_x \pm i\vec{e}_y \qquad \text{(eq. 2-20)}$$

The related energies result to be:

$$\text{for k=0: } E = \Delta\varepsilon + 2J \qquad \text{(eq. 2-21)}$$

$$\text{for k=±1: } E = \Delta\varepsilon + 2J + W\cos\left(\frac{2\pi}{N}\right) \qquad \text{(eq. 2-22)}$$

The interaction energy **J** is dependent on the structure of the aggregate. State **k**=1 is slightly red shifted with **J**<0.

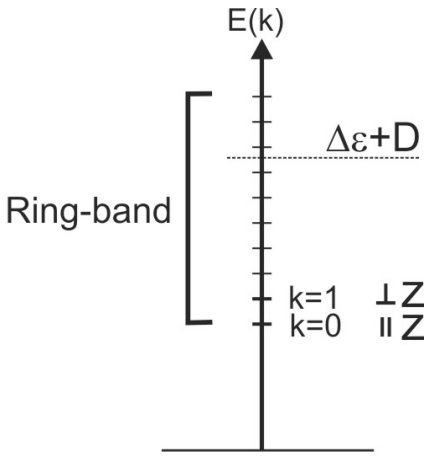

Figure 2-10:
Scheme of energy-band in a ring-aggregate. Only the two lowest levels are accessible. The J-band energy-shift is depicted.

2.1.5 Cylindrical aggregates

Cylindrical aggregates are a linear chain of ring-aggregates. In a simplified approach they are described as a stack of many rings [30], see Figure 2-11.

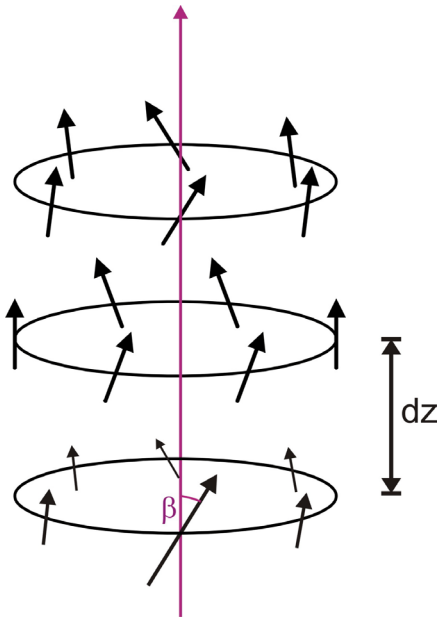

Figure 2-11:
Sketch of cylindrical aggregate as a stack of ring-aggregates. Each ring offering a defined distance dz to it's neighbour, as well as a certain tilt from ring to ring.

In this model there are two bands. One originates from the ring-aggregates, the other from the stack of the rings, forming a cylinder. From the preceeding chapters one knows, that transitions take place only at $\mathbf{k_z} = 0$ and $\mathbf{k_t} = 0, \pm 1$.

From the individual ring-aggregates one resulting $\boldsymbol{\mu}_k$-vector in **z**-direction remains. These vectors in **z**-direction establish a linear chain, as long as the ring-aggregates are arranged with a small tilt to each other. This linear chain in **z**-direction establishes another band-transition. One transition in z provides 100% intensity if all rings are equal and $\mathbf{k}_{||} = 0$ [30].

As a result of this linear-chain in the stack of ring-aggregates, the theory shows a characteristic energy-shift, as discussed in the chapter 2.1.3. From the properties of the ring-aggregates, the presence of two transitions remains. They are assignable to $\perp$**Z** and $||$ **Z**, where **Z** is the long axis of the cylindrical structure.

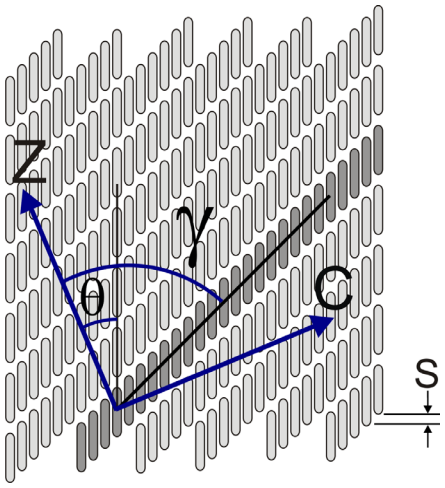

Figure 2-12:
Sketch of dipoles arrangement in cylinder. The black-line across the dark-grey bricks shows the virtual ring-aggregate within the cylinder. Z is the cylinder-axis, while C shows the roll-vector. S is the displacement of the individual cyanine-dyes providing the J-aggregate.

Figure 2-12 sketches the geometric aspects of the brick-layer model in the aggregates. The roll-vector **C** is naturally oriented perpendicular to the long axis **Z** of the cylinder. The angle θ is given between the orientation of the dye-dipoles and the cylinder-axis **Z**. The tilt of the dipoles leads to a displacement from each brick to the next. This displacement leads to an orientation angle γ of aligned dipoles relative to the cylinder-axis.

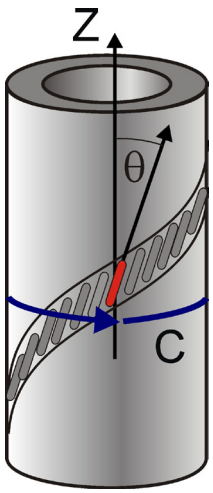

Figure 2-13:
Sketch of the cylindrical-aggregate. C indicates the roll-vector, Z is the orientation of the idealized aggregate-cylinder. The highlighted red cyanine-monomer shows the orientation of the dipoles within the aggregate-structure.

Figure 2-13 illustrates the dipole alignment wresting around the cylinder. Large cylinder-axis **Z**, roll-vector **C** and orientation angle **θ** are given in accordance to Figure 2-12.

2.1.6 Double-walled tube

The transitions of a double-walled tube are a superposition of two cylindrical aggregates. Each cylinder provides two radiative transitions, parallel and orthogonal to **Z**. The transitions of these two cylinders differ from each other, as they are not of same kind. One cylinder is fit into the other, offering therefore a smaller diameter, causing a stronger bending-angle and another tilt of monomers against the cylinder-axis **Z** ($\theta_i \neq \theta_o$), which is influencing the transition-energies. So such a double walled tube shows four transitions, two of the inner cylinder, two of the outer one. The depicted transition-energies of Figure 2-14 can be assigned to the peaks in the absorption spectra of C8S3 (see Figure 1-11) [64].

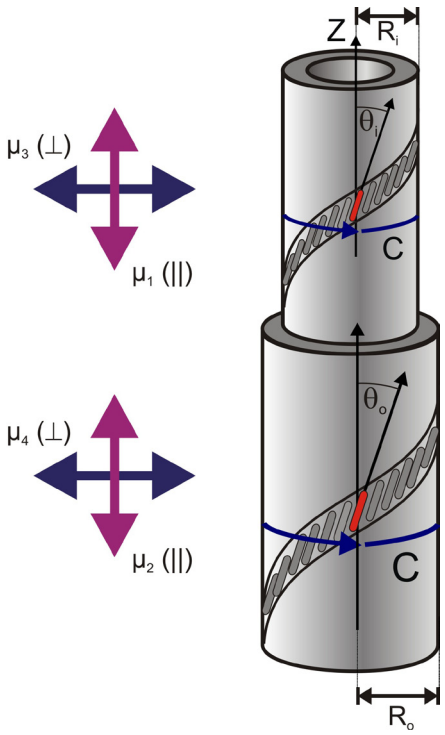

Figure 2-14:
Sketch of the cylindrical-aggregate (tube-in-tube). C indicates the roll-vector, Z is the orientation of the idealized aggregate-cylinder. The highlighted red cyanine-monomer shows the orientation of the dipoles within the aggregate-structure. Arrows on the left indicate the polarized transition of the individual tubes.

2.1.7 Exciton-diffusion and migration

It is known that excitons within organic materials are mobile mostly by an incoherent hopping process. This incoherent transport is also called exciton-migration, which was observed in molecular-crystals [62,65,66], conjugated polymers [67,68] and J-aggregates [69]. Early experiments by Scheibe using quencher molecules added to solutions of PIC gave rise to an estimation of a migration range of approx. 6000 molecules in PIC. It is further assumed that excitons in ordered materials are moving fast, with the speed of sound, and that the speed is directed due to the momentum of the incident photon [70]. In disordered materials, such as conjugated polymers, the exciton movement is better described by diffusion.

Due to the well ordered structure the tubular aggregates are expected to be able to establish energy-migration by Frenkel-excitons.

2.2 Polymer adsorption

2.2.1 Aggregate surface-charge

The double-walled aggregates are regular and well-defined structures. The inner and outer surface of the tube is covered with a large number of negative charges, provided by the polar SO_3^--groups of C8S3. Overall, the aggregate is a nano-scaled, cylindrical, hollow structure of known diameter with a large number of equally distributed negative surface charges. Therefore the aggregate may be utilized as a microscopic template [71,72].

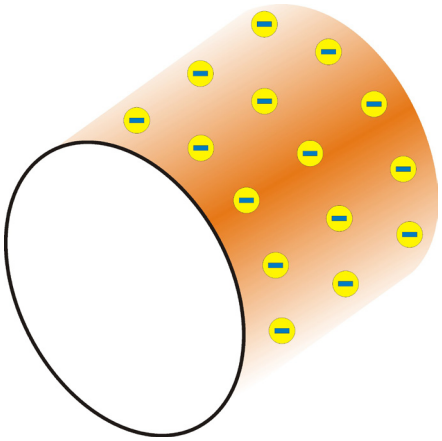

Figure 2-15:
Sketched aggregate surface with fixed and well-ordered negative charges.

Since the negative charges are attached to the dyes and the dyes are well ordered, one can assume that the charges are arranged at the aggregates surface on a well ordered grid, see Figure 2-15. The distances are fixed due to the structure of the aggregate. The mean charge density of the surface is estimated from the size and number of dye molecules and the dimension of the tubular structure. From the values given in Chapter 5.1 we obtain a mean density of 3.1 e/nm^2.

The aggregates appear in a neutral solution, which provides an equal number of counter-ions. The watery solution that surrounds the aggregates contains a number of positive ions (Na^+), each carrying a positive charge, so that over all the entire solution is neutral. On the other hand, the positive charges screen the negative surface potential over a certain distance, as given by the theory of Debye and Hückel [73]. The Debye-Hückel-Theory describes the disturbance of a homogenous mixture of positive and negative charges. A single negative charge would be surrounded by a large number of positive charges, due to electrostatic attraction. Equally charged

particles would repel each other. The strength of this screening is reduced by Brownian motion of the particles. This process is described by combination of Poisson-equation with Boltzmann-distribution of potential energy. As a result, the Coulomb-potential is screened by a length λ_D. The Debye-length λ_D is the distance from a single charge in which the potential drops down to the value of 1/e. It is defined in electrolytic solutions as follows:

$$\lambda_D = \sqrt{\frac{\varepsilon_0 \varepsilon_r \cdot k_B T}{2 N_A e^2 I}} \qquad \text{(eq. 2-23)}$$

In this case ε_0 is the electric field-constant, ε_r di-electric-field-constant, k_B is the Boltzmann-constant, **T** is the temperature in Kelvin and N_A is Avogadro-constant. The ion-strength is given with **I**, which is in this case given by the molarity of the solution, since all ions offer only one charge.

The number of Na^+-counter-ions in the aggregates solution equals the number of C8S3, which is given in work-solution with $3{,}36 \cdot 10^{-4}$ M. With these values, the Debye-length can be derived.

$$\lambda_D = 16.6 \text{ nm}$$

Kunze et al. [74] calculated the electrostatic attraction force between a cylinder and a helical-wrapping polyelectrolyte in dependence of a wrapping parameter ϑ.

2.2.2 Charged cylinders

The adsorption of a semi-flexible polyelectrolyte onto a charged cylinder was investigated theoretically by R. Netz and D. Andelmann [75] and experimentally by I. Gössl [76]. They discussed two approaches: The linear approach considers the interaction between the charges in accordance with the Debye-Hückel-theory. The non-linear approach takes the entropic counter-ion effect into account. The linear approach considers also a parallel alignment of the PE onto the charged cylinder.

Both approaches predict an overcharging of the complex. In the linear approach the overcharge, or over-compensation, is a result of electrostatic effects, while for the non-linear approach the overcharge is due to balancing of entropic effects (counter-ion release) and bending energies [76].

In both theories the total free energy is split into independent parts. Attractive contribution of oppositely charged cylinder and semi-flexible PE-chain on the one

hand and repulsive forces due to electrostatic repulsion on the other hand. The mechanical bending energy contributes additionally. The total free energy $\mathbf{F_{tot,\ linear}}$ of the linear approach is found to be a summation of all three independent parts.

$$F_{tot,linear} = F_{attractive} + F_{repulsive} + F_{bending} \qquad \text{(eq. 2-24)}$$

For vanishing salt-concentrations the bending-energy becomes negligible compared to the diverging electrostatic contributions. The total free energy minimizes with respect to the wrapping parameter ϑ.

$$\vartheta = \frac{\tau_C}{\tau_P} + \frac{1}{2} \qquad \text{(eq. 2-25)}$$

τ_P : Polymer charge-density τ_C : Surface charge-density of cylinder

The effective charge of the complex is the given by

$$\tau_{eff} = \tau_C - \vartheta\tau_P = -\frac{\tau_P}{2} \qquad \text{(eq. 2-26)}$$

The PE-coating dominates the effective charging of the complex. This is also valid for consideration of the non-linear approach, if neglecting the bending energy.

The important conclusion from this work is that the resulting surface-charge of the complex is determined by the coating-PE, no matter how the PE as attached to the cylinder.

2.3 Singlet-singlet energy transfer

2.3.1 Energy transfer

A prominent mechanism of fluorescence quenching is FRET. This effect usually happens at distances in the order of 10-100 Å [77].

For theoretical description consider a couple of donor and acceptor in close proximity. The ground-states are labelled as $\mathbf{D_g}$, $\mathbf{A_g}$, whereas the excited states are named $\mathbf{D_e}$, $\mathbf{A_e}$. If donor emission and acceptor absorption overlap, the coupling provides the resonance:

$$D_e + A_g \underset{k_{-T}}{\overset{k_T}{\Leftrightarrow}} D_g + A_e \qquad \text{(eq. 2-27)}$$

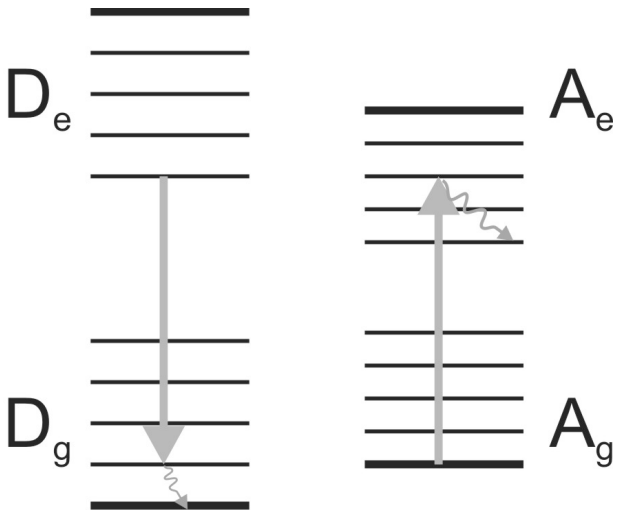

Figure 2-16:
Energy scheme of donor and acceptor coupled in resonant interaction. Vibrational relaxation occurs rapidly (taken from [77]).

The resulting acceptor singlet and donor singlet are in excited vibrational states. Fast vibrational relaxation takes place leading into ground vibrational levels. Therefore the reverse process $\mathbf{k_{-T}}$ of a possible efficient process $\mathbf{k_T}$ is unlikely to occur [77].

In the result, the donor fluorescence is quenched, while the acceptor becomes excited, which subsequently leads to fluorescence of the acceptor. This process is also called sensitized emission and will provide efficient transfer as long as distance between donor and acceptor is in the order of 50 Å.

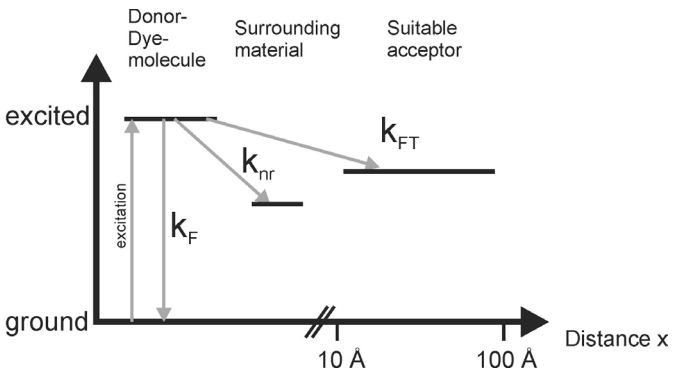

Figure 2-17:
Scheme of possible energy-processes of donor. Energy from excited donor may appear visible in fluorescence, non-visible in non-radiative processes such as heating the environment, and indirect-visible if Förster-transferred to an acceptor. The latter one is only available if a suitable acceptor is present.

One may name three processes ongoing from an excited state of a dye, see Figure 2-17. First there is the fluorescence itself, emitting light of certain wavelength, second non-radiative processes, such as collisions with neighbouring molecules in very close proximity, and third is meant to be energy-transfer to other molecules, which is only available if a suitable acceptor is around.

The general de-excitation rate **k** is given by the sum of all rates suitable for that species.

$$k = k_{FT} + k_{nr}^{D} + k_{F}^{D} \qquad \text{(eq. 2-28)}$$

$$\text{with } k_D = k_{nr}^{D} + k_{F}^{D}$$

The efficiency $\eta_{Transfer}$ of such an energy transfer is given by the fraction of $\mathbf{D_e}$ that is deexcited by the transfer-process.

$$\eta_{Transfer} = \frac{k_{FT}}{k_{FT} + k_{nr}^{D} + k_{F}^{D}} \qquad \text{(eq. 2-29)}$$

The transfer rate is given by $\mathbf{k_{FT}}$, while all other rates refer to donor processes, such as non-radiative losses ($\mathbf{k_{nr}}$) and of course the donor-fluorescence ($\mathbf{k_F}$), if present. These rates can be found theoretically or experimentally. As long as external parameters are kept fixed, their value is reproducible. The rates for $\mathbf{k_{nr}^D}$ and $\mathbf{k_F^D}$ are internal processes and cannot be avoided. The transfer rate $\mathbf{k_{FT}}$ on the other hand has an external origin, the presence of an acceptor in close proximity. The fluorescence investigation of the donor in comparison of donor with acceptor provides information

on the energy-transfer-efficiency via FRET $\eta_{\text{Förster}}$ (eq. 2-31), since in absence of an acceptor the $\mathbf{k_{FT}}$ is missing.

$$\frac{I_{D+A}}{I_D} = \frac{k_{nr}^D + k_F^D}{k_{FT} + k_{nr}^D + k_F^D} \qquad \text{(eq. 2-30)}$$

2.3.2 Förster transfer

The Förster-transfer itself is a transfer mechanism that is strongly dependent on the Förster-radius $\mathbf{R_0}$, but in the order of 10 – 100 Å distance efficient [78]. The resulting efficiency $\eta_{\text{Förster}}$ is given by the relation.

$$\eta_{Förster} = \frac{1}{1 + \left(\frac{r}{R_0}\right)^6} \qquad \text{(eq. 2-31)}$$

The distance of donor and acceptor is represented with **r**. The quotient of donor-acceptor-distance and Förster-radius incorporates to the efficiency with the power of 6. This means, that small excesses of average donor-acceptor-distances from the Förster-radius cause big losses of the transfer-efficiency.

The Förster-radius is the distance of a FRET-couple, where the transfer-efficiency drops to 50%. The energy-transfer efficiency is then given by:

$$k_{FT} = \frac{R_0^6}{\tau_D \cdot r^6} \qquad \text{(eq. 2-32)}$$

With this equation one also derives a relation with the lifetime of the donor's excited state [79]. This is very useful in time-resolved spectroscopy. One can derive a relation by comparing lifetimes of the donor's excited state in presence or in absence of an acceptor.

$$\text{with } \tau_D = \frac{\Phi_D}{k_D} \text{ and } \tau_{D+A} = \frac{\Phi_D}{k_D + k_{FT}}$$

$$\Rightarrow \frac{\tau_{D+A}}{\tau_D} = \frac{k_D}{k_D + k_{FT}} \qquad \text{(eq. 2-33)}$$

With eq. 2-35 and 2-34 this can be rephrased to:

$$\frac{\tau_{D+A}}{\tau_D} = 1 - \eta_{Förster} \qquad \text{(eq. 2-34)}$$

R_0 can be calculated from the spectral overlap of donor-emission and acceptor absorption. The quantity of this overlap is given by the overlap-integral **J** [80].

$$J = \int f_D(\lambda)\varepsilon_A(\lambda)\lambda^4 d\lambda \qquad \text{(eq. 2-35)}$$

$f_D(\lambda)$: normalized donor-emission at wavelength λ
$\varepsilon_A(\lambda)$: extinction-coefficient of acceptor at wavelength λ

The Förster-radius **R_0** is directly derivable from **J**.

$$R_0 = 8{,}79 \cdot 10^{-5}\left(J\kappa^2 n^{-4}\phi_D\right)^{1/6} \text{ Å} \qquad \text{(eq. 2-36)}$$

In this case **n** is the refractive index of the medium between donor and acceptor, **ϕ_D** is the quantum yield of the donor in absence of an acceptor and **κ^2** is a geometric factor that considers the orientation of donor and acceptor to each other. The value of **κ^2** may be assumed to 0.47 for the case of static and fixed positions that are randomly distributed and oriented.

2.3.3 Dexter transfer

The Dexter-energy-transfer is a resonant-transfer, too. It is a triple-triplet-coupling based on the overlap of electron-orbitals. It is known to be efficient for donor-acceptor-distances less than 10 Å.

$$k_{Dexter} \propto J \cdot e^{-\frac{2r}{L}} \qquad \text{(eq. 2-37)}$$

L : van-der-Waals radius

Since Dexter efficiency and range is weak compared to Förster, we will neglect this process and concentrate on pure FRET.

3 EXPERIMENTAL PART

"Es ist auf der Welt nichts unmöglich, man muss nur die Mittel entdecken, mit denen es sich durchführen läßt."

Nothing in the world is impossible, one just has to reveal the ways that perform.

Hermann Oberth, german rocket-scientist

3.1 Transmission electron microscopy

The technology of transmission electron microscopy (TEM) provides high resolution imaging of supramolecular and other structures. In contrast to X-ray structure-analysis, which needs a crystalline sample, TEM also performs with native samples. Necessary efforts to handle native samples of C8S3-aggregates in TEM are discussed in the paragraph 3.1.4.

TEM images are two-dimensional projections of three dimensional objects from translucent samples. The obtained image is a superposition of all structure densities. The material of the investigated aggregate-structures is of low atomic-number and therefore providing low contrast in the TEM. To overcome this contrast imaging-issue, the approaches of de-focussed obtaining and limiting the transfer-function were made, see paragraph 3.1.6 and 3.1.7.

The investigated aggregate-structures are not electron-beam-resistant. To avoid serious radiation damage the exposure time of aggregates has to be limited, as described in paragraph 3.1.5.

To explain each effort made to circumvent imaging issues of C8S3-aggregates it is necessary to understand the basic TEM-setup and it's influence on sample imaging. The TEM can be understood in analogy to classical light optical microscopy (LM).

3.1.1 Philips CM12 TEM

For the images of this thesis a TEM made by Philips, model CM12 including a Gatan cryo-add-on was used. The CM12 microscope is one of the most common commercial electron-microscopes. The CM12 has a special cooling equipment and comes with a liquid-nitrogen cooled specimen-holder made by Gatan. This add-on enables measurements at very low temperatures. There are only few electron-microscopes with a cryo-add-on located in the area of Berlin. One Philips CM12, including a cryo-add-on, is at the Freie Universität zu Berlin, Forschungszentrum für Elektronenmikroskopie (FZEM). This where the cryo-TEM investigations were carried out.

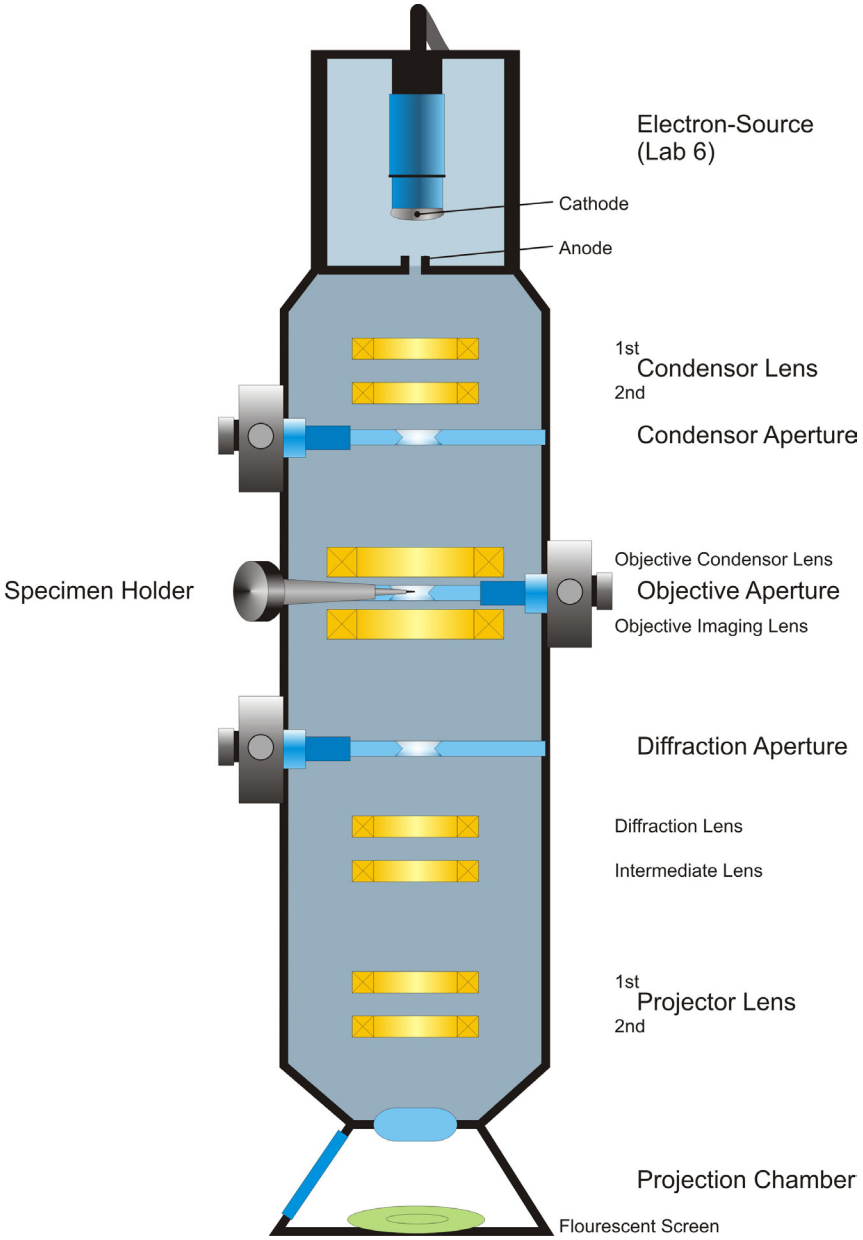

Figure 3-1:
Schematic layout of a TEM.

Figure 3-1 gives a schematic overview of the general setup of the TEM-column.
On top of the column the electron source is located. It is a thermo-ionic LaB_6-cathode (lanthanum-hexaboride) which enables acceleration voltages up to 120 keV and higher. The high-voltage is applied between anode and cathode. A bias-voltage may be applied between Wehnelt-cylinder and cathode, steering the emission by the variation of the emission-area. The filament of the crystalline LaB_6-electron-source may additionally be heated to increase the electron-flux.

The compound of electron-source, anode, cathode and Wehnelt-cylinder is called “gun”. The cathode of this compound can be shifted and tilted relatively to the optical axis of the column alignment, which will later be referred as gun-tilt.
Right beneath the gun is the evacuated column, which can be separated into two parts: illumination and imaging section. The condensor coils parallelizes the electron-beam on the specimen whereby the condensor-aperture limits the beam-width.
In between both sections is the specimen. The specimen is, as usual in modern TEM, located within the objective lens, the first and strongest imaging lens in the ray-path. The objective aperture in the backfocal-plane of the objective-lens may be enabled to increase contrast-depth by removing scattered electrons from the ray-path. The CM12 has an aperture holder with exchangeable contrast apertures in the range of 30 μm up to 100 μm.
In the imaging section, the subsequent lenses magnify the first image obtained from the objective lens. The objective lens can be switched between diffraction and image-mode, each mode is projected on the fluorescent screen or camera, respectively.
The fluorescent viewing screen may be moved to let the electron beam pass through to a camera mounted underneath. This camera uses commercial Kodak SO-163 Electron Films photoemulsion plates, that are illuminated separately. The TEM camera is capable of 36 plates, which have to be developed in the end of each session by a proper photo-development procedure, utilizing the Kodak ID-19 developer.
In addition to the TEM camera, there is a TV-camera mounted in parallel. This device is used for precise setup of parameters during the measurement and allows also a fast-Fourier-calculation (FFT) in nearly realtime via a small computer. This FFT is necessary for the stigmatism-correction.

3.1.2 Resolution and aberration

The transmission electron microscopy is based on the particle-wave-dualism of electrons and was first realised by E. Ruska and M. Knoll in 1930. It is a direct way to beat the optical resolution of classic-optical microscopes that is given by the Rayleigh-criterion.

$$d_{\min} = 0{,}61 \cdot \frac{\lambda}{NA} \quad \text{with} \quad NA = n \sin\varphi \qquad \text{(eq. 3-1)}$$

d_{min} : Minimum-distance of 2 objects

φ : Aperture

λ : Wavelength

n : Refraction index

NA : Numerical aperture

From this formula one can derive the resolution $\mathbf{d_{min}}$, the distance of two individual objects that can be separated by visual inspection through an optical microscope. It is mainly given by the wavelength of the used light. By using light of shorter wavelength in the visible-range or by increasing of the refractive index **n** by oil-immersion one may achieve a $\mathbf{d_{min}}$ of about 240nm.

Ruska and his group replaced that virtually big photons with virtually smaller particles: accelerated electrons. The assignable wave-length of an accelerated electron is given by the following de-Broglie-equation [81].

$$\lambda = \frac{h}{\sqrt{2m_0 e U_B^*}}, \text{ with } U_B^* = U_B\left(1 + \frac{eU_B}{2m_o c^2}\right) \qquad \text{(eq. 3-2)}$$

U_B : acceleration Voltage

U_B^* : relativistic correction

m_0 : electron mass

e : elementary mass

c : vacuum speed of light

To compare, an electron accelerated with 100 keV has a wavelength of 0.0037 nm. That delivers a theoretical possible resolution in sub-nanometer-range.

TEM can be explained with nearly the same terminology of classical optical microscopy, as there are many analogies. The photon as scattered particle is replaced by electron and therefore optical lenses and apertures are replaced by magnetic lenses. A well-designed composition of electromagnetic fields induced by magnets, coils and capacitors focuses, tilts, shifts and deflects the electron-beam, which is accelerated with a few keV in an evacuated column.

Magnetic lenses also suffer from inaccuracies, i.e. aberrations [82]. The major aberrations are chromatic, stigmatic and spherical. The results of these aberrations are losses on focus-depth and distortion in images.

Chromatic aberration is caused by the difference in speed, respectively wavelength, of the accelerated electrons, which is a big issue especially on thermo-ionic electron guns. Emitted electrons have a distribution in speed with a certain spread. Faster

electrons or electrons with higher frequency, respectively, cause a weaker bending of electron beams in magnetic lenses. Therefore the focus of a magnetic lens spreads as much as the inhomogenity of electron-speed-spread.

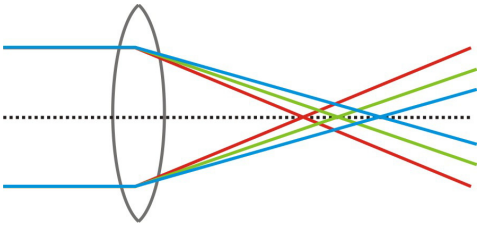

Figure 3-2:
Sketch of chromatic aberration.

Spherical aberration is caused by inhomogenities in the magnetic field. The electron-beam offering a certain diameter is affected differently by the lens in the center than far off the center. Electrons on the edge of the lens are bend stronger, causing a shorter focal distance. This causes a less focussed beam. The defined focal point is reduced to a point of "least confusion".

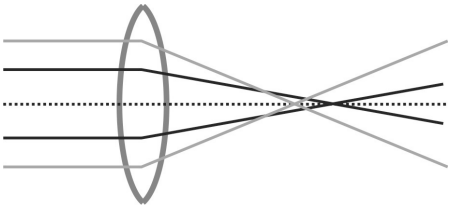

Figure 3-3:
Sketch of spherical aberration.

Stigmatism is originated by tilts of the electron gun. A gun tilt causes the electron beam to hit the lens plane not exactly perpendicular. Due to imhomogenities in the lens geometry a beam tilt leads to an unsharpness as known from classical optics. Further inhomogeneties or contaminations in proximity of the lense increase stigmatism.

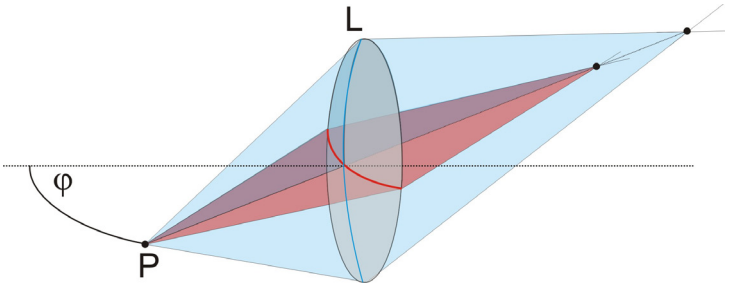

Figure 3-4:
Sketch of Stigmatism.

All these mentioned aberrations limit resolution and image sharpness. Their effect on imaging has to be taken into account. Disadvantages can be minimized by proper alignment of the gun, result-oriented setup of parameters and constant control of image parameters during the measurement, i.e. stigmatism control.
Overall, the resolution in TEM is rather limited by technical, than physical properties. Investigations on vitrified C8S3-specimens can be easily obtained with a resolution of 0.34 nm for an acceleration voltage of 100 keV and magnification of 60 000x, which is the applied magnification for all investigated samples in this work, unless stated otherwise.

3.1.3 TEM sample

Samples are prepared in most cases on commercially available copper TEM-grids. Samples have to be very thin to be translucent. Dependent on the atomic mass of the investigated material, absorption contrast reaches saturation at thicknesses ≅ 300 nm.

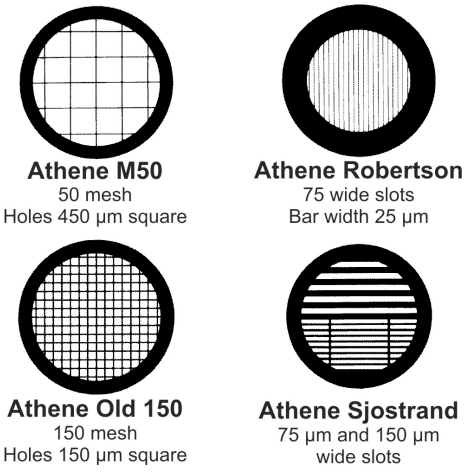

Figure 3-5:
Various shapes of TEM-grids [83].

There is a wide variety of grids available on the market, providing different shape and material. Most common are grids made of copper, but gold, silver, titanium or other comparable materials are also available. The grids are very thin, i.e. 10 to 20 µm, but still opaque for electron beams in between the solid bars.
Besides this variety of commercial available copper-grids, the investigation of C8S3-aggregates in solidified (vitrified) solution requires a special modification of the grid. The distances between the Cu-bars have to be bridged with a opaque polymer-film. Such a polymer-film is given with the brand marked Quantifoil. The advantage of

such a foil is manifold. During the sample-preparation, the foil provides a thin (5-10 nm) fixating backbone to the liquid solution, while vitrified. The defined holes in the foil guarantee sufficient thin ice to be translucent (few ten nanometers). On the other hand, the foil provides contrast rich background during investigation, which is necessary to find the focal-plane. The grainy background enables beam alignment procedures. Charging effects, resulting from accumulated electrons on sample-surface, can be avoided by conductivity of the supporting film. During the entire cryo-TEM investigations at the FZEM there have been unexceptionally used Athene Old 200 mesh (copper) with a Quantifoil R1/4 cover.

These foil covered copper-grids have been hydrophilized before sample application by glow-discharge in a BalTec MED-020 [84].

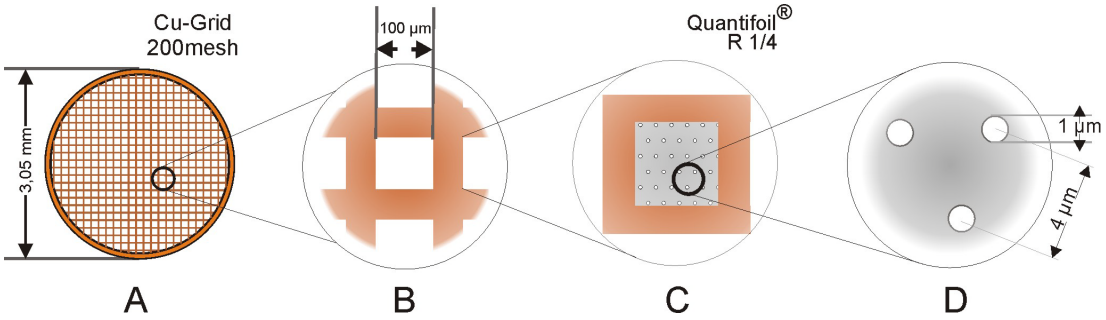

Figure 3-6:
Sketched TEM-grid
A: Copper grid of shape Athene Old 200 mesh with a total-diameter of 3.05 mm.
B: Detailed view of copper-grid, 200 copper-bars per inch provide 100 µm squares.
C: Quantifoil cover on copper-grid spans over square-holes.
D: Quantifoil R1/4 provides holes in defined size (1 µm) and distance (4 µm).

This means a grid with 200 copper bars per inch, see Figure 3-6, providing a square-mesh, or square-stitch, with 100 µm length and height, provides an electron transmission of 55%. Each one of these mesh is spanned by a polymer-film that is perforated with holes of 1 µm in diameter in equal distances of 4 µm. The applied liquid material allocates ideally within these holes while surround polymer-film can be utilized to find the focus in the microscope, see Figure 3-7.

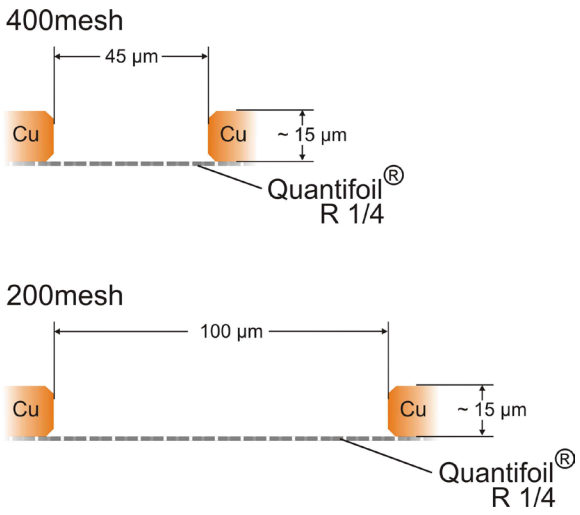

Figure 3-7:
Sketched cross-section of Quantifoil R1/4 on copper Athene Old 200 mesh respectively 400 mesh.

The sample is simply prepared by application of a small droplet of the solution. The solvent dries and the sample remains in the holes of the quantifoil-film.
To avoid fragile samples from damage through drying one may solidify samples in solution by vitrification them before the solvent is entirely dried.

3.1.4 Cryo-TEM sample-preparation

The preparation of cryo-samples requires enhanced skills. As the investigated material has to be kept in aqueous solution to maintain its structure, the preparation of samples is done by solidification of the entire ultra-thin layer of solution. Therefore a droplet of solution is applied to the grid, blotted and vitrified.
The vitrification is performed by cooling the grid, including solution, down to -180°C, which is below the boiling temperature of liquid nitrogen. This temperature is necessary for amorphous water-ice. Cooling a watery solution below the freezing temperature leads to crystallization of water, which gives the water an order and dilatation.
Both, order and dilatation, have to be avoided to investigate the structure. Order of ice-crystals would lead to increased contrast in transmission electron microscope and therefore reduce available contrast-depth for the substance. Further, the crystallisation leads to dilatation, which would destroy the fragile substance structure.

The process of vitrification of water is solidification without crystallization. It utilizes one of the over 400 known anomalies of water. Water is switching its condition from liquid to solid at about 0°C. For some reasons, the crystallization process in water takes only place in temperature-range between -140°C to 0,5°C [85,86,87,88,89], see Figure 3-8. Thus a liquid aqueous solution can be vitrified by cooling it to -150°C directly (phase XI from Figure 3-8), without passing the temperatures of the crystallization process. However, this is not achievable directly, but cooling has to proceed very fast, so that crystallization can not start. It has been found, that a cooling rate of 10^5 K/s is necessary to avoid crystallisation [90,91].
Such high cooling rates can only be achieved by limiting the mass, that has to be cooled and increasing the heat-transfer-rate of the surface. Limiting the mass or the thickness of the sample is necessary anyhow [92] (compare contrast). Therefore, the solution droplet on the grid is blotted (dry process with a piece of soaking paper). The remaining water dries out at ambient atmosphere very fast. Adequate thickness is reached, when interference fringes appear in the remaining solution. They can be observed with a simple microscope.

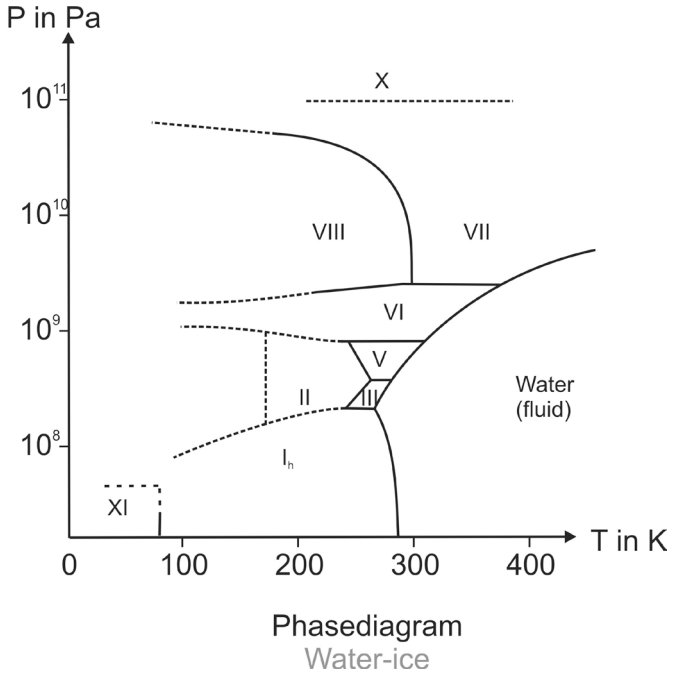

Figure 3-8:
Phase-diagram of water-ice (taken from [93]). Ice-crystals form especially in region I. Amorphous ice possibly in the region XI.

The high heat-transfer-rate can be achieved by using a dense medium of cooling with a good wetting ability. Liquid nitrogen is usually performing a gas-phase at the interface, which inhibits a wetting. Ethane, for instance, is a material, that is liquid

between -140°C and -180°C and offers a good wetting when an object is inserted [91,94].

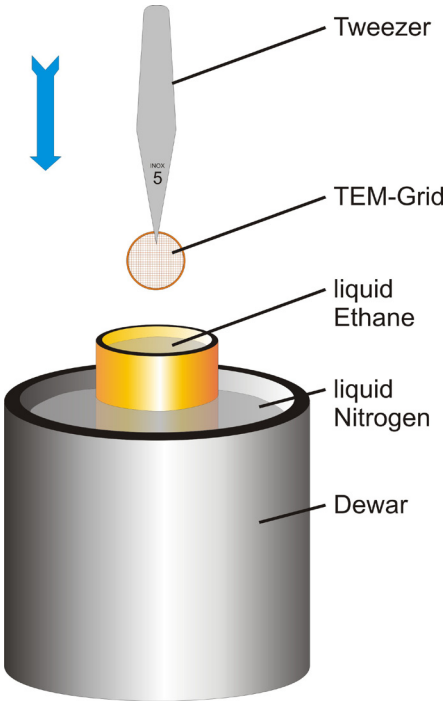

Figure 3-9:
Setup of a vitrification apparatus.

Therefore the sample is shot into a bath of liquid ethane, cooled to -180°C, to vitrify the liquid layer of the sample [85], see Figure 3-9. From that point on, the sample has to be kept cold until it is investigated in the TEM. Therefore a liquid nitrogen Dewar for long term conservation is provided by the FZEM.

3.1.5 Low-Dose imaging

Samples in the TEM are exposed to a high flux of electrons. Fragile samples, especially organic structures, are very sensitive to radiation damage. Cooling of samples with liquid nitrogen prevents them from damage to some extend. A cryo-protection factor $\mathbf{C_p}$ has been found to be ~10 comparing fragility at room-temperature (273 K) and liquid nitrogen temperature (98 K) [95].

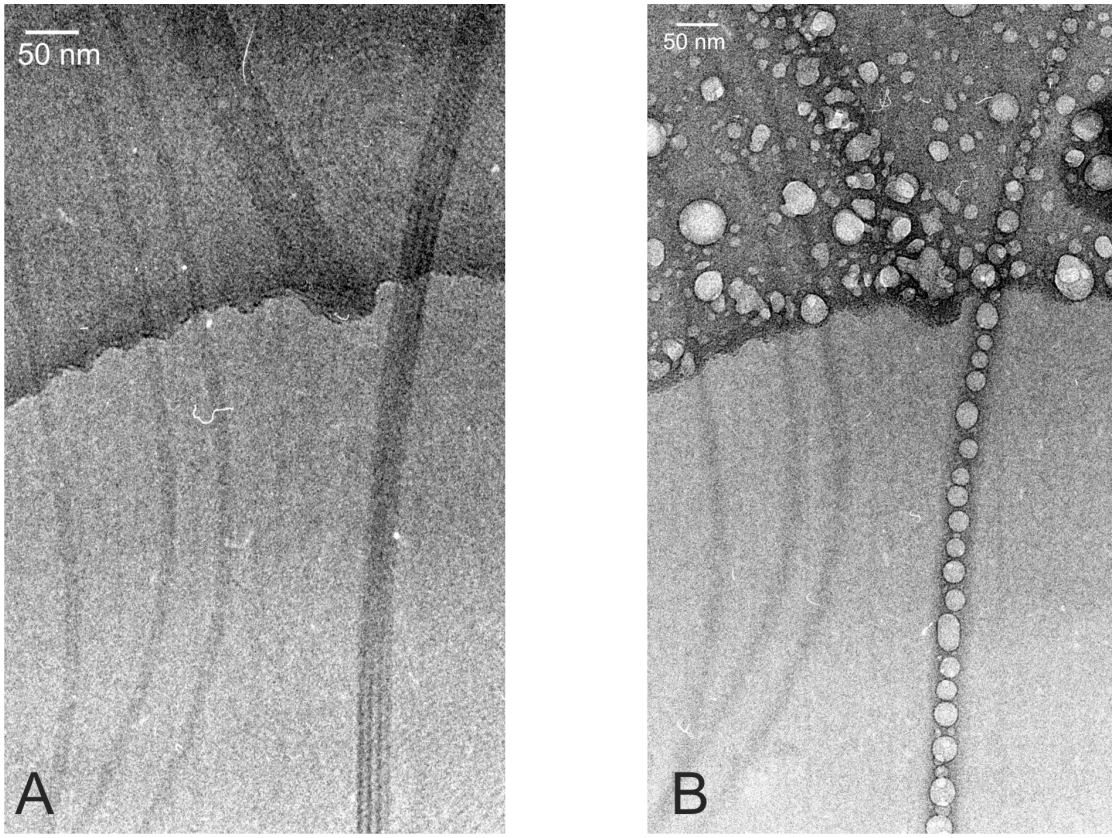

Figure 3-10:
Cryo-TEM images obtained in low-dose
A: N2971, individual and bundled aggregates, first exposure
B: N2975, same region after several exposures

Anyway, fragile structures may suffer from radiation although cooled, as the electron flux increases with magnification [96,97,98], see Figure 3-10. The comparison of images A and B from Figure 3-10 shows the radiation impact. The aggregate bundle in the right-section is clearly observable in image A. Image B, obtained after several exposure times shows the disruption of the fragile aggregates. To avoid serious damage during investigation, which would change or even destroy the structure, it is possible to reduce the exposing time of the sample by using the so called low-dose mode.

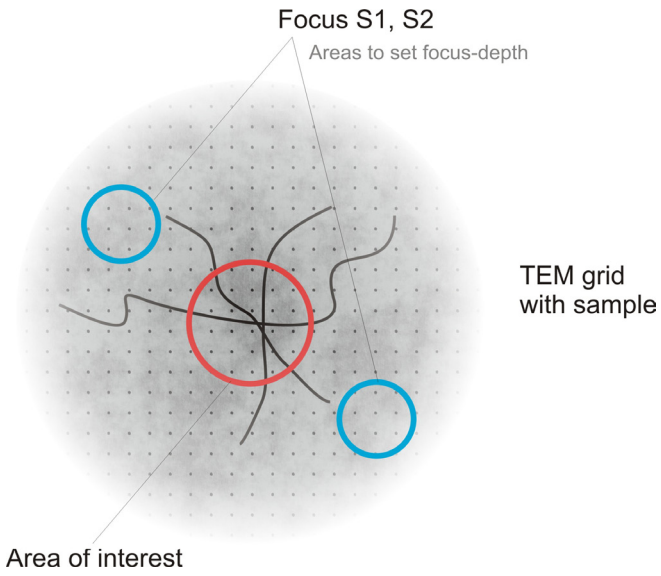

Figure 3-11:
Low-dose imaging-system. Red-circle shows the area of interest, the blue circles show the two spots to set imaging parameters, i.e. focus.

Figure 3-11 illustrates the low-dose method. An interesting spot on the grid is locked in only in the search mode, which is using low magnification, meaning a low electron-dose per sample-area (< 0,01 e/Å²) [99]. Necessary settings of defocus, beam intensity and exposure time (for illumination of the photo-negative) are made on two spots (**S1**, **S2**) aside the area of interest, while in exposure mode (same magnification as during the imaging, > 10 e/Å²). If the values of these parameters differ in **S1** and **S2**, the final values for imaging on the interested spot are found by interpolation. This is necessary, i.e. if the sample is tilted or the thickness of ice varies.

3.1.6 Contrast

There are several contributions for generation of contrast in TEM. Understanding the complex contrast mechanisms is compulsory to assure proper characterization of obtained TEM-images.

Absorption contrast is the first important mechanism to name. Thick or dense (high atomic mass) specimens absorb electrons. That is usually the case for specimens of more than 100 nm thickness. Absorbed electrons do not contribute to imaging, but lead to excitation of specimen atoms and may cause secondary effects [100]. Absorption contrast provides no internal information about structures since the electrons are removed from ray path.

Scattering absorption contrast takes place on thin specimens. The charge density distribution of the specimen causes elastic scattering of accelerated electrons from electronically dense features of the specimen. Specimen features with high charge density scatter the electron beam more efficient. These parts contribute to the imaging with a reduced number of electrons. Anyway, the charge-density distribution of the specimen is recorded, providing internal information of the structure, which is more favorable than absorption contrast.

Phase contrast is strictly applicable only on even thinner specimen, as in the case for cryo-TEM samples. Scattering absorption effects are negligible on such samples. The wave-front of incoming electrons is phase-shifted after passing the very thin specimen and therefore weak phase object. In ideal TEM this phase-shift χ is almost invisible. Due to spherical aberration of the objective lens this shift benefits and the phase contrast increases [101]. The phase contrast can be even stronger if the objective lens is defocused. The phase-shift χ in TEM is given by (if focused to minimal contrast) [102]:

$$\chi = \frac{\pi}{2} \cdot \frac{C_S}{\lambda} \cdot \Theta^4 \cdot C_S \qquad \text{(eq. 3-3)}$$

Θ : scattering angle C_S : spherical aberration

The resulting contrast changes B(q) are given by contrast transfer function (CTF), related to the phase-shift.

$$B(q) = \sin \chi \qquad \text{(eq. 3-4)}$$

The meaning of CTF may be explained by presenting the contrast transfer over a full spatial frequency range.

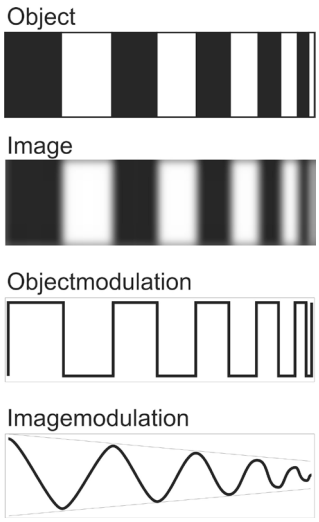

Figure 3-12:
Sketched contrast transfer from object to image. Object modulation compared to image-modulation.

Referring to Figure 3-12, the image of an object shows less contrast. To describe the shown object mathematically one finds the idealized rectangular function. The image-modulation on the other hand, is a damped sinus-function. The damping increases with spatial frequency. In translation to real images, this means a reduced contrast for higher resolutions. The strength of the mentioned contrast-damping is dependent on the lens quality-factor. With defocusing it is possible to shift the CTF towards lower frequencies, resulting in increased contrast in these spatial frequencies. The effect of defocus on the total phase-shift is seen in Scherzer's equation [102]:

$$\chi(R,\Delta) = 2\pi\left(\frac{R^4}{4} - \frac{\Delta R^2}{2}\right) \qquad \text{(eq. 3-5)}$$

with $R = q \cdot \sqrt[4]{C_S\lambda^3}$ and $\Delta = \frac{\delta z}{\sqrt{C_S\lambda^3}}$

q: space frequency R: normalized space frequency

Δ: normalized defocus δz: defocus, distance between focal plane and object plane

The amplitude contrast is neglected in this case as it is the extension of phase contrast to the case of heavy metal staining, used for contrast enhancement or thicker samples.

3.1.7 Defocus

Biological and organic supramolecular structures naturally show weak contrast in TEM, as they consist of elements of low atomic number which show weak elastic scattering interaction with electrons. In addition, amorphous water-ice delivers a grey background. To enhance small intensity differences one makes use of defocusing the objective lens, in this case: underfocus.

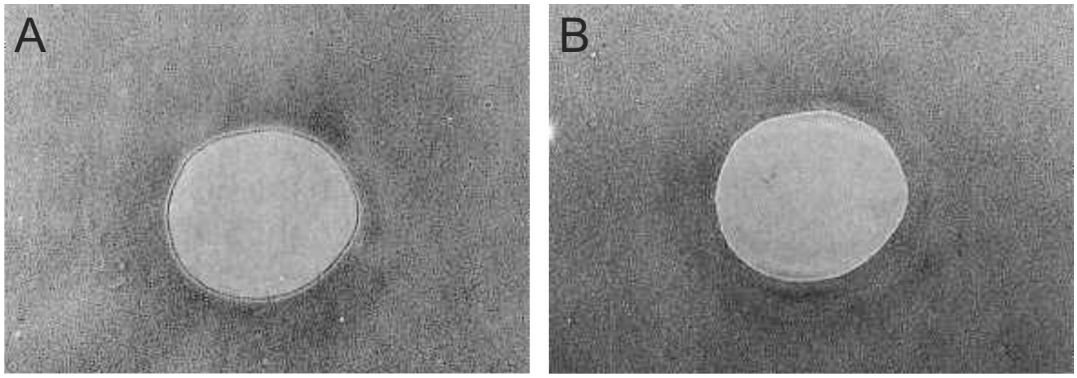

Figure 3-13:
TEM-images of a hole in coal-contrast film 100 000x magnification, obtained holes of approximately 20 nm in diameter, showing Fresnel-fringes, taken from [103]: A: obtained in over-focus (**$\Delta f > 0$**), black fringe. B: obtained in under-focus (**$\Delta f < 0$**), white fringe.

By recording images at a relatively large defocus (i.e. $\Delta f = -1{,}3\ \mu$) electrons become carriers of phase information in addition to amplitude [104], see eq. 3-5. Sample-parts with more material increase phase-shift of the electrons. The phase-contrast information leads to interference with the 0-beam, the unaffected beam. The edges of structures are surrounded by Fresnel-fringes, as seen in Figure 3-13. To highlight objects in TEM-images, that appear darker than the background, the under-focus can be utilized to establish a bright-fringe around the structure.

3.1.8 Scaling

The correct lateral scale in TEM-images is determined by calibration. Although the fixed arrangement of lenses and blends provides a theoretical fixed value of magnification, the proper value is affected by small deviations in acceleration-voltage, magnetic-lense-current inaccuracies and so on. To compensate this mismatch, the proper magnification value is derived from imaging a calibration-sample, such as Heidenreich cross-gratings and coal lattice.

3.2 Microelectrophoresis (Zeta-potential)

Measuring the zeta potential helps to understand colloidal suspensions by revealing the surface-charge of nano-scaled particles in solution. Water is a common suspending liquid, although non-aqueous liquids are used as well. Anyway, the knowledge of viscosity, settling and effective particle size of the sample and its suspending liquid are necessary [105,106].

Surface forces at the interface of the particle and the liquid are very important because of the microscopic size of the colloids. One of the major surface effects is electrokinetic. Each colloid carries a “like” electrical charge which produces a force of mutual electrostatic repulsion between adjacent particles. If the charge is high enough the particles stay discrete, disperse and in suspension. Reducing or eliminating the charge has the opposite effect [107].

Particle charge can be controlled by modifying the suspending liquid. Modification includes changing the liquid’s pH or changing the ionic species in solution. Another, more direct technique is to use surface active agents which directly adsorb to the surface of the colloid and change it’s characteristics – which has been done specifically by wrapping the aggregates with polyelectrolytes.

The diffuse layer can be visualized as a charged atmosphere surrounding the colloid.

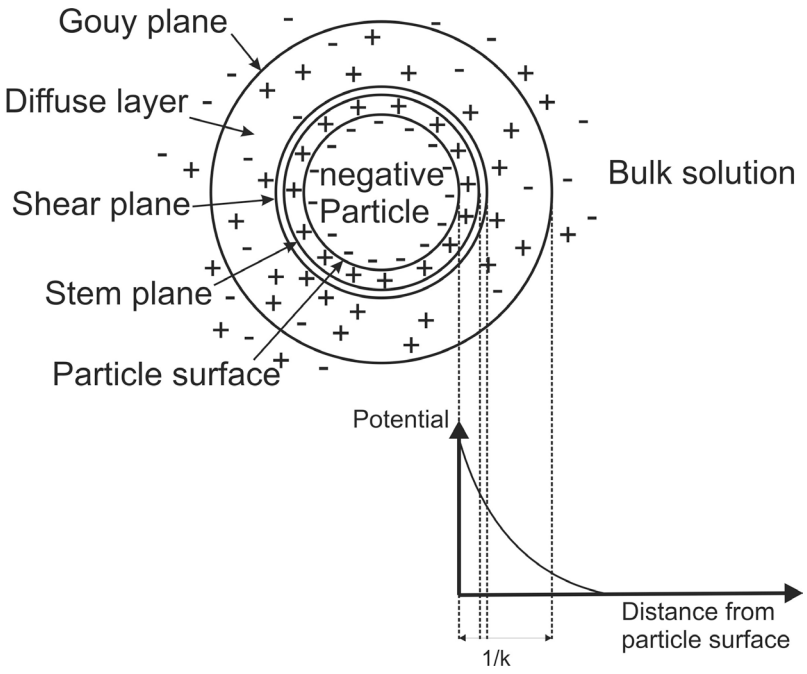

Figure 3-14:
Schematic representation of electric double-layer around particle with negative surface charges.

From Figure 3-14 the relation of this charged atmosphere and the resulting potential is revealed. The potential plot shows the correlation between charge-planes, respectively distance from the particle-surface, and the potential. The diffuse layer is slipped away under influence of external electric field. Yet, the measured zeta-potential is resulting from the effective potential at the Stern-plane [108]. Microelectrophoresis is a method for determination of the zeta potential.

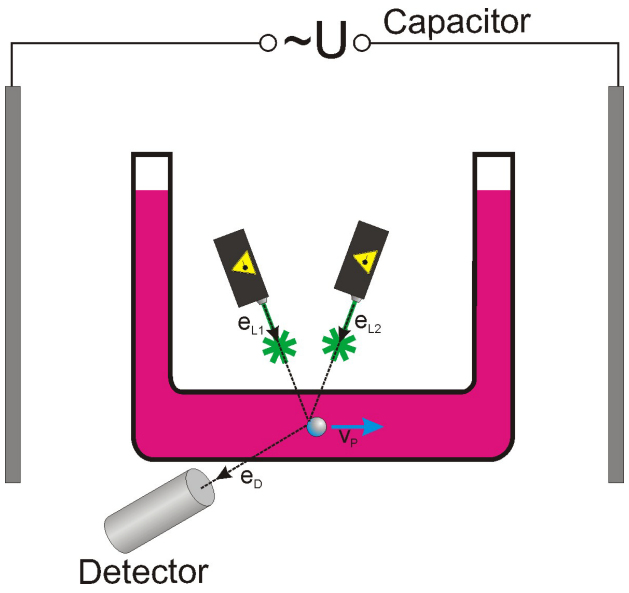

Figure 3-15:
Scheme of laser-Doppler anemometry setup with two laser-beams in zeta-potential measurement-setup. A special U-shaped sample-cell with open ends and capacitor-plates is used. The detector is positioned in a defined angle to the incident laser-beams.

Zeta potential was measured by applying an electric field across the sample solutions using the technique of laser-Doppler-anemometry, which is an optical way of detecting velocities within liquids. Two laser-beams under an angle of φ with respect to each other are pointing to the fluid-stream. A detector behind the sample-cell is collecting the scattering-signal that originates from particles within the solution in the sample cell. Particles of different surface-charge density crossing the laser-interference-field cause alternating scatterings signals with a certain frequency. This frequency is proportional to the velocity of the moving particle [109].

This laser-Doppler-anemometry is obtained several times per second due to the oscillating electric field applied to the cuvette by the capacitor. Charged particles within the solution tend to move according to the field.

The charged particles are entirely suspended by counter-ions, so that from distance the solution appears neutral. Due to field-induced particle-movement the weakly

bound suspension breaks up and reveals the charged particle. The particle movement is enhanced by the oscillating field. Under usage of buffer solutions with known ion content it becomes a measurable size. The resulting particle speed, the mobility, in the field is the obtained measurement. From the mobility $\mathbf{U_e}$ one derives the zeta-potential ζ [39,42].

$$U_e = \frac{2\varepsilon\zeta f(ka)}{3\eta} \qquad \text{(eq. 3-6)}$$

U_e : electrophoretic mobility

ε : dielectric-constant

ζ : zeta-Potential

f(ka) : Henry-function

η : dynamic viscosity

Measurements in this work were carried out on a Zetasizer Nano ZS analyzer with integrated 4 mW He-Ne laser, λ = 633 nm (Malvern Instruments Ltd, U.K.). This device is able to detect particles in sizes from 0.6 up to 6 µm. To elucidate the surface charge of the aggregates and coated aggregates measurements were obtained in phosphate buffer.

100 ml buffer was prepared using 4.27 ml of 0.02 M KH_3PO_4 and 30.49 ml of 0.01 M Na_2HPO_4. Additional 65.24 ml of pure Milli-Q water (Millipak Express 20, 0.22 µm Flter) have been added to fill the volume, delivering the buffer a pH-value of 7.6. All measurements were carried out at 25 °C using folded capillary cells (DTS 1060) in three replicate measurements. Buffer and samples were prepared freshly to provide best results.

3.3 Spectroscopy

3.3.1 Fluorescence spectroscopy

The fluorescence spectrometer is a commercial device, a JASCO FP-6500. It comes with built-in light-source (Xe-lamp UXL-159, 150 W), two grating-monochromators with variable slit-width and detector [110]. The device is setup in a 90°-configuration. The repetitive-accuracy is given with 1 nm. The wavelength-range reaches from 250 nm up to 700 nm.
All parameters concerning scan-speed, slit-width, scan-range and sensitivity can be chosen by the software on the connected computer.
Samples were applied to the device in 3 mm quartz-cuvettes with small bearing, unless otherwise stated.

3.3.2 Absorption spectroscopy

The double-beam absorption spectrometer is a commercial device as well. It is a SHIMADZU UV2101 (revision 2.2, [111]) and is also connected to a computer. The device offers built in light-source, beamsplitter and detector. The accurate scan-range reaches 200 nm up to 650 nm. Measurements were carried out with a resolution of 1 nm. Samples were measured in 1 mm quartz-cuvettes, if not stated otherwise.
Measurements are performed against reference solution, so that the signal difference is caused only by the sample itself.

3.3.3 Time resolved fluorescence spectroscopy

The time resolved spectroscopy was performed using a home built time-correlated single-photon-counter (TCSPC) setup. Sample excitation was performed with 3,5 ps pulses in 80 MHz repetition rate (Spectra pump-laser), dispersed in a subtractive double monochromator. Detection of single-photon counting provides an overall time resolution of 10 ps [112]. All measurements were carried out at room-temperature. Measurements were obtained under the magic angle of 54,7° between polarization of excitation and emission to eliminate influences by rotational depolarisation processes in the sample [113,114,115].

4 MATERIALS

Mens agitat molem.

Mind moves matter.

Publius Vergilius Maro (Vergil), Aeneis 6

4.1 Cyanine dye (C8S3)

Dye aggregates are supramolecular structures of non-covalently bound dyes. Cyanine dyes represent a large group of dyes. From the family of amphiphilic cyanine dyes C8S3 is known to form well-defined tubes. The present work is dealing exclusively with C8S3-aggregates.

The abbreviation C8S3 is a short term for 3,3′-bis(2-sulfopropyl)-5,5′,6,6′-tetrachloro-1,1′-dioctylbenzimidacarbocyanine, which is a cyanine-dye derivative. This derivative is one in a series of amphiphilic cyanine-dyes, that have been investigated during the last decade [20,27,116,117].

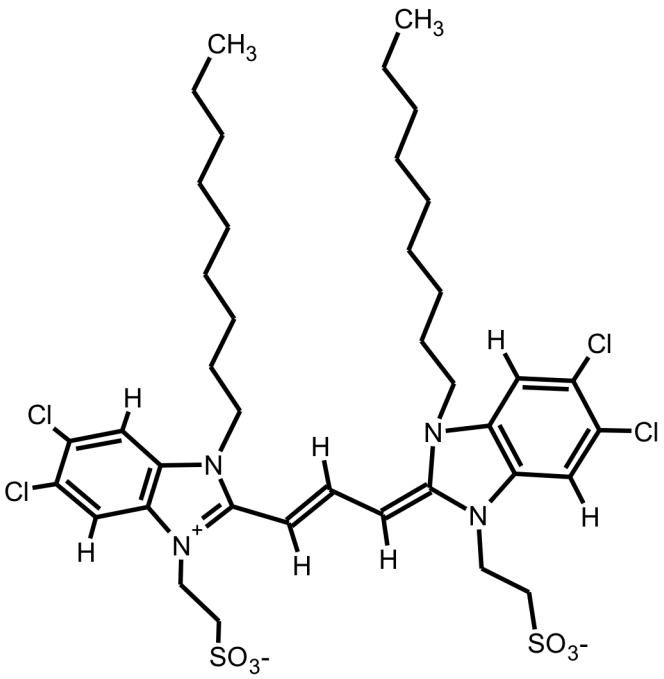

Figure 4-1:
Structure of C8S3 cyanine-monomer [118].

This cyanine-dye derivative has been provided by FEW Chemicals (Dye S 0440, FEW Chemicals, Wolfen, Germany) and was used as received. It is a symmetric molecule. The cyanine backbone including the chromophor, provides a delocalized π-orbital system. In ground-state the chromophor is easily polarisable, which leads to strong attractive van-der-Waals-forces, between neighbouring dyes. These forces are named dispersion forces and lead to formation of stacks of dye molecules.

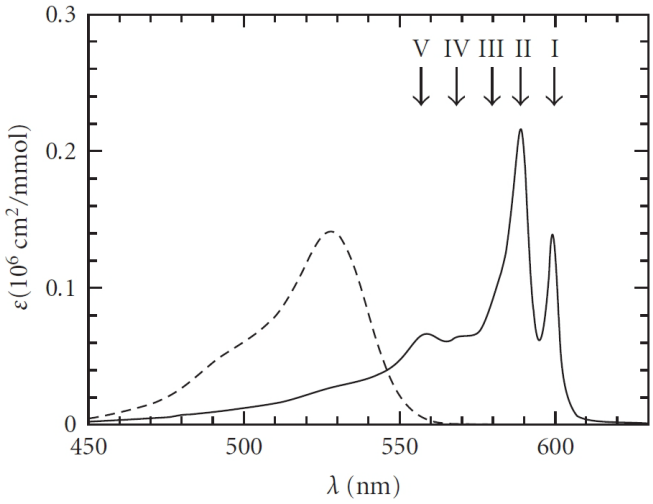

Figure 4-2:
Absorption spectra of C8S3. Dashed line shows the monomer-absorption, solid line shows the aggregate absorption @ 6 X 10^{-5} M [116].

This figure shows the spectral shift of the cyanine dye C8S3 above the critical micellar concentration of 10^{-5} M. The dashed line shows the monomer-absorption for lower concentrated solutions. The solid-line shows the absorption of the higher concentrated C8S3. The dramatic red-shift is the characteristic J-band-shift. The two major-peaks I and II are assignable to the outer and the inner wall of the aggregated tube [30,63,116].

The dye is furthermore zwitter-ionic, offering positive and negative charges at the same time. Overall, the structure appears anionic, since more negative charges are present. Despite the amphiphilic nature of this molecule it is soluble in water and therefore a surfactant.

The following values can be given:

Molarweight:	783.82 g/mol
Molecular Volume:	1.086 nm³
Density:	653.99 cm³/mol
	(derived from comparison to C8O3)

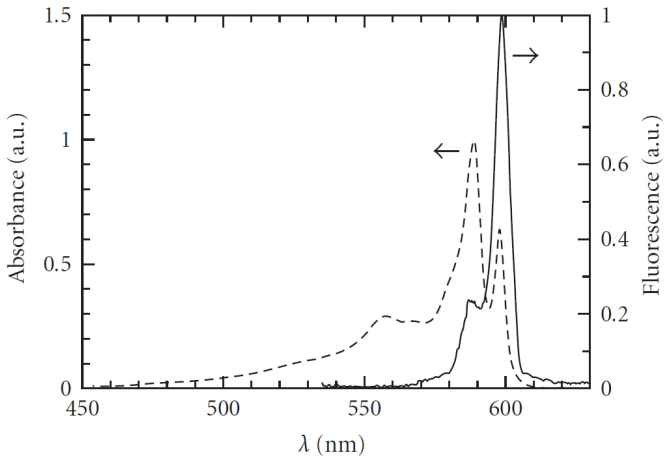

Figure 4-3:
Absorption- and emission-spectrum of C8S3-aggregates.
Solid line shows the aggregate-fluorescence at 6 x 10^{-5} M. Dashed line is the absorption [116].

The preparation of C8S3-aggregates strictly obeyed the following so called **alcoholic route** [26] method to obtain highly reproducible results.

A 2.92 mM stock solution of monomeric C8S3 was prepared by dissolving an appropriate amount of C8S3 (MW = 902.8 g/mol) in pure methanol (Methanol Rotisolv UV-IR-grade, Roth, order-number: T 909.1), while stirring. The resulting solution shows a clear orange colour. In order to prepare C8S3 J-aggregates [26] 130 µl of the C8S3 stock solution were added to 500 ml of ultrapure H_2O (Milli-Q, Millipak Express 20, 0.22 µm filter) and stirred to ensure even mixing. An immediate color change from clear orange to deep pink is observed, indicating the formation of double-walled tubular C8S3 aggregates. The solution was stored in the dark for 24 h before adding an additional 500 ml of H_2O to stabilize the aggregation process, resulting in a final dye concentration of $\mathbf{c_{C8S3}} = 3.36 \cdot 10^{-4}$ M. Solutions of J-aggregates were typically used for experiments within three days after preparation and stored in the dark until then.

4.2 Polyelectrolytes

All PEs were used without further purification unless stated otherwise.

4.2.1 Polydiallyldimethylammonium-chloride (PDADMAC)

PDADMAC is a common polyelectrolyte for layer-by-layer attempts [41,42,105]. It has been purchased at ALDRICH (CAS: 26062-79-3) and comes bottled in 20 wt % solution in H_2O. Both, short and long PDADMAC derivatives have been investigated.

Stock-solutions in a variety of dilutions have been prepared by application of weighted amount of PDADMAC to a certain amount of Milli-Q water (Millipak Express 20, 0.22 μm filter).

Molar-weight:	161.5 g/mol
Chain-length:	~ 1000 monomers short (light PDADMAC)
	~ 3000 monomers long (heavy PDADMAC)
Average M_W:	100 000 – 200 000 (light PDADMAC) g/mol
	400 000 – 500 000 (heavy PDADMAC) g/mol

PDADMAC is known to by a strong polyelectrolyte. It is fully charged at a wide range of pH-value.

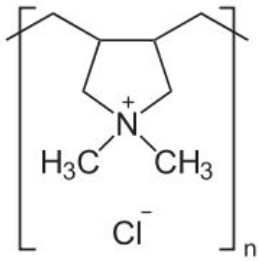

Figure 4-4:
Chemical structure formula of PDADMAC monomer.

4.2.2 Polyethylenimine (PEI)

PEI has been purchased at ALDRICH (CAS: 9002-98-6) and comes bottled 50 wt % in H_2O. Stock-solutions are prepared as mentioned before. It is known as strong polyelectrolyte.

Molar-weight:	43.1 g/mol	
Average M_W	750 000 (by LS) g/mol	Chainlength: 17 000
Average M_n	60 000 (by GPC) g/mol	

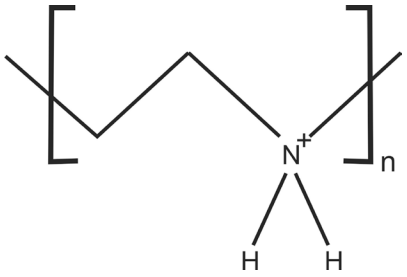

Figure 4-5:
Chemical structure formula of PEI monomer.

In a more detailed view PEI has to be taken as a block-copolymer, because some units branch off. The chain-structure is therefore correctly written as:

$$[NH\ CH_2CH_2]_x\ [N(CH_2CH_2NH_2)CH_2CH_2]_y,$$

where the indices **x** and **y** describe the unbranched and branched units, respectively. Since **x** = 0.9, the the branching is mostly neglected and the PEI described as a linear polymer.

4.2.3 Polyallylamine-hydrochloride (PAH)

PAH is the third polyelectrolyte used in this work and known from layer-by-layer attempts [40,41,42]. It has been purchased at ALDRICH (CAS: 30551-89-4) and comes bottled in 20 wt% solution in H_20. Worksolutions are prepared as mentioned before. It is known as weak polyelectrolyte, offering it's charge only at low pH-solution.

Molar-weight:	57.1 g/mol
Chain-length:	~ 182 monomers
Average M_W:	17 000 g/mol

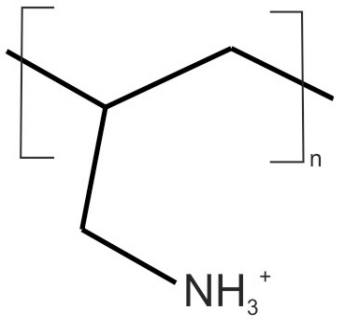

Figure 4-6:
Chemical structure formula of PAH monomer.

The polymer PAH is offering an amine-group. Such groups are known in bio-chemistry to be suitable for labelling with dyes.

4.3 Donor- and acceptor-dyes

For further functionalization a number of dyes has been used as donor or acceptor for energy-transfer from or to the aggregate. These dyes have been covalently bound to the wrapping polycations. The functionalization is therefore only applicable if the aggregate becomes wrapped with a PE. This approach avoids disorder of the well-defined aggregate-structure, but it causes a distance of donor and acceptor in the order of the coating-thickness.

The choice of dye-labels is dependent on the desired spectroscopic overlap with the aggregate spectra. Without a direct energy-transfer from donor to acceptor, i.e. electron-transfer, an efficient transfer, such as FRET, requires a large spectroscopic overlap of donor-emission and acceptor absorption.

4.3.1 Rhodamin B labelled PDADMAC

Rhodamin B is a very common dye and known from several technical applications, like textile colouring, dye-lasers or DNA-marking [119]. Depending on the structure rhodamin offers fluorescence in yellow-green or in the orange-red area of the visible light-spectrum. It also offers a high quantum-yield of up to approximately 95%.

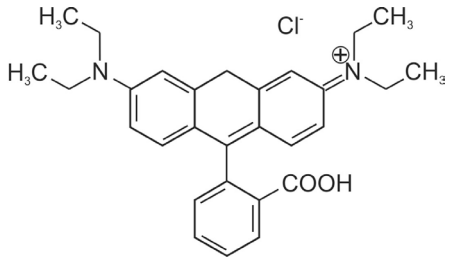

Figure 4-7:
Structure of rhodamin B.

Molarweight:	492.02 g/mol
Formula:	$C_{28}H_{31}ClN_2O_3$
CAS:	81-88-9

Due to sterical hindrance it is not possible to label every single monomer of the entire PDADMAC-chain. The provided PDADMAC-rhodamin B had a labelling ratio of 10%, which means that on average after every 9 or 10 plain monomers one monomer is labelled. The labelling was provided from E. Wischerhoff and A. Laschewsky [120,121].

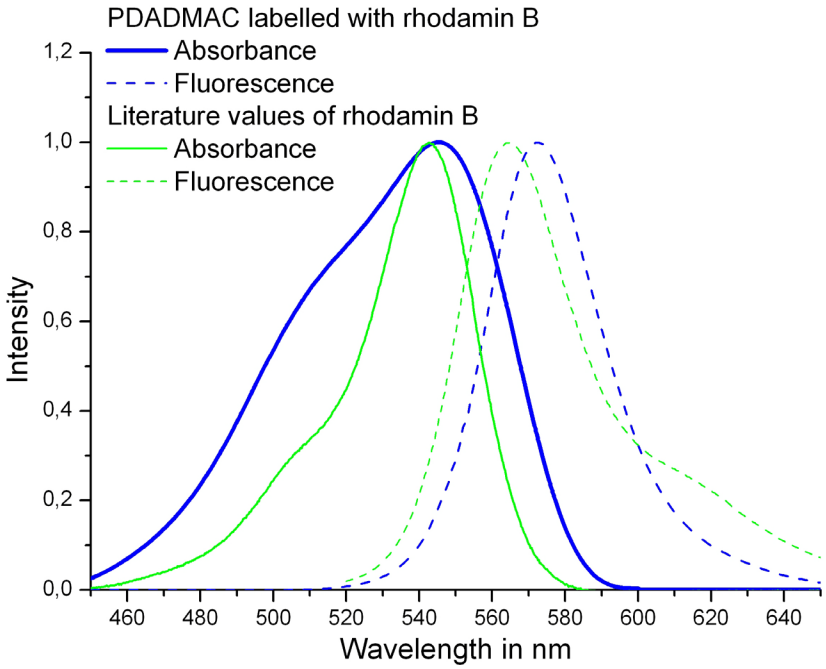

Figure 4-8:
Absorption and emission spectra of rhodaminB labelled PDADMAC. PE-concentration is 10^{-3} M, label-ratio is 10%. Compared are litarature graphs (green) of rhodamin B and measured graphs (blue), excitation wavelength 540 nm.

In Figure 4-8 absorbance and fluorescence spectra of rhodamin B and rhodamin B-labelled PDADMAC are given. In blue the spectra of rhodamin B as labels on PDADMAC are plotted.

In comparison to literature values of pure rhodamin B the obtained spectra are slightly red-shifted. The absorption-peak appears at 544 nm (± 0.5 nm) instead of 540 nm (± 0.5 nm), the fluorescence-peak is located at 574 nm (± 0.5 nm) compared to 567 nm (± 0.5 nm). This shift is due to steric effects, caused by the labelling.

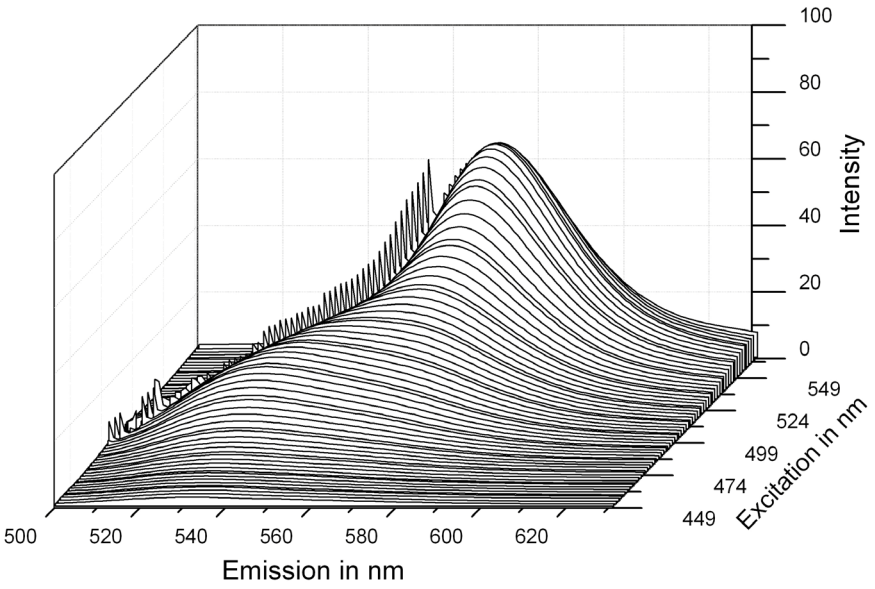

Figure 4-9:
Plot of several emission and excitation spectra of rhodamin B labelled PDADMAC.

However, another more severe characteristic feature was detected, namely a strong shift of emission with excitation wavelength. As shown in Figure 4-9 blue excitation below 500 nm leads to a new fluorescence band with a peak at 530 nm which is not characteristic for rhodamin B. The origin of this blue-response is unclear: It might be a second species that was generated during the labeling procedure or it is due to aggregation of rhodamin molecules. Such aggregation leading to H-aggregates was observed also in other systems. As will be seen in chapter 5.3, this blue emission component will be used for our energy transfer experiments.

4.3.2 Texasred (sulfurrhodamin 101) labelled PAH

Texasred is also a dye from the rhodamin-family.

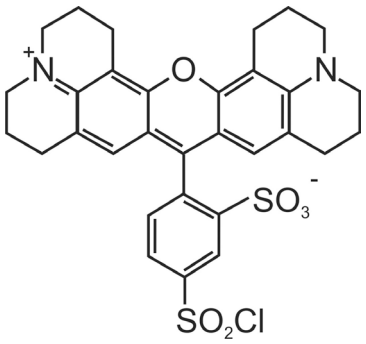

Figure 4-10:
Structure of texasred (sulfurrhodamin 101).

Molarweight:	625.16 g/mol
Formula:	$C_{16}H_{29}ClN_2O_6S_2$
CAS:	82354-19-617000

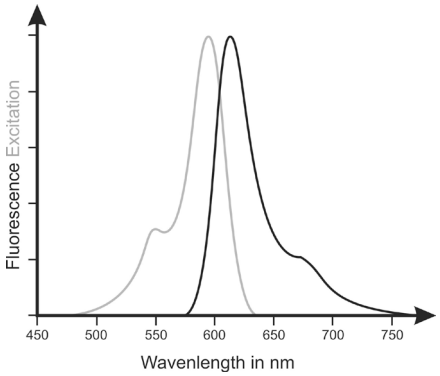

Figure 4-11:
TexasRed spectra.
Grey: Excitation spectra
Black: Emission spectra

The PE PAH offers one amino-group per monomer. Due to steric reasons not every monomer-unit could be labelled. The label-ratio of the used texasred-labelled PAH was in the order of 10% throughout this work. It has been provided by A. Laschewsky and E. Wischerhoff.

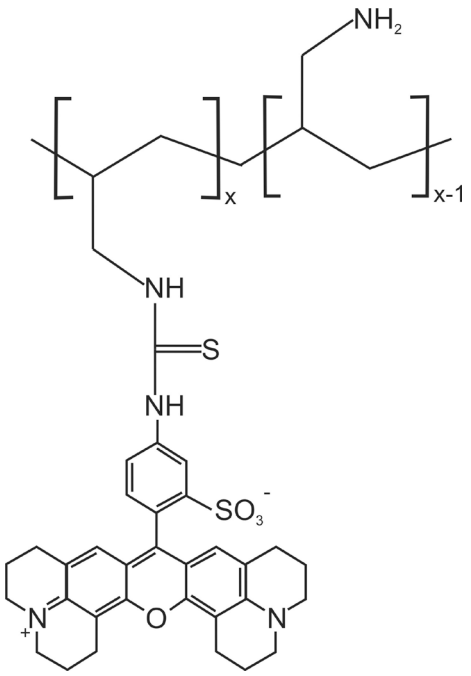

Figure 4-12:
Texasred labelled PAH.
Only a small percentage of the PAH-monomers is labelled ($x \cong 0.1$) in the polymer-chain.

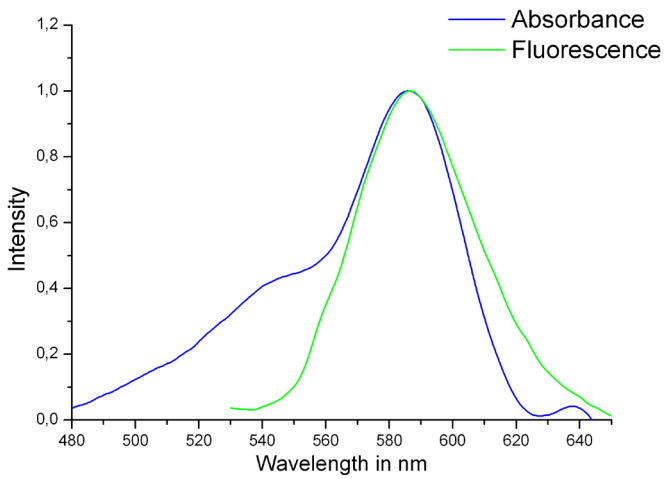

Figure 4-13:
Absorption and emission spectra of texasred labelled PAH.

In direct comparison of the pure dye in solution (Figure 4-11) and as label on PAH (Figure 4-13) one sees that the absorption has shifted approximately 10 nm to the red, which causes difficulties in spectral separation of texasred-PAH and C8S3, see 6.2.3.

4.3.3 Alexa631 labelled PAH

The Alexa631 is one representative of the Alexa-dye-family, that offer high extinction **ε** and radiative-rate-constant **k**. Alexa631 offers maximum absorption at 637 nm (± 0.5 nm) and is therefore very close to the emission band of the C8S3 aggregates.

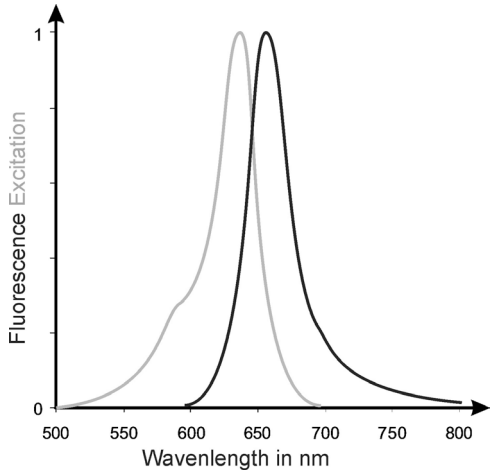

Figure 4-14:
Alexa631 spectra. Grey: Excitation spectra; Black: Emission spectra.

This commercial available dye was covalently bound to PAH by AOKIN, Berlin [122]. In this case the polyelectrolyte was only labelled in a ratio of 100:1, which means, that only every 100 unlabelled PAH monomers one PAH offers a dye label. The following image shows the structure.

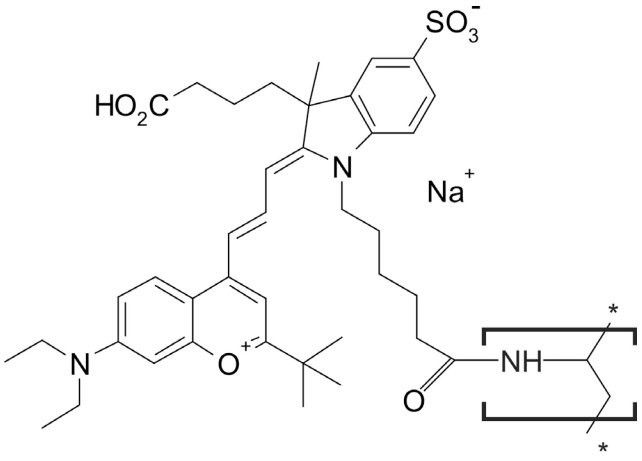

Figure 4-15:
Chemical structure formula of Alexa631 labelled PAH.

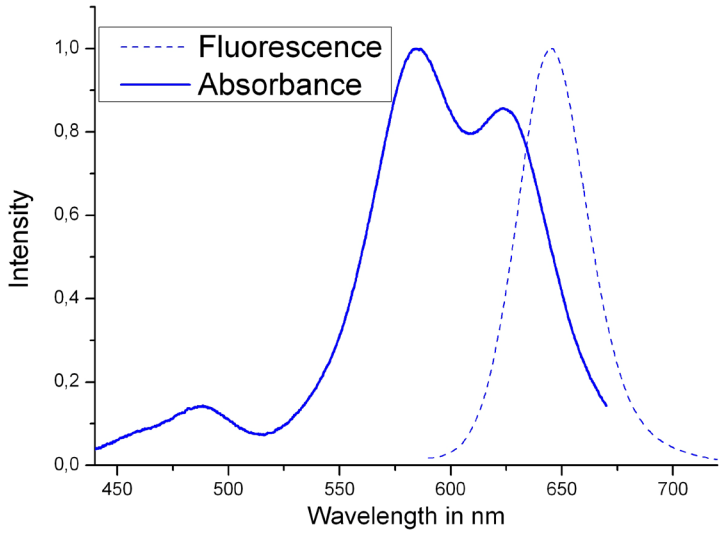

Figure 4-16:
Absorption and emission spectra of Alexa631 labelled PAH.

The comparison of pure Alexa631 in solution and the dye as label on PAH shows significant differences. The absorption of Alexa631 as a label shows a double-peak appearance. It may be explained by different Frank-Condon-factors due to the chemical bond to the PE.

5 RESULTS AND DISCUSSION

勿因一时疏忽

破坏永恒美好

A single act of carelessness leads to eternal loss of beauty.

Old chinese locution

The following chapter is separated into three subjects, each refers to one kind of investigated aggregate development.

1) The first subject is related to uncoated aggregates and highlights mechanical issues that were revealed during investigation under the TEM.

Figure 5-1:
Sketch of aggregate, uncoated, no wrapping nor functionalization.

2) The second subject is the plain wrapping of aggregates. Coating attempts by polyelectrolyte adsorption are investigated. Maintenance of the well-defined aggregate structure and energy-migrating ability are probed by optical spectroscopy.

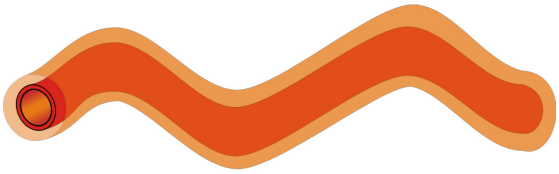

Figure 5-2:
Sketch of plain-coated or plain-wrapped aggregate. No functionalization.

3) In the third subject the functionalization of aggregates is investigated. This research is based on the second subject. To testify if adding functional groups to the wrapping layer enables efficient energy transfer, FRET-effects are probed. Donor-quenching and acceptor-pumping are observed by optical spectroscopy and time-resolved spectroscopy.

Figure 5-3:
Sketch of functionalized aggregate. Shown is a acceptor-functionalization with acceptor-dye-labels in the wrapping layer.

5.1 Pure C8S3 J-aggregates (naked)

5.1.1 Individual aggregates

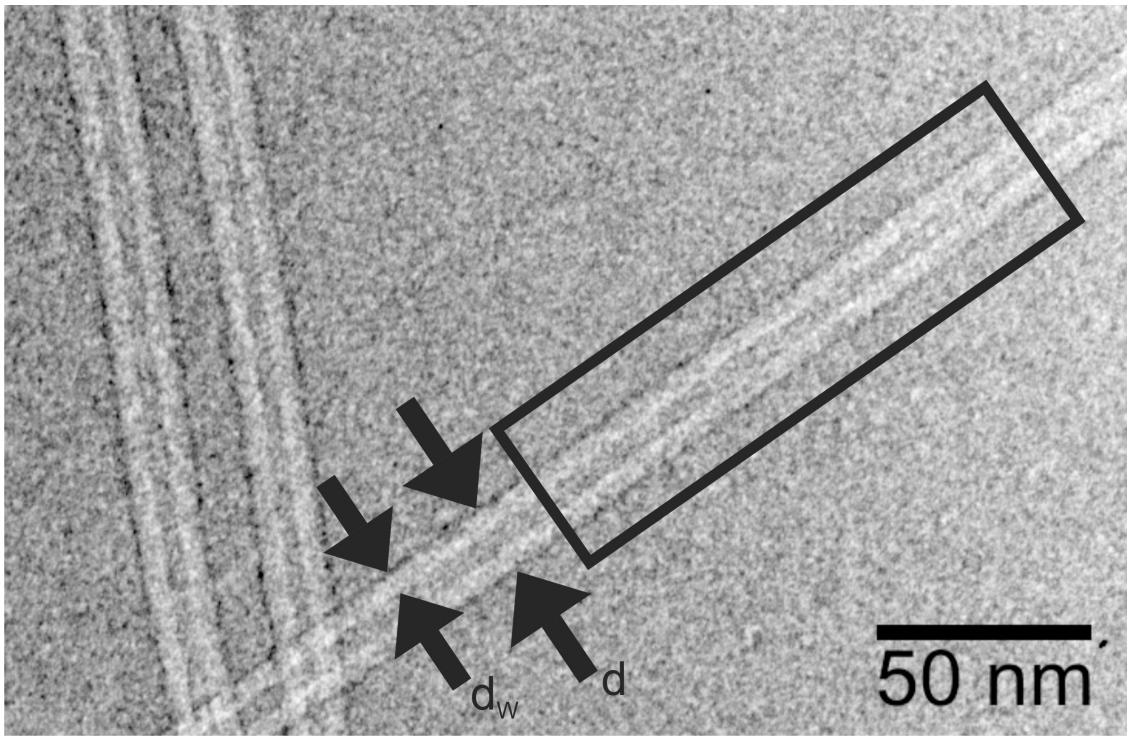

Figure 5-4:
Cryo-TEM negative image of naked aggregates, highlighted diameter d and wall-thickness d_W. Rectangle marks the area utilized for profile evaluation.

The image in Figure 5-4 shows pure C8S3-aggregates (uncoated) in solution, obtained by cryo-TEM. The presented image shows typical appearance. The solutions have a monomer concentration of $3.4 \cdot 10^{-4}$ M and are freshly prepared 3 hours before shock-frosting.

The figure above marks the diameter **d** and the wall-thickness $\mathbf{d_W}$. These values can be determined by extracting the cross-section of an aggregate in a TEM-image. The differences in grey-values can be assigned to background (ice-film), aggregate-wall ($\mathbf{d_W}$) and overall aggregate diameter (**d**). An averaged intensity profile is obtained from evaluating the cross sectional line scan over an extended rectangle (indicated in Figure 5-4). In the plot of gray values the intensity of the background (ice-film) and the walls of the J-aggregate can be well identified. Due to the under-focus Fresnel-fringes appear on the outer edges of the structure which are neglected for the evaluation of the diameter and the wall thickness.

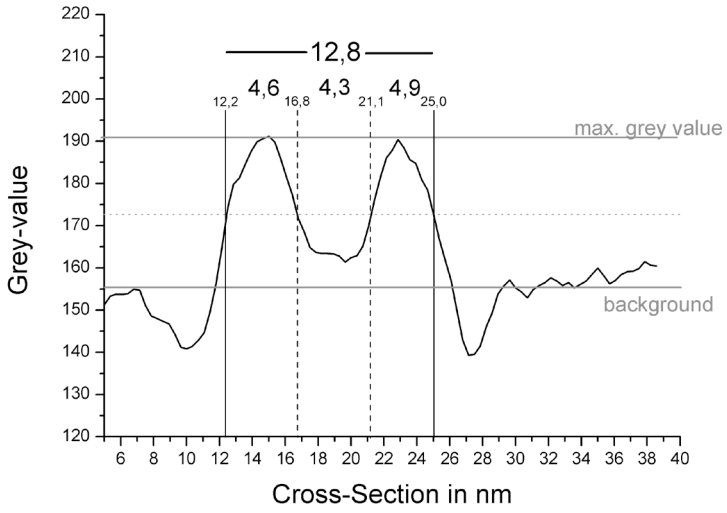

Figure 5-5:
Cross-section averaged through depicted area of TEM image, showing an individual C8S3-aggregate (profile-plot). See text below for further explanation.

From the cross-section plot in Figure 5-5 the total diameter **d** and the wall-thickness $\mathbf{d_W}$ is measured from the grey values that are 50% of the maximum value above the background level. The numerical values are measured as

$d = 12.8 \text{ nm} \pm 0.5 \text{ nm}$

$d_W = 4.8 \text{ nm} \pm 0.5 \text{ nm}.$

These values are in good agreement with known values previously reported [26]. One has to note, however, that slightly different values for the wall thickness and aggregate diameter can be obtained for different under-focus settings of the TEM.

The image in Figure 5-6 is taken at lower magnification and shows an overview of aggregates in solidified, vitrified solution. In this image parts of the quantifoil film is seen with a 1 μm, circular hole at the lower center. The quantifoil film is covered by a thin layer of frozen amorphous aqueous solution which also spans over the hole as described in section 3.2.3.

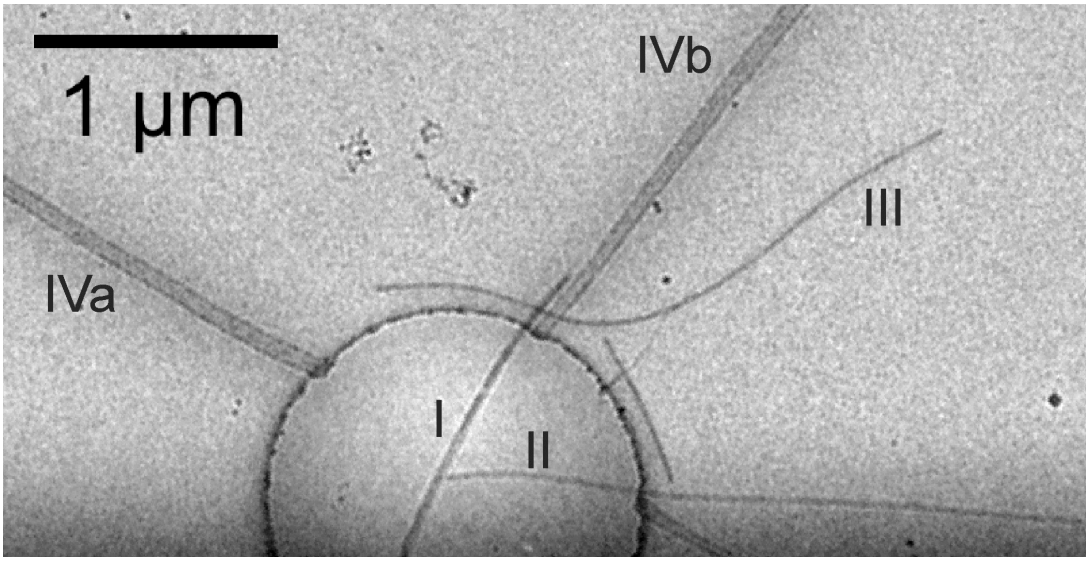

Figure 5-6:
Cryo-TEM image of naked aggregates, low-dose, bright-field, defocus -3 µm, 10 000x magnification, N2967.
Overview image of Quantifoil-hole and surroundings.

In Figure 5-6 an aggregate bundle (I) crosses the quantifoil hole and proceeds even onto the quantifoil-film, providing a length of more than 1 µm. An individual aggregate (II), beginning in the center of the hole shows a length of several micrometers. Another individual aggregate (III) entirely located on the quantifoil-film extends over more than 2.5 µm in length.

The structures marked with (IVa) and (IVb) are imprints on the quantifoil-film. These are marker lines between the holes, but of no interest for the further investigation.

5.1.2 Effects of electrostatic repulsion

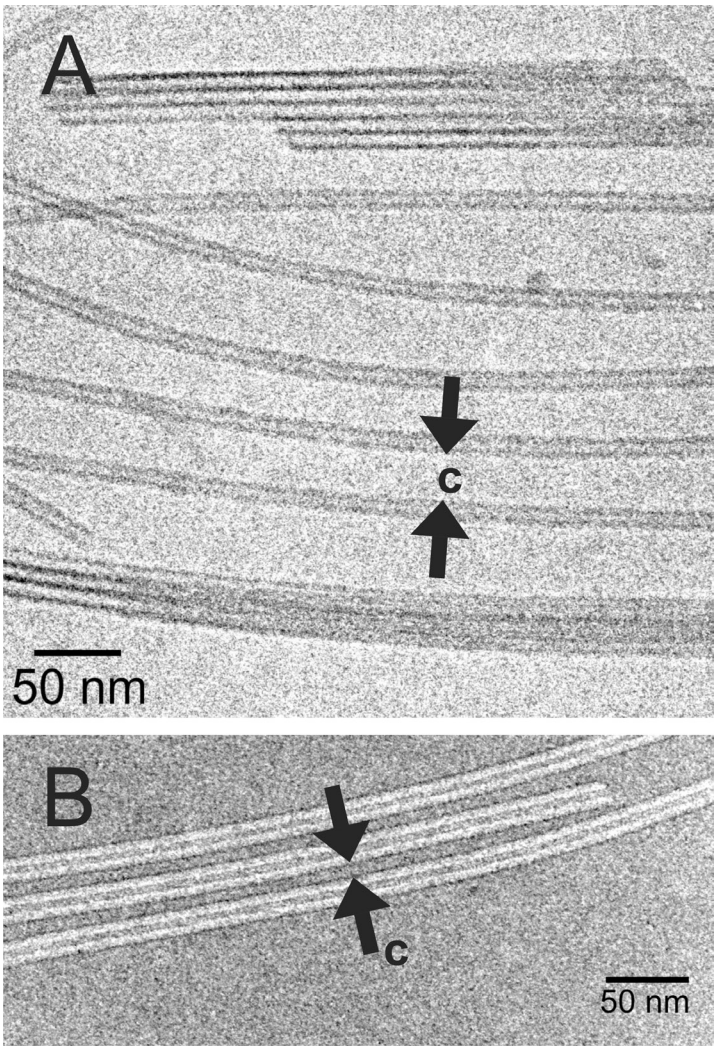

Figure 5-7:
Cryo-TEM images of uncoated C8S3-aggregates shown in positive (A) and negative (B) contrast. The images show the typical parallel alignment of single aggregates within the thin liquid film. A minimum distance for this alignment is observed throughout a multitude of similar images.
60 000x magnification, low-dose, bright-field, defocus -1.3 µm.
A: N3661 (positive)
B: N7105 (negative)

The TEM images from figures above show individual uncoated aggregates. It is interesting to note, that the aggregates either are closely bound to each other, forming bundles like in top-region of Figure 5-7A, or don't touch each other but are separated by a certain distance **c** as indicated in Figure 5-7A+B. Sometimes aggregates are aligned in parallel, as seen in Figure 5-7B. In this case a minimum distance appears with a least value $\mathbf{c_{min}}$. Even though there are cases of crossings und junctions, the

parallel orientation of individual aggregates is obvious. Typical values are found to be:

$$c_{min} = 7 \text{ nm} \pm 1 \text{ nm}$$

These peculiarities seem to be aspects of electrostatic repulsion of individual aggregates.

The observed minimum-distance or separation-distance might be due to the fact, that each surface charge of the aggregates is offering a negative potential, causing a repelling force between them. This electrostatic repelling encounters a mechanical force, which is driving the aggregates together. As mentioned in the chapter 3.1.3 the solution-droplet is blotted to form a very thin film.

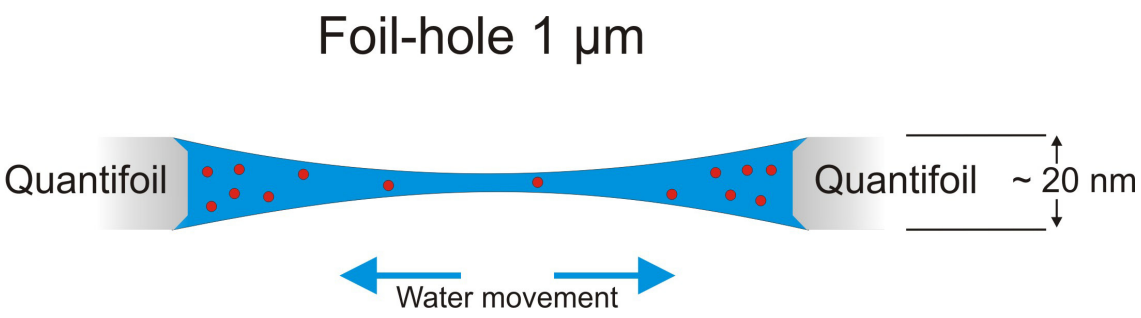

Figure 5-8:
Sketch of cross-section solidified (vitrified) water meniscus in quantifoil-hole with aggregates indicated by red dots. The water drainage encounters a drag force to the aggregate moving them to the boundary of the hole.

The resulting amorphous ice spans over 1 µm quantifoil-holes with a thickness of a few nanometers. During the blotting the water is partially removed from the sample which causes thinning of the freely suspended water film. In this stage the water forms a meniscus in the quantifoil-holes and a drain of water towards the boundary of the hole. This causes the ice on the edges to be thicker and in the middle thinner. With the water drain the aggregates are moved arranging themselves in the thick-ice area but parallel to the hole-edge. The result is a mechanical force caused by the water drain. Unfortunately, it is not possible to calculate the magnitude of this mechanical force, because the speed of the water drain is unknown. However, it is assumed that this mechanical drag force is compensated by the electrostatic repulsion of the aggregates which leads to parallel alignment at a typical distance. The range of the electrostatic force is mainly given by the Debye-length due to the counter ions present in the solution, see chapter 2.2.1 and eq. 2-23.

This drain effect is depicted on images in Figure 5-8.- The images show the area in the quantifoil-holes as well as the quantifoil-film itself. The circular shape of the quantifoil holes is easily recognizable. Aggregates crossing this circular edge are mostly bent to follow the edge. Aggregates that are entirely located in the hole get drained to the edge. Furthermore the grey background appears lighter in the centers of the qauntifoils-holes than on the edges. The grey-scale correlates with the ice-thickness.

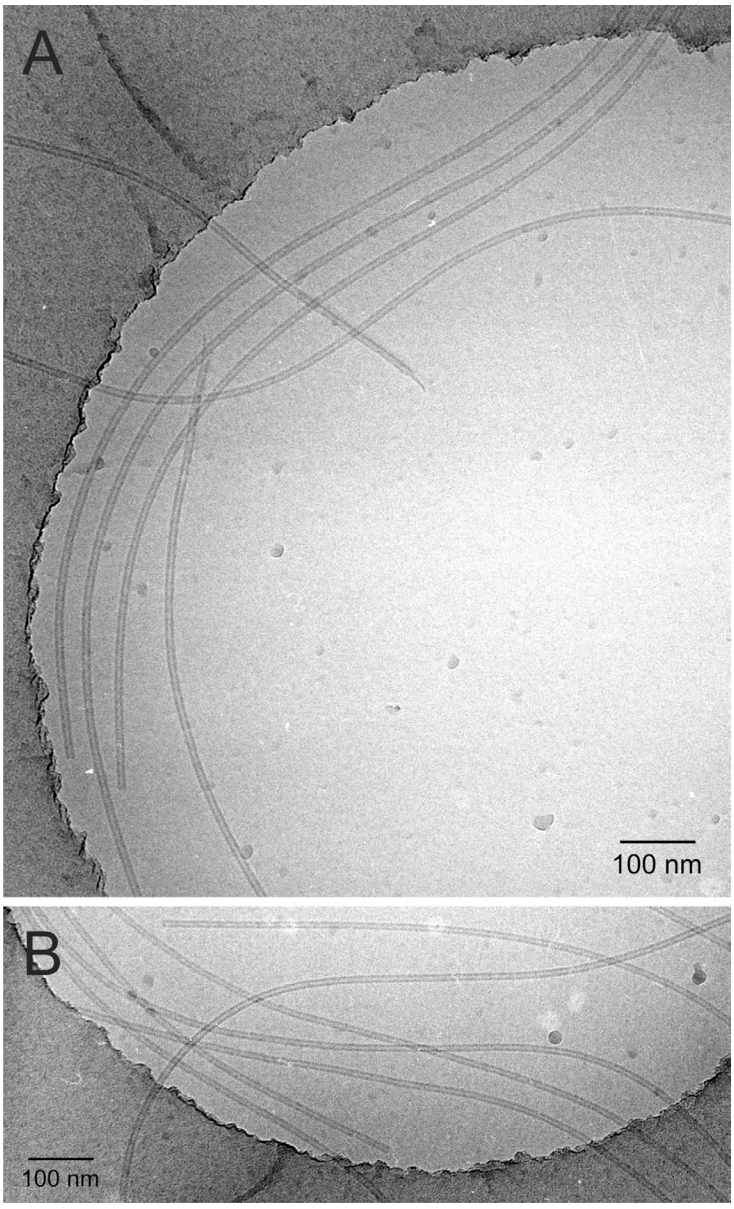

Figure 5-9:
Cryo-TEM images of uncoated C8S3-aggregates at 60 000x magnification.
A: N3657 (negative)
B: N3659 (negative)

Figure 5-9 shows several individual aggregates close to the boundaries of the quantifoil-hole. On these images the drain-effect of the water-meniscus is observable.

In Figure 5-10A+B aggregates crossing each other under a very sharp angle ("twist") are emphasized by the red lines. These twists are typical representatives for a situation where two aggregates approach each other at a distance below $\mathbf{c_{min}}$ without forming bundles. Therefore the twists of individual aggregates are understood as an individual phenomenon and not as a step towards bundle-formation.

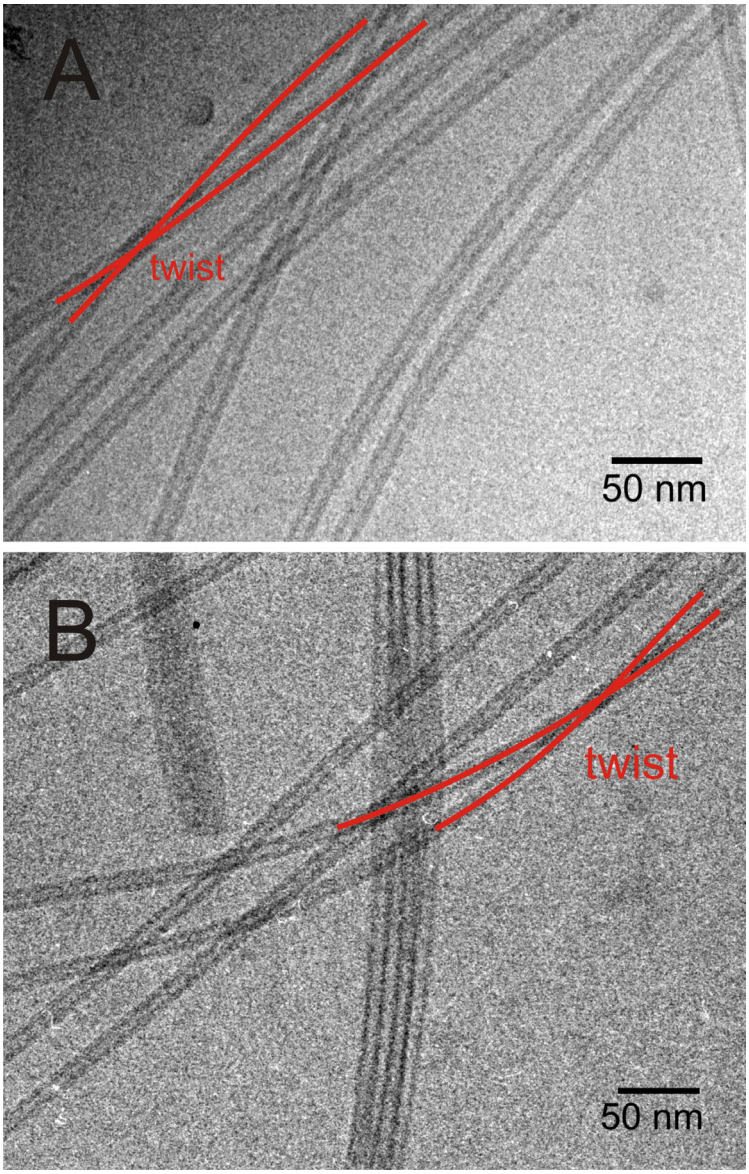

Figure 5-10:
Cryo-TEM images of uncoated C8S3-aggregates showing crossings of tube-pairs. These crossing or twists do not lead to bundling of aggregates.
60 000 magnification, low-dose, bright-field, defocus -1.3 µm.
A: N7115
B: N3653

5.2 Wrapping of J-aggregates with polyelectrolytes

The addition of polycations to aggregates of C8S3 in order to establish a PE-cover is a challenging task. In a simple approximation the aggregates are assumed as long cylinders with homogeneously distributed negative surface charges. This assumption neglects the character of the aggregate structure as a compound of a large number of non-covalently bound C8S3-monomers, each offering a negative charge. The fragile aggregate could be disrupted or disturbed by the polycations if the binding forces between the oppositely charged polymer and the C8S3 molecules is larger than the forces between the dye molecules.

As mentioned in the theory-chapter 2.2, the dominating parameter of the polyelectrolytes which influences the packing-density in the wrapping layer and the overcompensation of the aggregate surface-charge is the charge-density of the polycations. Therefore, to investigate this effect, three different kinds of polycations were used, namely, PDADMAC, PEI and PAH, as described in the chapter Materials. The charge density of this linear PEs can be evaluated from simple geometric considerations and is given in Table 2.

The effect of persistence length is assumed to be small compared to electrostatic forces. Persistence length of the investigated polyelectrolytes are in the same order. Thus the impact of persistence length on the wrapping of aggregates is negligible.

Table 2:
PE charge-density and chain-length.

Polyelectrolyte	Monomer-length	Charge density	Average chain-length n
PDADMAC	5.0 Å	0.20 e/Å	500-3000
PEI	4.0 Å	0.25 e/Å	1400
PAH	2.5 Å	0.40 e/Å	200

The major focus of this work is on the quality and quantity of polycation adsorption on the aggregate surface. A thin, but homogeneous and continuous wrapping is advantageous for any further functionalization by means of dye-labelled PEs.

5.2.1 Discussion of polyelectrolyte-volumes

The aggregate-solutions are mixed with polyelectrolytes to force a PE-wrapping. For this process it is important to find the right ratio of concentrations, where PE concentration is always calculated in terms of monomer concentrations.

Therefore, in the following a brief estimate will be given for the concentration needed for total coverage of the aggregates with a PE layer of a typical thickness of 3 nm. This value is motivated from thicknesses measured for single PE layers in planar polyelectrolyte multilayer films [123] and also in PE coated colloids [124].

The molecular volume of C8S3 is assumed to be in the order of C8O3 and is taken from [54].

Table 3:
List of molecular data used for estimation in wrapping experiments.
PE-concentration, -mass and –volume.

Polycation	**Conc. (Monomer)** [mol/l=M]	**Molar-mass (Monomer)** [g/mol]	**Molecule-volume (Monomer)** ν_0 in [nm³]	**Molar-density** ρ in [g/cm³]	**Molar-volume (Monomer)** [cm³/mol]
PDADMAC	$6.4 \cdot 10^{-4}$	161.5	0.258	1,04	155.29
PEI	$7.3 \cdot 10^{-4}$	43.1	0.086	0,83	51.76
PAH	$7.5 \cdot 10^{-4}$	57.1	0.125	0,76	75.12
C8S3	$\mathbf{3.4 \cdot 10^{-4}}$	**783.8**	**1.086**	**1,20**	**653.99**

The coverage of the aggregates can be calculated easily from simple geometric arguments knowing the molecular volumes of the C8S3-monomer and the wrapping PEs. From 5.1.1 we know the diameter **d** and the wall-thickness $\mathbf{d_w}$ and hence the radii of the idealized hollow-cylinder as sketched in Figure 5-11. The values of inner and outer wall are given with radius $\mathbf{r_i}$ = 2.2 nm, $\mathbf{r_a}$ = 6.5 nm. With the assumption of a 3 nm coating on aggregates one finds the value for the radius of coated aggregates to be $\mathbf{r_{PE}} \cong 9.5$ nm.

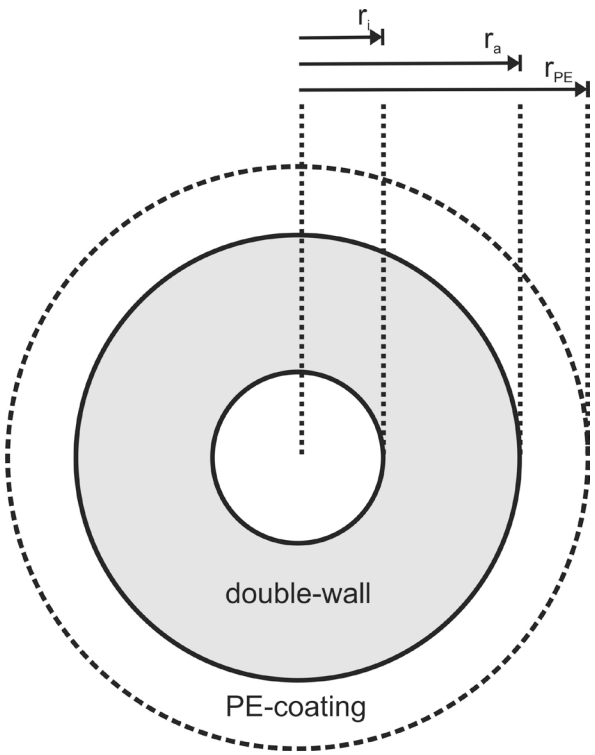

Figure 5-11:
Sketch of cross-section of wrapped aggregate. Depicted are the important radii of inner wall-surface r_i, outer wall-surface r_a and PE-coating surface r_{PE}.

The volumes of the aggregate-tube $\mathbf{V_{aggregate}}$ and the coating $\mathbf{V_{coating}}$ are given by the formula of a hollow-cylinder. With these values one can easily calculate the ratio between the PE and the aggregate volume from the relation:

$$V_{rel} = \frac{V_{coating}}{V_{aggregate}} = \frac{\left(r_{PE}^2 - r_a^{\,2}\right)}{\left(r_a^2 - r_i^2\right)} \approx 1.47 \qquad \text{(eq. 5-1)}$$

The amount of PE needed to cover the entire aggregates is found from this volume-ratio (eq. 5-1). With the molecular volumes $\boldsymbol{\nu_0}$ of the coating PE and of C8S3, and the concentration of C8S3 the number of PE-monomers needed to coat aggregates is given with the equation. The results are listed in Table 4.

The values in this table show just a rough estimation of needed PE concentration for a 100% coating of aggregates under the assumption of a 3 nm thick coating. Since in the beginning of application of higher concentrated PE led to precipitation, concentrations of smaller magnitudes were applied, too.

Table 4:
Estimated consumed PE-amount for entire aggregate wrapping.

Polyelectrolyte	**Relative molecular-volume** $\nu_{0;\,PE} / \nu_{0;\,C8S3}$	**Estimated necessary PE-concentration** [mol/l]
PDADMAC	0.238	$2.1 \cdot 10^{-3}$
PEI	0.079	$6.3 \cdot 10^{-3}$
PAH	0.115	$4.4 \cdot 10^{-3}$

5.2.2 Wrapping with polydiallyldimethylammonium-chloride

Adding a solution of PDADMAC with a concentration of 10^{-5} or 10^{-6} M to freshly prepared C8S3-aggregate solution leads to no changes in the absorption spectra. The usage of higher concentrated PDADMAC leads to precipitation: While 10^{-4} M PDADMAC took a few minutes to fall out C8S3, the effect took place immediately with 10^{-3} M. Concentrations below 10^{-7} M showed no effect. The application of PDADMAC with concentrations at 10^{-5} M and 10^{-6} M, respectively, provided assumingly stable solutions.

The plot in Figure 5-12 shows absorption spectra of C8S3 aggregates before and after addition of PDADMAC at various concentrations. PDADMAC of two different molecular weights was also used: heavy (long) and light (short). Light PDADMAC is providing an average chain-length of approximately 1000 monomers, heavy PDADMAC is three-times longer.

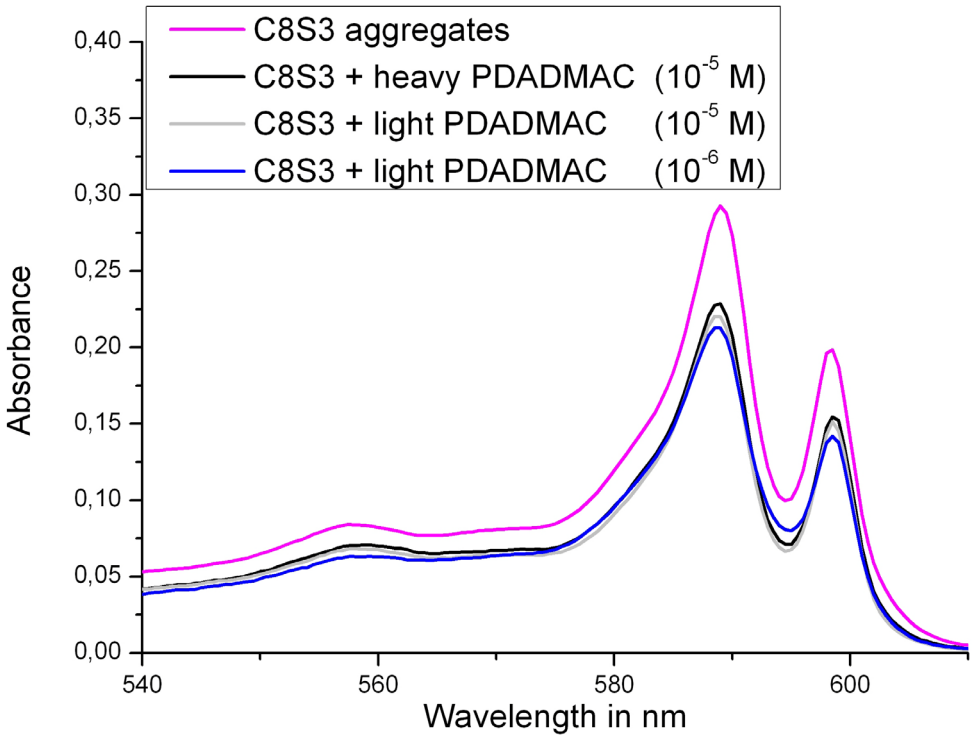

Figure 5-12:
Absorption-spectra of PDADMAC-wrapped C8S3 aggregates. Compared are uncoated C8S3 aggregates, wrappings with short and long PDADMAC-chains and higher and lower PDADMAC-concentration.
The spectra are corrected to equal C8S3-monomer concentration.

From Figure 5-12 it is clearly seen, that the addition of PDADMAC causes no significant spectral changes. The peaks that are characteristic for the tubular J-aggregate remain at same wavelength and are not broadened; only the entire absorption is slightly reduced by approximately 20%. This indicates, that the morphology and the well ordered molecular structure of the aggregate stays in shape. Usage of long or short PDADMAC revealed no difference in the absorption, nor did the usage of 10^{-5} or 10^{-6} M respectively.

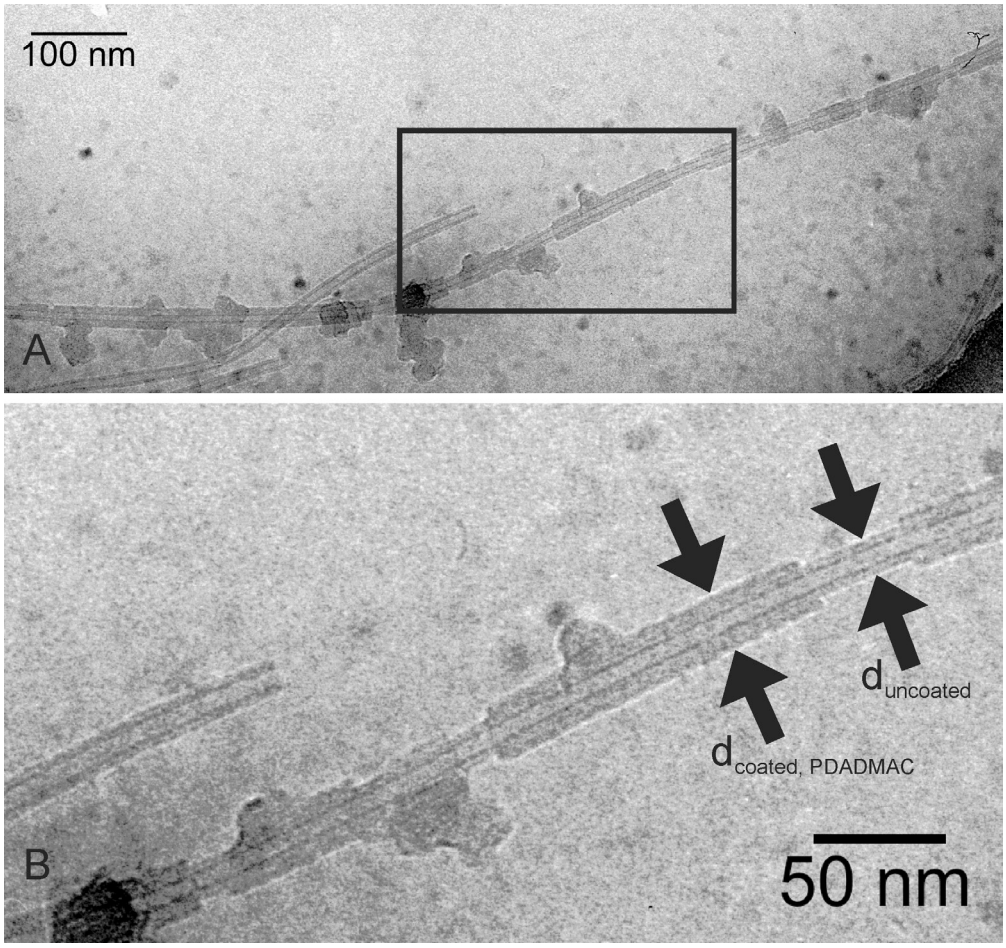

Figure 5-13:
Cryo-TEM images of C8S3 aggregates wrapped with heavy PDADMAC. PE-concentration 10^{-4} M; obtained 60 000x magnification, low-dose, bright-field, defocus -1.3 µm.
A: N8644
B: zoom-in of N8644 in highlighted area of image A

Typical cryo-TEM images of C8S3 aggregates wrapped by PDADMAC are shown in Figure 5-13. From the cryo-TEM images one can see that wrapping occurs, but only on some of the aggregates and only piece-wise in a small number of fragments. Apparently, the diameter of the wrapped parts is very homogeneous and regular, both within one fragment and between the fragments. From the images one can derive the values for diameter of uncoated aggregates **d** and PDADMAC-wrapped aggregates $\mathbf{d_{coated;\ PDADMAC}}$ as:

$$\mathbf{d} = 13 \text{ nm} \pm 1 \text{ nm}$$

$$\mathbf{d_{coated;\ PDADMAC}} = 21 \text{ nm} \pm 1 \text{ nm}$$

Obviously, the diameter of uncoated segments of the aggregates is unchanged. This finding is in accordance with the observation that the absorption spectra do not change with adsorption of the PDADMAC.

The wrapping of single aggregates occurs only partly, so vast areas of aggregates are still uncoated. From the cryo-TEM images one can derive the fraction of the length of aggregates that is covered by PDADMAC. By measuring the total aggregate-length $\mathbf{L_{tube}}$ and the total length of coated parts $\mathbf{L_{tube,\ coated}}$ one finds:

$\mathbf{L_{tube}} = 28.0\ \mu m \pm 0.6\ \mu m$

$\mathbf{L_{tube,\ coated}} = 8.6\ \mu m \pm 0.6\ \mu m$

The average length of the coated part is given by

$\mathbf{L_{tube,\ coated,\ av.}} = 215\ nm \pm 5\ nm$

From these numbers we get an estimate of the mean coating fraction of 30% (± 3%) (overall). This number has to be compared to the expected volume fraction of coating. Using the equation 5.1 and the coating radius of $\mathbf{r_{PE}} = 10.5$ nm one calculates a fraction of $\mathbf{C_{theo}} = 27\%$, which is very close to the observed value of 30%. Furthermore the TEM-images show globular objects (blobs) which are assigned to the polyelectrolyte. The volume of these PE-blobs was omitted in the estimation.

One may argue that the very smooth and regular surface is very suspicious because it has almost the same thickness as the wall of the naked aggregate. One may assume that the positively charged polyelectrolyte adsorbs flat on the aggregate providing a positive coating for further adsorption of another double layer of C8S3-Monomers. In result, a second double-walled tube would grow on the C8S3-aggregates. Such a coaxial twin-double-walled-tube would also deliver a smooth surface and show a wall thickness of two times 4 nm, which is surprisingly close to the values observed in the images above. However, the second bi-layer of dyes ought to have different molecular structure and hence different absorption spectra. It is known that changes in aggregate diameter by similar amounts lead to very different spectra [56]. From these spectroscopic arguments we exclude such a double layer dye structure and conclude that the observed coating is purely composed due to PDADMAC.

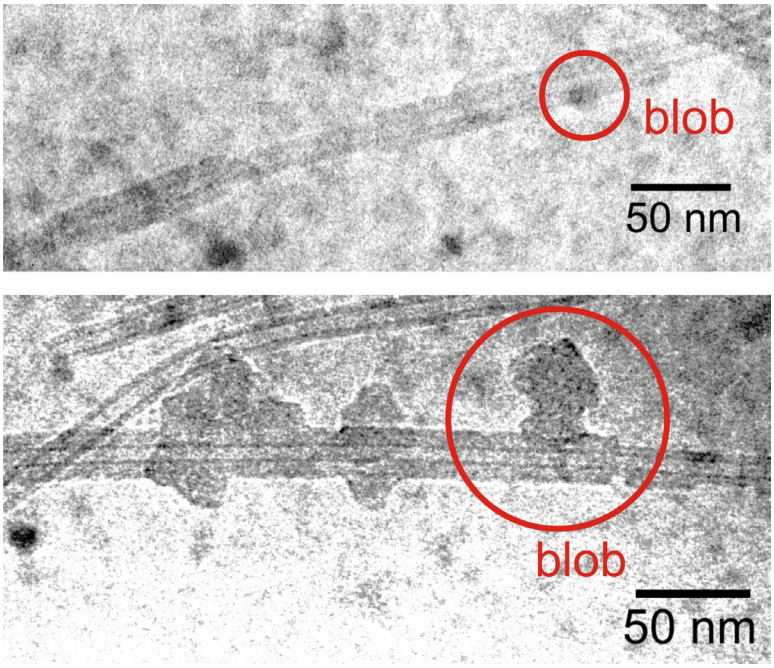

Figure 5-14:
Cryo-TEM image of vitrified solution of C8S3-aggregates with light PDADMAC. PE-concentration 10^{-4} M.
Images N8645 + N8646, low-dose, bright-field, 60 000x, defocus -1.3 µm.

It is an interesting observation that in most cases the coated segments are accompanied by blobs of polyelectrolyte, as indicated in the cryo-TEM images, see Figure 5-14. This widespread appearance of blobs on all coated fragments gives rise to the assumption that the PE adsorbs on the aggregates in a coiled state. The PE-chain of a few thousand monomer-units adsorbs at the aggregate-structure with an arbitrary part of the chain. When attached to the aggregate the globular PE is assumed to disintegrate and adsorb more or less completely on the oppositely charged aggregate surface, as sketched in Figure 5-15. If the PE-chain from the globule is not entirely adsorbing on the aggregate, the globules remain present on the coated fragment.

The size of the globules can be related to the length of the PDADMAC chains. For the rough estimate of the blob volume two extreme cases may be considered:

a) The volume is given by a dense packing of PDADMAC monomers, which gives a lower limit. In this case, for **N** = 3000, a mean diameter of a spherical globule would be 6 nm.

b) The volume is given by the radius of gyration $\mathbf{R_G}$, as obtained for an ideal polymer chain with a persistence length of **a** = 2.5 nm. In this case, blob size

is given by $\mathbf{R_G}$ and the number of Kuhn-segments $\mathbf{N} = 1200$ one obtains $\mathbf{R_G} = 35$ nm.

Due to the charges PEs are in a more swollen state than uncharged polymers. In a simple approximation the charges lead to an increase of the persistence length. In our case one may expect an electrostatic contribution of counter-ions, that decreases the the PE-swelling [125]. The observed sizes of blobs fit to the gyration radius $\mathbf{R_G}$.

A rather high concentration of counter-ions is present in the solution and the chains are not in a fully extended state but form globules.

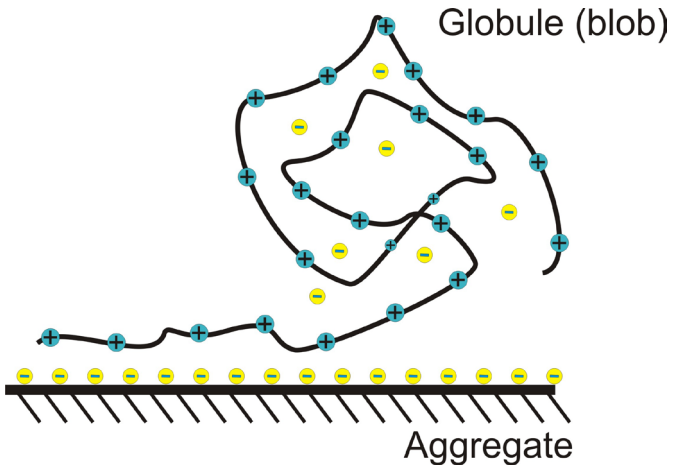

Figure 5-15:
Sketch of PE-globule adsorption on aggregate-surface. A PE-chain in solution appears in globules due to presence of counter-ions. Loose ends of the chain adsorb on a charged surface, reducing the amount of PE in the globule.

The average blob-to-blob-distance is found to be approximately 180 nm.

For the case of PDADMAC (heavy) the chain-length is 3 000 repeat units on average, each unit of 5 Å, providing an overall length (averaged) of 1 500 nm.

The coated fragments have been found to be of average length $\mathbf{L_{tube,\ coated,\ av.}} = 215$ nm. Within the coating on these fragments approximately 77 600 monomer-units are consumed, which is almost 26 PE-chains.

5.2.3 Wrapping with polyethylenimine (PEI)

The polycation PEI is a very strongly adhesive polyelectrolyte due to the different amin-groups. It is very often used as the first layer in the preparation of layer-by-layer assemblies due to the strong adhesion to different substrate materials [126,127,128,129]. It has also proven to form layers at colloids in solution [124]. Therefore, it was an interesting question whether PEI forms thicker coatings on the tubular aggregates.

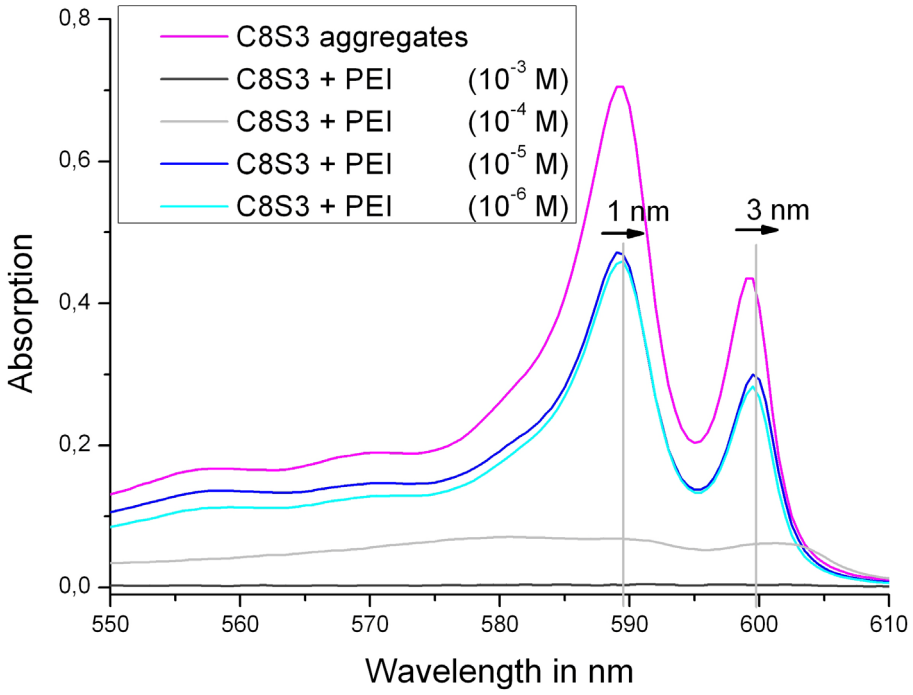

Figure 5-16:
Absorption-spectra of PEI-wrapped C8S3 aggregates. Compared are uncoated C8S3 aggregates and wrappings with PEI in various PE-concentrations. The molarities given in the table depend on the monomer-concentration of PEI.

Figure 5-16 shows the interesting part of the absorption-spectrum more detailed. On the major J-band-peaks a slight peak-shift is perceivable. At concentrations of PEI higher than 10^{-5} M the spectra are significantly reduced and the peaks are broadened. This broadening is typical for very high degree of disorder within J-aggregated systems [130]. The reduction of absorbance is explained by precipitation of large flakes that can be seen by naked eyes. For the concentration of 10^{-4} M there is still a weak tendency of J-bands observable, although the intensity loss is drastic. For the highest concentration of 10^{-3} M there is no optical activity observable anymore due to precipitation. Therefore, only samples with PEI concentrations in the range of 10^{-5} to 10^{-6} M were considered for cryogenic TEM inspection.

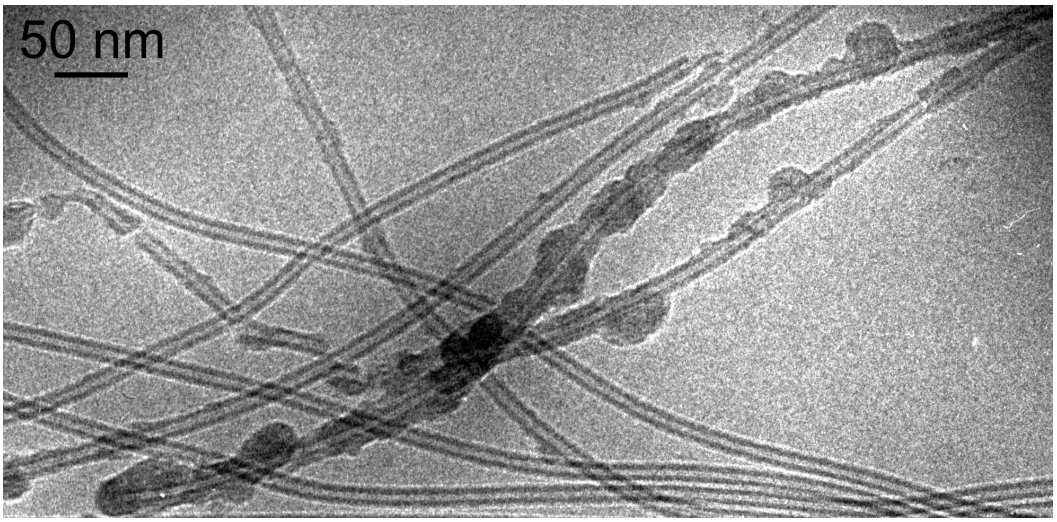

Figure 5-17:
Cryo-TEM image N9313 low-dose, bright-field, 60 000x, defocus -1.3 µm.
Vitrified solution of C8S3-aggregates and PEI @ 10^{-5} M.

Figure 5-17 shows typical appearance of PEI-wrapped C8S3 aggregates. The wrapping is easily to distinguish from uncoated aggregates. In contrast to previously discussed PDADMAC-wrapping, PEI shows a very uneven surface. Additionally the presence of blobs is observed, too.

A detailed investigation of cryo-TEM images delivers insights on typical PEI-wrapping features.

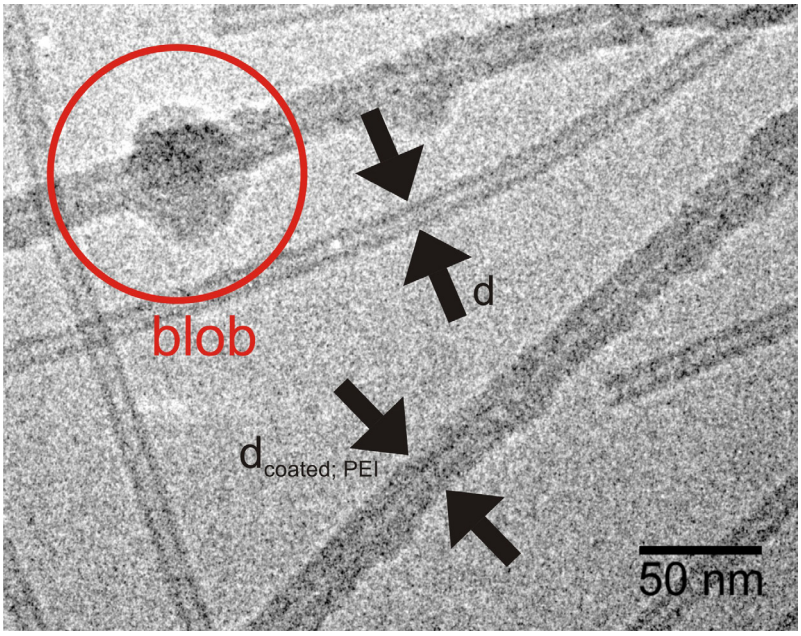

Figure 5-18:
Cryo-TEM image N9300, low-dose, bright-field, 60 000x, defocus -1.3 µm.
Vitrified solution of C8S3-aggregates and PEI @ 10^{-5} M.

In analogy to the experiments with PDADMAC, the TEM-images of PEI wrapped aggregates reveal uncoated and coated aggregates. Since uncoated aggregates are very homogeneous with a well defined diameter, the parts that are covered by PEI can easily be distinct from the uncoated aggregates. The aggregates coated with PEI show an irregular diameter and often huge blobs attached to the surface.

From the TEM-images we derive values for the diameter of uncoated aggregates **d** and PEI-wrapped (PE-conc. 10^{-5} M) aggregates $\mathbf{d_{coated;\ PEI}}$ (neglecting the blobs):

$$\mathbf{d} = 13 \text{ nm} \pm 1 \text{ nm}$$

$$\mathbf{d_{coated;\ PEI}} = 18 \text{ nm} \pm 1 \text{ nm}$$

Further inspection of the TEM images reveals that approximately a fraction of 4% (with respect to the total tube length visible in the images) of the aggregates are coated with PEI. Using a diameter for the coating of 18 nm and the PEI concentration of 10^{-5} M the coating fraction can be evaluated by eq. 5-1 to be $\mathbf{C_{theo}} = 1.9\%$. This is of same order of magnitude as the value obtained from the TEM images. For the latter, the error can be rather high and cannot be put in numbers because only small fractions of the samples are inspectable by the TEM and blobs are neglected anyway.

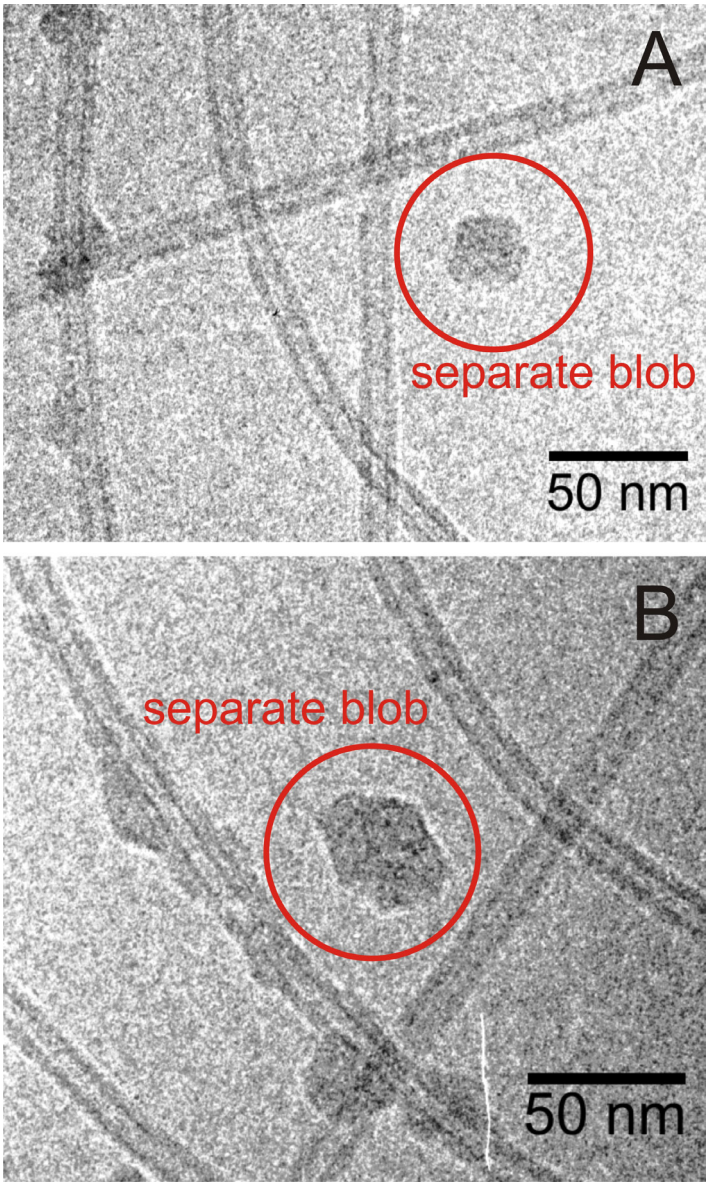

Figure 5-19:
Cryo-TEM image N9301 + N9302, low-dose, bright-field, 60 000x, defocus -1,3 µm. Vitrified solution of C8S3-aggregates and PEI @ 10^{-5} M.

Figure 5-19 shows images where separate blobs can be found (highlighted by red circles). It is assumed that these blobs are pure PEI globules. They are found irregularly between the aggregates and are of similar size and contrast as the blobs found within the PEI coating along the aggregates.

The coating itself is not smooth but interrupted by such blobs and extrusions. The difference between a thick coating and a blob is not always distinguishable. There are some coated fragments that show no blobs at all. An explanation for these blobs can be made in analogy to that given in chapter 5.2.2. The polycation PEI has typically chain-lengths of 5 000 to 17 000 monomers, which is larger than in case of

the PDADMAC. This may explain why in case of PEI the adsorption at the aggregate surface is more irregular: if the mean size of the adsorbed globules is larger, than more parts remain coiled or uncoasted even when the surface is already covered by evolved PEI.

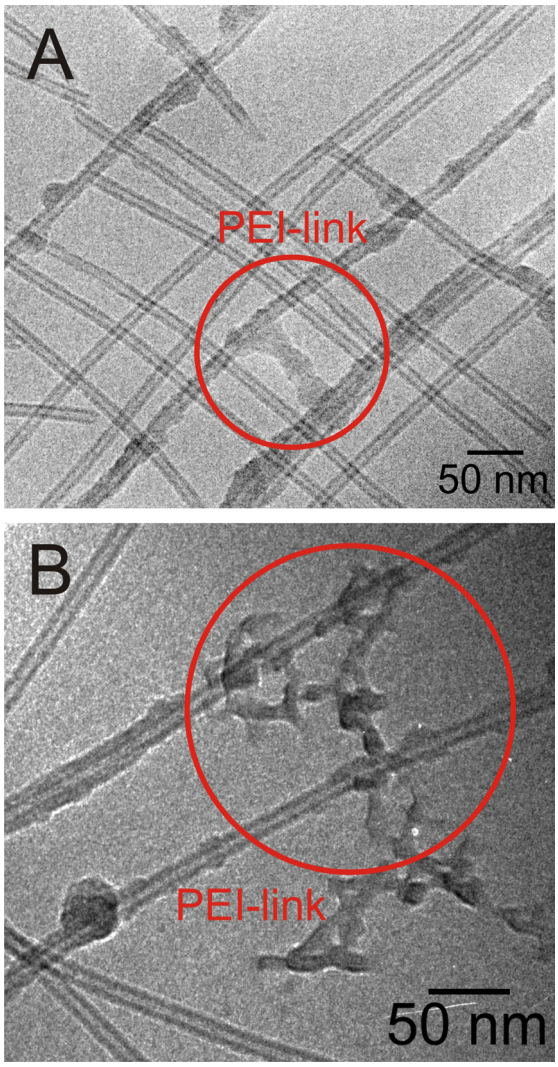

Figure 5-20:
Cryo-TEM image N9310 (A) + N9317 (B), low-dose, bright-field, 60 000x, defocus -1.3 µm.
Vitrified solution of C8S3-aggregates and PEI @ 10^{-5} M.

The presence of globular PEI between the aggregates sometimes leads to network formation. This is shown in Figure 5-20 where linkages between aggregates by PEI are highlighted. These links of PEI span distances up to 100 nm between aggregates. Their appearance varies from solid-like (Figure 5-20A) to more branching and vague (Figure 5-20B). It is hard to distinguish if these links are formed by single PEI chains or if larger clusters of several chains are involved. Over all, the total volume fraction of PEI that is consumed by the blobs and bridges is hard to evaluate and was

therefore neglected for our estimate of covered aggregate length. The unordered kind of wrapping with irregular thickness and the tendency of PEI to form blobs even abroad from aggregates, is undesirable for further experiments where dye labelled PEs shall be used with the demand to have these labels at a distinct distance. Therefore, although the coating with PEI is successful, this polyelectrolyte will be excluded for further sophisticated experiments.

5.2.4 Wrapping with polyallylamine-hydrochloride (PAH)

Adding a prepared solution of PAH to freshly aggregated C8S3 results in qualitative changes in absorption spectroscopy that can be seen in the spectra below.

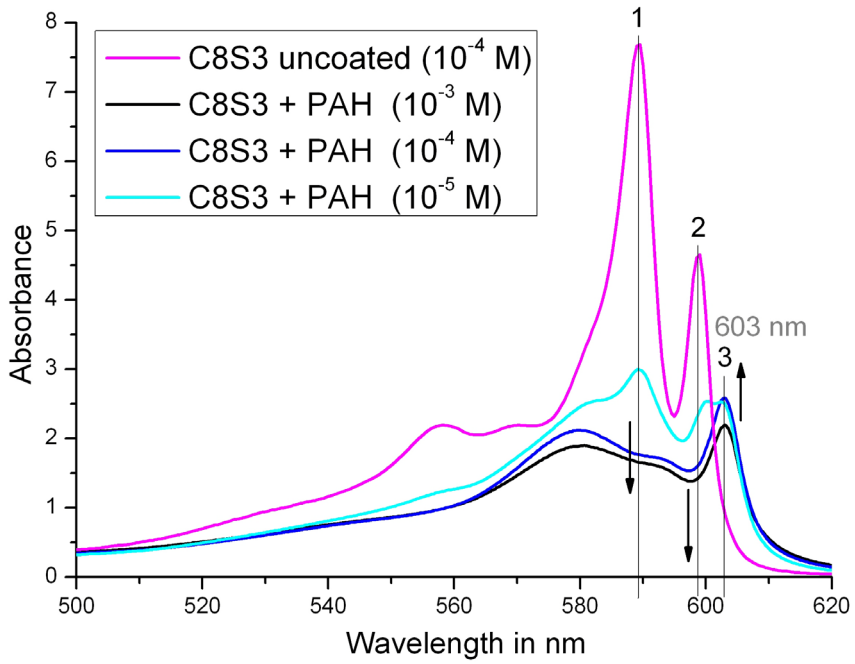

Figure 5-21:
Absorption of C8S3-aggregates and PAH treated aggregates. Changes in J-band are highlighted.

The spectroscopic investigation of C8S3 aggregates with various PAH-solutions delivers absorption spectra with interesting changes. First of all, one can state, that the characteristic J-bands are still present. For the highlighted position 1 in Figure 5-21, the peak decreases with higher PAH-concentrations. This takes place on peak-position 2 as well. On the other hand, there is a new peak increasing at position 3 when increasing the PAH concentration. These significant changes in spectra may be due to a structural changes within the tubes. A very similar spectroscopic behaviour

was observed earlier [131,132] and attributed to bundling of aggregates to larger agglomerates.

5.2.4.1 Structural appearance

As to be seen in the TEM images of PAH-treated aggregates, there are some aggregates with the known diameter **d** of 13 nm, which is known to be characteristic for uncoated aggregates, and a regular surface. These aggregates are identified to be uncoated.

The other aggregates in the images offering a larger diameter and rough and irregular surface, are identified as PAH-wrapped aggregates. The layer thickness of the coating varies.

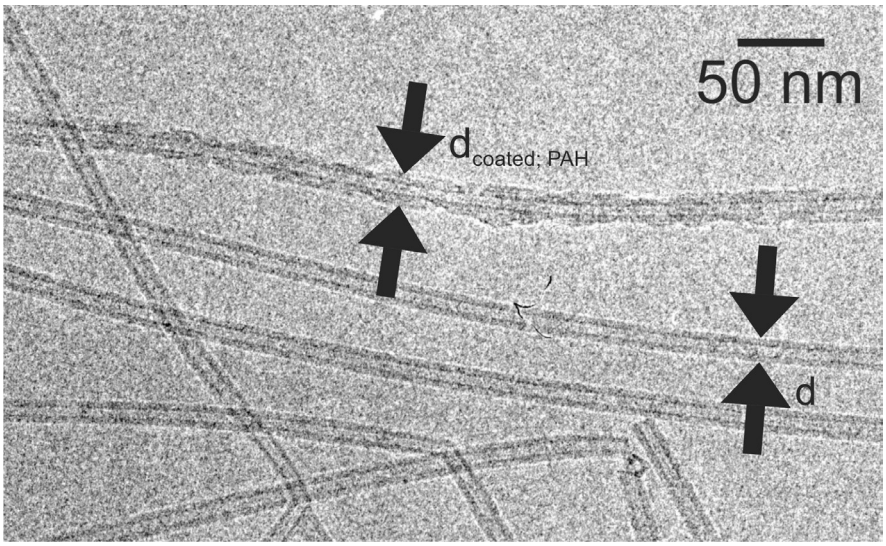

Figure 5-22:
Cryo-TEM image of vitrified solution of PAH-wrapped C8S3-aggregates, PE-concentration 10^{-4} M.
Image N6622 obtained at 60 000x, low-dose, bright-field, defocus -1.3 µm.

From the obtained TEM-images we derive the values for diameter of uncoated aggregates **d** and the average diameter of PAH-wrapped aggregates $\mathbf{d_{coated;\ PAH}}$

$$\mathbf{d} = 13 \text{ nm} \pm 1 \text{ nm}$$

$$\mathbf{d_{coated;\ PAH}} = 18 \text{ nm} \pm 1 \text{ nm}$$

Surprisingly the amount of PAH-electrolyte is not equally distributed on all aggregates. From screening a large number of TEM images one can state, that the wrapping of a single aggregate with PAH is entirely or does not take place at all. There are no aggregates with partly PAH-coating. Besides, only very few blobs, separated or attached, can be seen on these images.

Approximately 25% (of all tube length) of the visible aggregates in TEM images is covered with PAH, when applied with 10^{-4} M PE-concentration.

The estimation from eq. 5-1 ($\mathbf{V_{rel}} = 1.08$) for this case of 30% is very close to the measured coating-ratio. The mentioned blobs, although in very few in number, still consume PAH and have not been taken into account for the estimation. These blobs lower the coating-ratio which may explain the lower experimental coating-value.

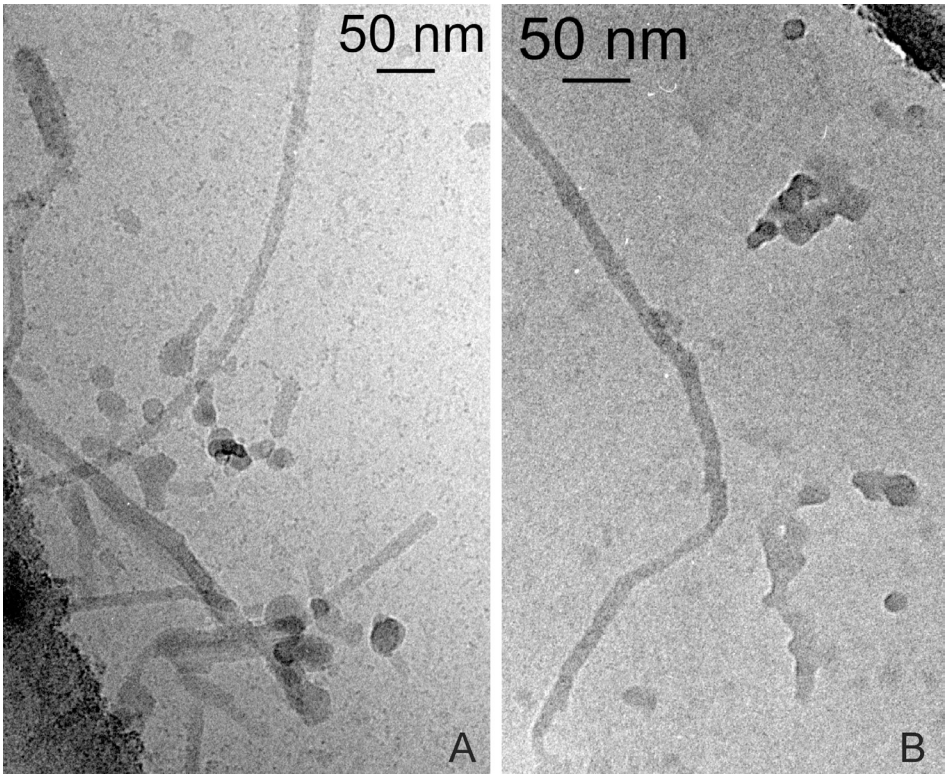

Figure 5-23:
Cryo-TEM images of vitrified solution of C8S3 aggregates wrapped with PAH (PAH concentration of 10^{-3} M).
Images obtained at 60 000x, low-dose, bright-field, defocus -1.3 µm.
A: I388
B: I391

In addition, it is worthwhile to consider wrapping of aggregates using PAH with higher concentration of 10^{-3} M (Figure 5-23). Such high concentrations were employed for the functionalization with dye labelled PAH. From the TEM-images one derives a higher coating-ratio of about 80%, while the coating-thickness is not changed.

5.2.4.2 Bundling of aggregates

Aggregates show a tendency to form bundles during aging over days or weeks. This tendency has been investigated and discussed in previous work [26,133]. In Figure 5-24 those bundles are presented as observed after 5 month of storage of an aggregate solution. Similar bundles where always found as rare by products in our samples even when freshly prepared, see Figure 5-10B. The distance **c** between individual aggregates in such bundles is reduced to zero and sometimes the aggregates are twisted around each other. The aggregates are not individual anymore.

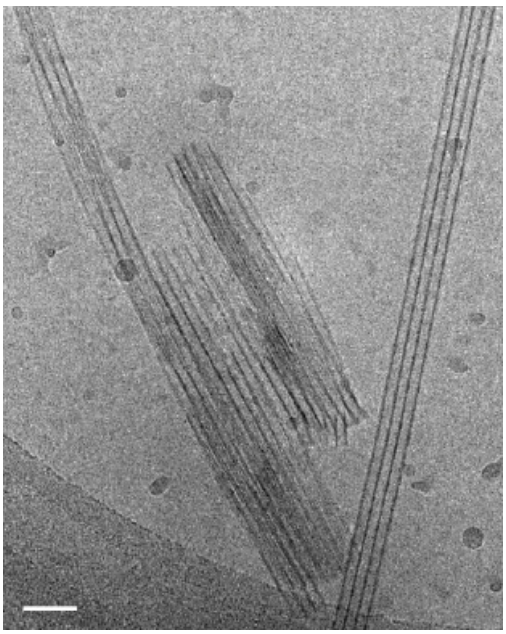

Figure 5-24:
Cryo-TEM image of C8S3-aggregates after 5 months of storage, showing bundles. Bar = 50 nm. (taken from [26]).

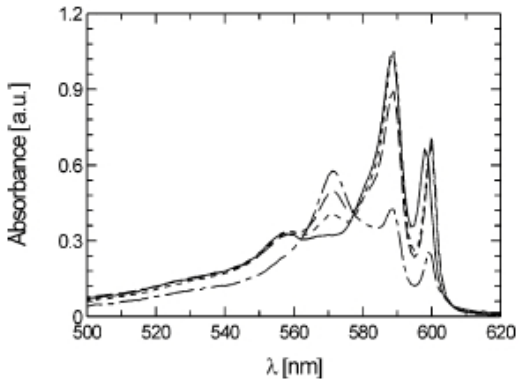

Figure 5-25:
Storage time dependence of the absorbance of C8S3 solution. Storage time after preparation: 10 min (solid), 1 day (dotted), 2 days (dashed), and 17 days(dotted-dashed) (taken from [26]).

The time-dependence of the absorbance has been investigated and is shown in Figure 5-25. In this detailed plot characteristic changes of the assigned J-band peaks are obvious. During the bundling progress the inner wall peak at 599 nm is replaced by a peak at 603 nm while the assigned outer-wall peak shows serious intensity loss.

It is assumed that initially the electrostatic repulsion of individual aggregates prevents them to form bundles. Over time there is some probability increases that two aggregates overcome the electrostatic repulsion barrier by thermal motion and are attracted by short range van-der-Waals-forces. For pure C8S3 samples this process takes days or weeks (see Figure 5-24 and Figure 5-25). For spherical colloids this process is well known as flocculation and described by the DLVO theory [134]. The attachment of several aggregates leads to larger bundles.

As known from the DLVO theory it should be possible to facilitate this bundling process by an increased number of counter-ions, because this decreases the Debye screening length and hence reduce the effective electrostatic repulsive force between individual aggregates. This effect was investigated by adding various salts to solutions of aggregates [135].

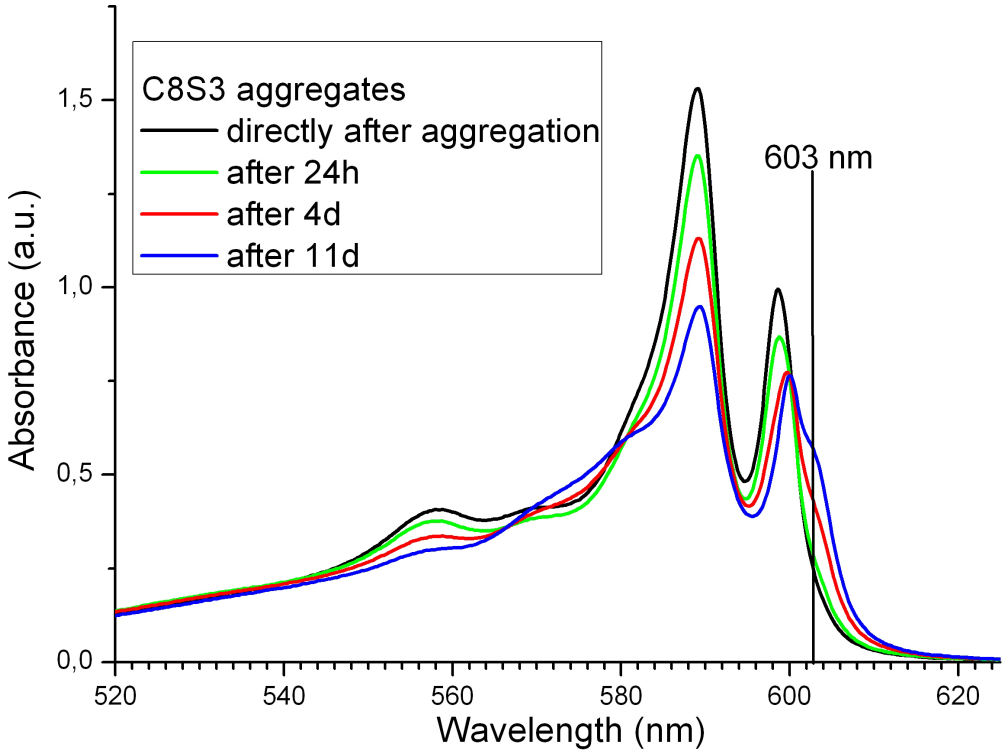

Figure 5-26:
C8S3 absorption-spectra obtained directly, 1d, 4d and 11d after aggregation, respectively. Assigned outer-wall peak decreases. Inner-wall peak shows formation of a new peak at 603 nm with time [135].

Spectral changes as shown in Figure 5-26 are assigned to formation of aggregate-bundles in solution. The dynamic of the bundling can be affected by addition of counter-ions.

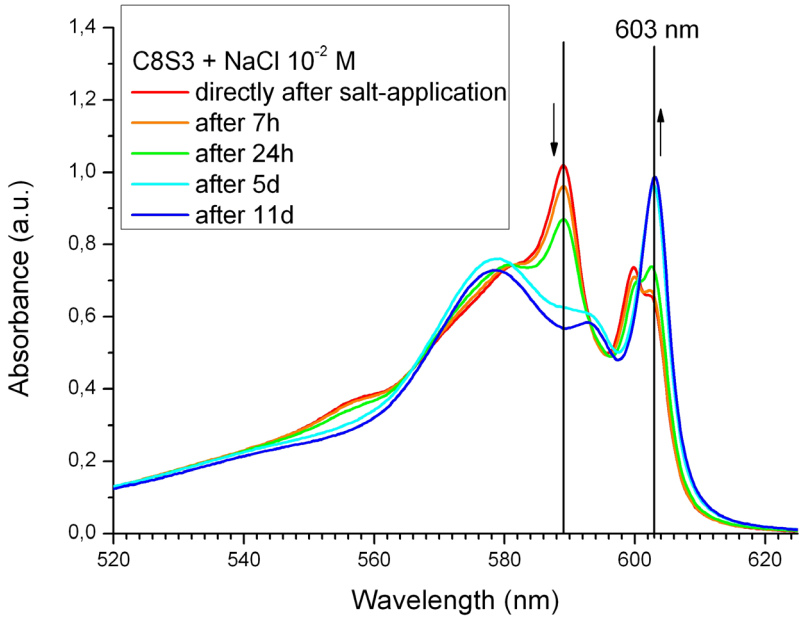

Figure 5-27:
Absorption-spectra of C8S3-aggregates with additional NaCl. The influence over time is depicted on the major J-band peaks. The outer-wall peak at 589 nm decreases, while the inner-wall peak, usually at 599 nm, shows a growing peak at 603 nm [135].

Figure 5-27 shows the influence of counter-ions on the bundling dynamic. The spectroscopic changes of NaCl-salt treated aggregate-solution reveal effects similar to bundling due to aging of aggregate-solution without salt. The difference is the speed of the dynamic. The addition of counter-ions obviously increases the speed of bundling dramatically. The intensity of the growing peak at 603 nm of pure C8S3-aggregates after 11 days of aging is comparable to C8S3-aggregates directly after addition of NaCl, so is the decrease of the outer-wall peak.

The treatment with counter-ions forces the solution to establish bundles much faster than obtained in aggregate-solutions without salt. The degree of bundling, obtained with the spectral-changes, is comparable with a 17-days-aging process without salt-addition. Additionally, the bundling reaches a new stable condition, where the spectra do not change anymore and probably all aggregates are attached to bundles. This increased bundling process due to addition of counter-ions is in accordance to the assumption of stabilization of sinlge aggregates by electrostatic repulsion.

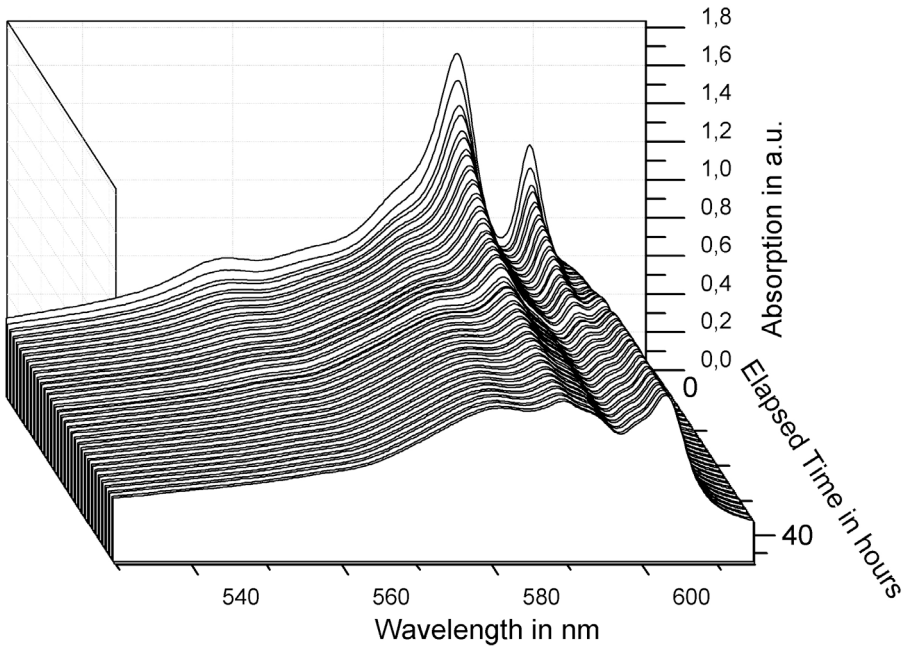

Figure 5-28:
2D-plot of PAH-wrapped aggregate (PAH-conc. 10^{-5} M) absorbance with addition of 0.1 M NaCl. The dynamic progress is shown from 0-48 h after adding salt to the aggregate solution.

Bundling was also observed for aggregates covered with PAH. The 2D-plot of Figure 5-28 shows the decrease of the outer-wall-peak while the new peak at 603 nm gains intensity. The inner-wall-peak at 590 nm is also decreasing. The spectra of a freshly prepared solution and measured after 48 h are given in Figure 5-29.

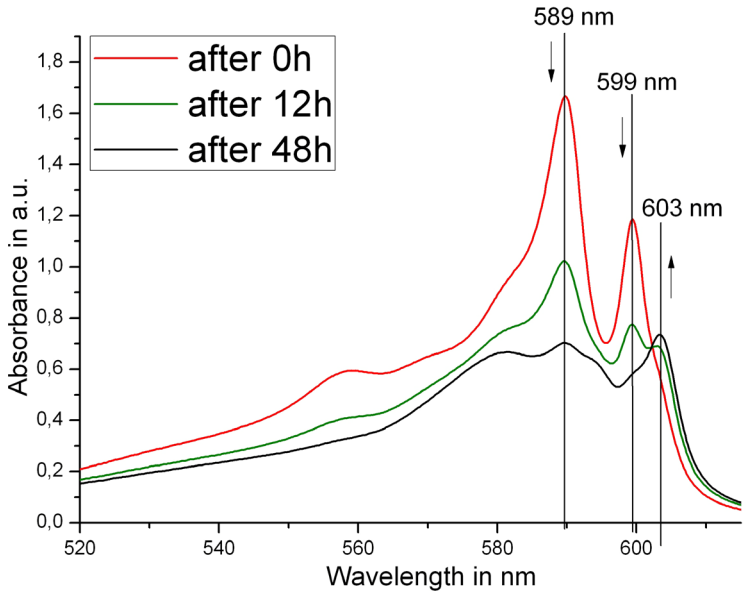

Figure 5-29:
Absorption of NaCl-treated (0.1 M) PAH wrapped aggregates immediately after salt-application, after 12 h, and after 48 h, respectively.

The dynamics of spectral changes PAH-wrapped aggregates under addition of salts is comparable to the dynamics observed for uncoated aggregates with NaCl. It is assumed, that the decrease of outer-wall peak and changes in inner-wall peak are due to same reason – bundling. This assumption is confirmed by inspection of cryo-TEM images, see Figure 5-30. A high number of bundles is found where the PAH coating can be identified by a blurred boundary of the bundles. The images also suggest that the bundles are glued into networks by the PAH.

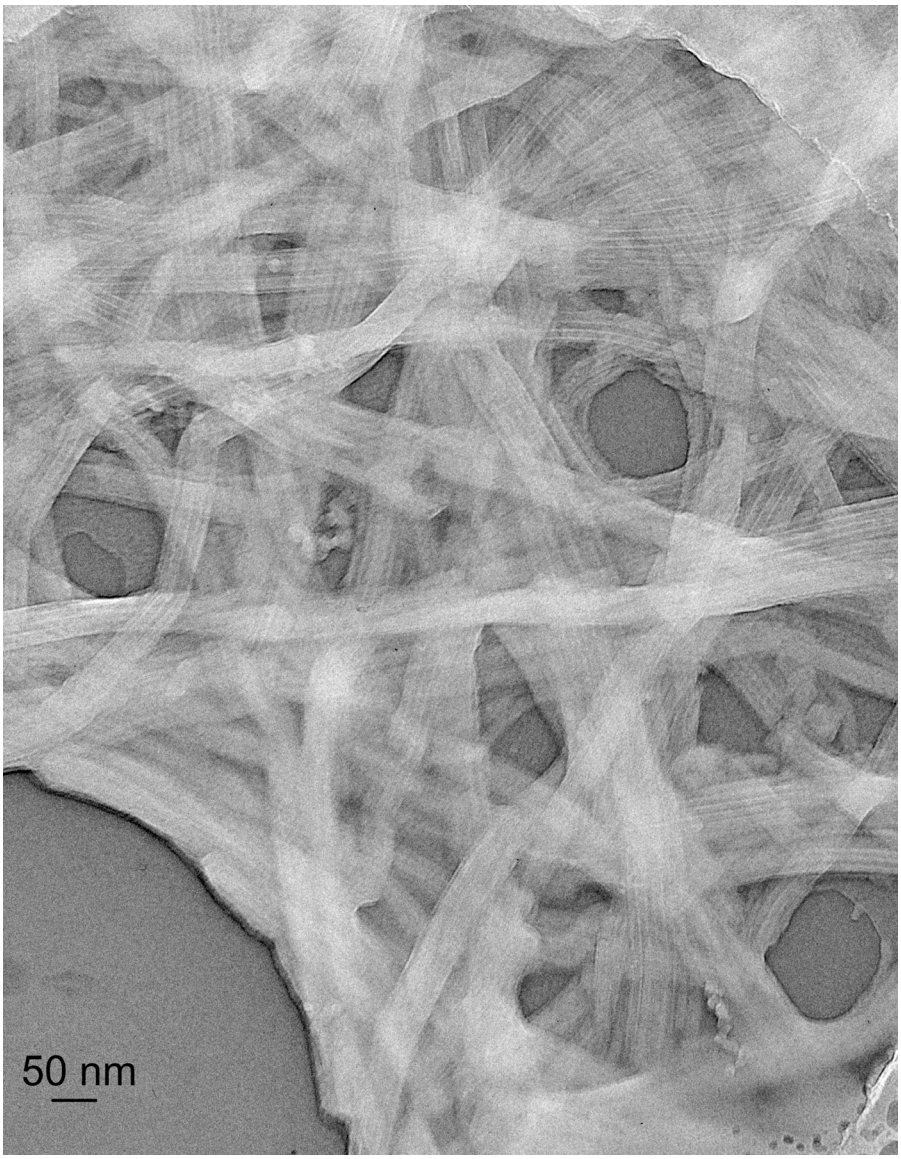

Figure 5-30:
Cryo-TEM image (H673) of wrapped C8S3-aggregates with NaCl (0.5 M), 2d after salt-addition to aggregate-solution. Almost all aggregates are found in bundles.

5.2.5 Zeta potential of wrapped aggregates

Adsorption of PE on aggregates can also be observed by monitoring the surface potential. Surface-charges of aggregates are negative if uncoated, which alters to positive charges, if coated. The surface charge causes response to external electric fields. Coated aggregates would be affected by external electric fields in the contrary way.

Zeta-potential measurements monitor this response. These measurements have been performed at the Free University, Department of Chemistry, in the group of Prof. R. Haag. The data were measured with a Malvern Zetasizer Nano ZS analyzer (Malvern Instruments Ltd, UK). Each measurement was repeated 3x20 times to avoid statistical anomalies. A Zeta-potential measurement obtains the mobility of charged particles in solution. The mobility is influenced by the viscosity of the medium and of course by the size and shape of the moving particles.

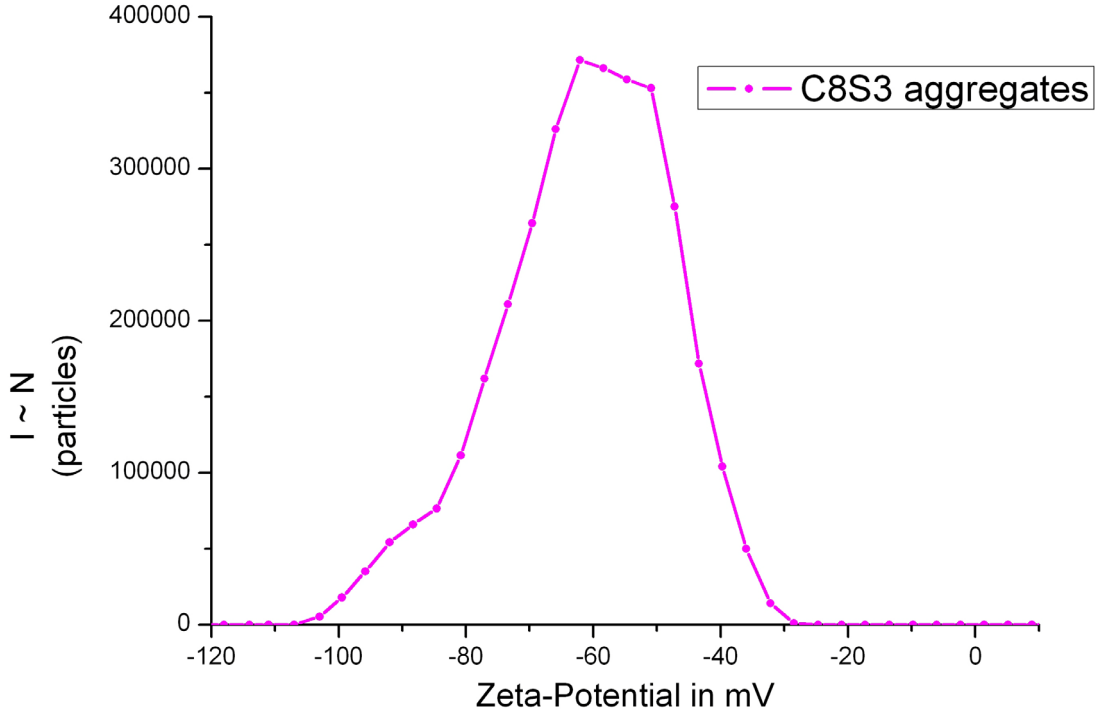

Figure 5-31:
Zeta-potential plot of naked C8S3-aggregates.

The plot in Figure 5-31 shows the intensity counts vs. zeta-potential of uncoated C8S3-aggregates. As estimated, the charged particles in the solution, the aggregates, offer a negative surface charge. Although the diameter of the aggregates has always been determined to be approximately 13 nm, the length may differ. So the

investigated solution offers an ensemble of aggregates in a variety of lengths, causing the zeta-plot to appear broadened.

Such measurements were done for every polyeletrolyte used for the wrapping. The following plots show the results of the Zeta-potential measurements.

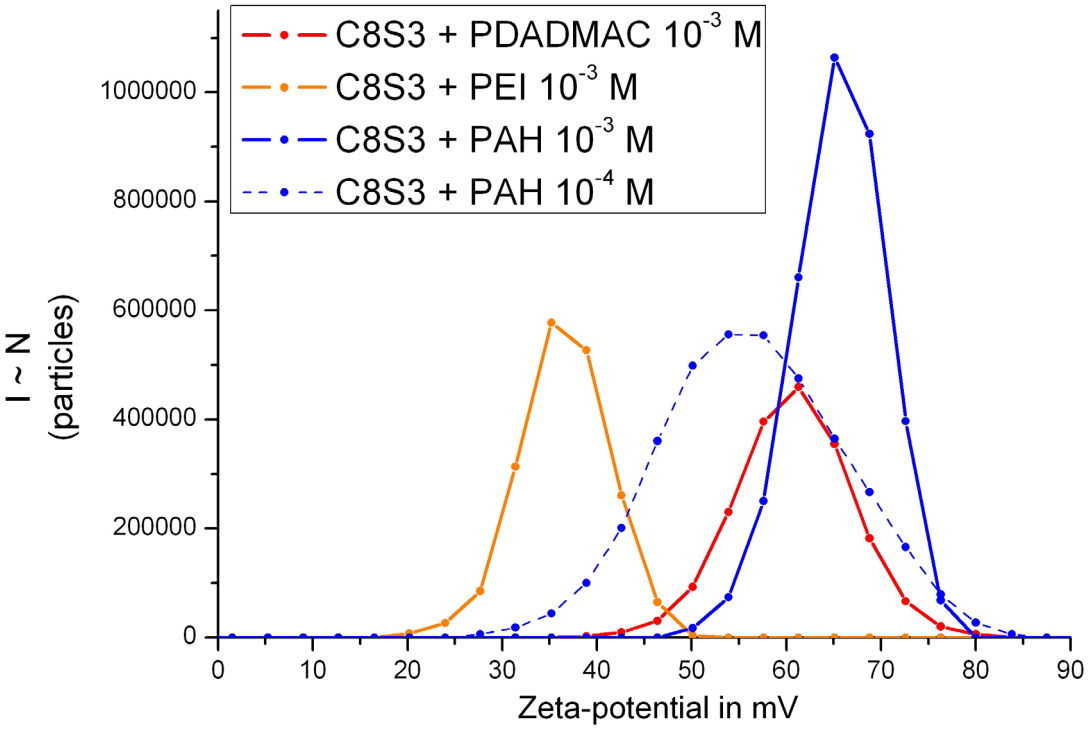

Figure 5-32:
Zeta-potential plot of wrapped C8S3-aggregates. Each colour represents coating with a certain polyelectrolyte. All polyelectrolyte treated C8S3-solutions provide positive potentials.

Obviously the wrapping of C8S3 with positively charged polyelectrolytes changes the surface charge of the aggregates dramatically, even towards opposite sign. Such behaviour is well known from colloids when coated by oppositely charged polyelectrolytes [136,137,138,139]. However, one has to note that colloids used for polyelectrolyte adsorption usually have much larger diameters, starting from 200 nm. Comparison of PAH-, PEI- and PDADMAC-wrappings at same concentration of 10^{-3} M reveals that the wrapping with PAH delivers the highest zeta-potentials. This might be due to the fact that PAH is providing the highest charge-density.

It is interesting to relate the change in surface potential with the amount of positive charges adsorbed upon wrapping with polyelectrolytes. As an example we consider PAH. Assuming a dense-packing of PAH in the coating layer, one can evaluate the number of PAH monomers as well as C8S3 dyes consumed per aggregate-length from simple volume considerations. The total wall of the aggregates consists of

approximately 100 molecules per nm length, where 2/3 belong to the outer wall. A more precise calculation gives 64 C8S3-monomers per nm for the outer wall, whereas the coating consumes 974 PAH-monomers on the same aggregate-length. From this evaluation one derives a ratio of 15:1 PAH-monomers in the coating per C8S3-monomer in the outer wall. This large over charging may easily explain the observed overcompensation of the surface-charge. Even if one assumes that each C8S3-monomer provides two negative charges at the surface (neglecting the positive charge at the conjugated polymer unit) the charge-ratio remains in the order of 7:1.

The mean surface potential as seen by the maximum of the potential distributions in Figure 5-32 shifts with the concentration of PAH. The higher PAH concentration (10^{-3} M, solid line) offers an average zeta potential of 66 mV, whereas the lower concentrated PAH (10^{-4} M, dashed line) offers 55 mV. The higher concentration shows a more narrow distribution with a maximum of intensity counts up to 120 000 counts and a potential spread of ±10 mV, whereas the lower concentrated PAH shows a more broad distribution with maximum of 60 000 counts and a spread of up to ±25 mV. The gain in mean zeta-potential indicates an increased number of attached positive charges on the aggregates for the higher concentration of PAH [136]. The smaller spread might be due to a higher homogeneity of wrapped aggregates at higher PAH concentrations, which is in good accordance to the observed TEM-images, showing a significant higher coating-ratio on the high-concentrated PAH coatings.

5.3 Functionalization of wrapped J-aggregates

The following section describes FRET experiments as a proof of concept for functionalization of wrapped J-aggregates. The function of energy transfer between the aggregate and dye-labels is enabled by labels located in the wrapping-layer. The functional dye-labels are covalently bound to the polyelectrolyte that is going to be wrapped around the aggregates. This method is favourable against direct incorporation of dyes into the J-aggregate for two reasons: first, the structural integrity of the aggregate is less disturbed; second, the location of the dye labels is known, because they are homogeneously distributed within the wrapping layer.

Two versions of energy transfer are investigated: Energy transfer from donor-labels to the aggregate and the other way round, energy-transfer from aggregate to dye-labels. Differences in transfer-efficiencies should reveal anomalies caused by excitonic effects, such as exciton-migration.

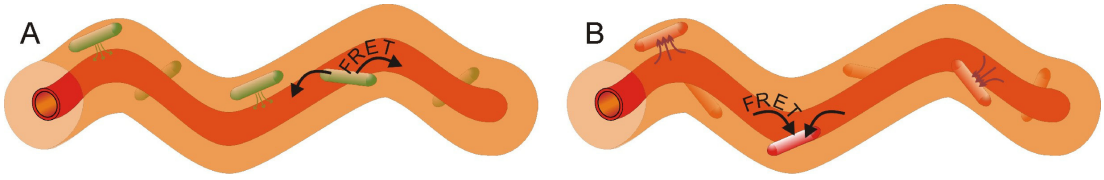

Figure 5-33:
Sketch of functionalized aggregate.
A: Donor-labels in the coating-layer deliver energy via FRET to the aggregate. (donor-to-aggregate FRET) B: Acceptor-labels receive energy from aggregate (aggregate-to-acceptor-FRET).

Figure 5-33 illustrates the investigated constellations. In the following the dyes rhodamin B and Alexa631 are investigated as approaches of donor-labels or acceptor-labels in the coating, respectively.

5.3.1 Donor-to-aggregate-FRET (rhodamin B as donor)

The first functionalization attempt was done with rhodamin B on PDADMAC. In this constellation, the rhodamin B dyes bound to PDADMAC are donors, while the aggregate is acting as energy-acceptor, as depicted in Figure 5-33A. In this configuration the quenching of donor emission is the relevant measure. Fortunately, this is independent of the wrapping ratio of the dye labelled PDADMAC.

5.3.1.1 Structure of rhodamin B PDADMAC functionalized aggregates

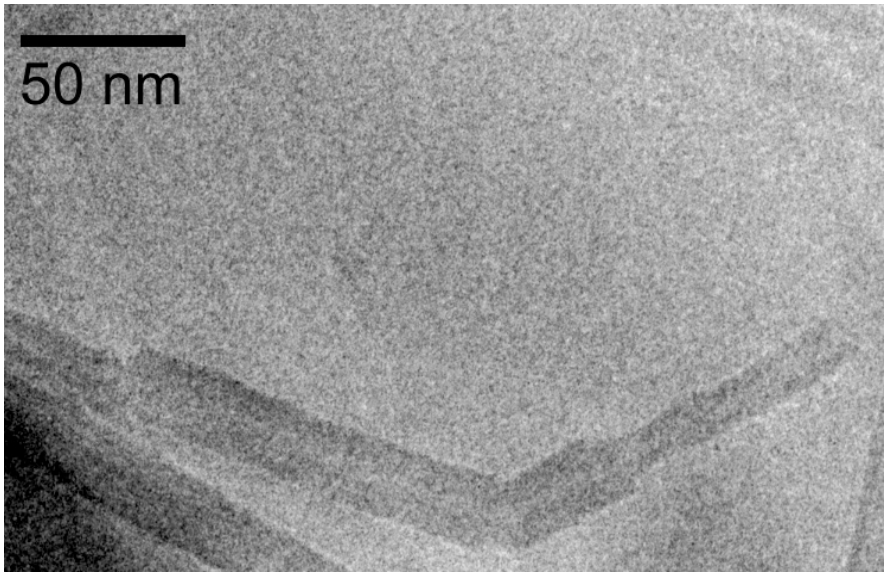

Figure 5-34:
Cryo-TEM-image (E382) of C8S3-aggregates with PDADMAC (10^{-5} M) labelled with rhodamin B.

In Figure 5-34 a typical TEM-image of rhodamin B functionalized C8S3-aggregates is shown. The image shows a PE-coating, which appears to be similar to the coating of plain PDADMAC application. The coating thickness is found to be 4 nm, as it was for non-functionalized PDADMAC-wrapping. Also, the low coating-ratio and overall smoothness of functionalized PDADMAC coating is similar to the case of non-functionalized PDADMAC. From this point of view, the morphology of plain wrapped aggregates and functionalized aggregates are supposed to be equal. The functionalization of the polyelectrolytes is assumed to have no impact on the quality or quantity of the coating.

5.3.1.2 Donor quenching

For an overview, the absorption- and fluorescence-spectra of the rhodamin B labelled PDADMAC and the C8S3 aggregates are given below.

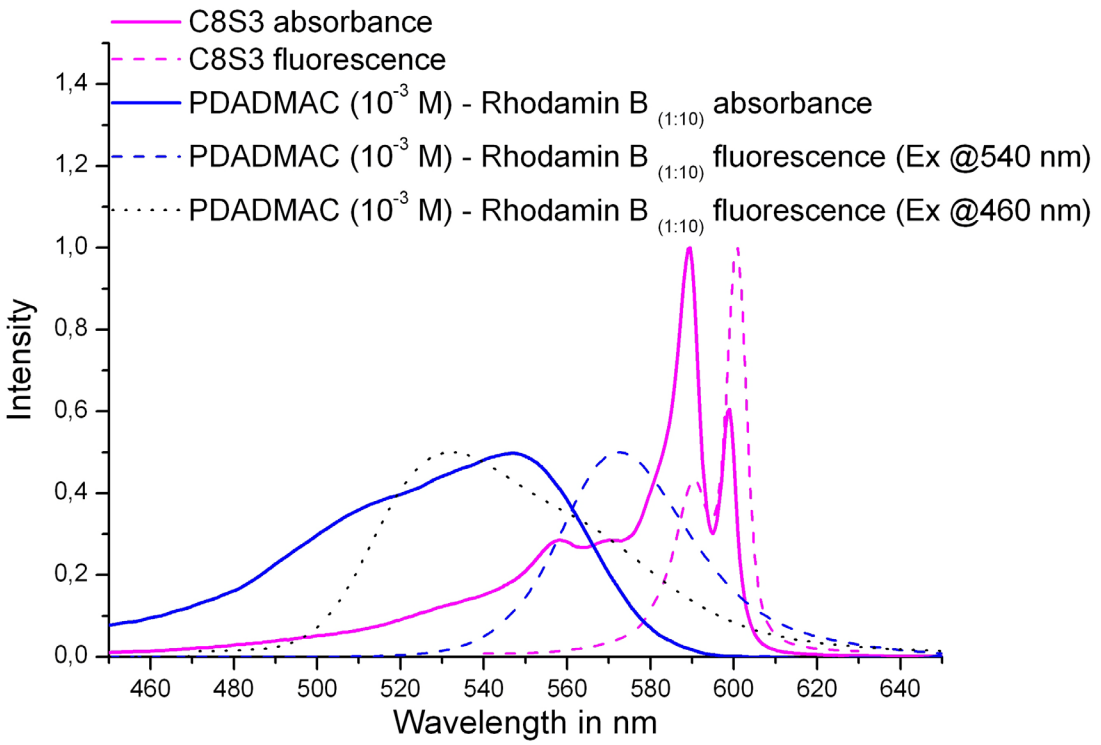

Figure 5-35:
Absorption and emission of uncoated C8S3 aggregates and rhodamin B labelled PDADMAC.

The comparison of absorption and emission of rhodamin B labels and C8S3-aggregates, see Figure 5-35, shows, that the emission of rhodamin B is overlapping with the absorption of the aggregate, which provides a high value for the overlap integral **J** and therefore grants a good transfer-efficiency. The evaluation of **J** is given in the appendix-chapter 7.2.1.

On the other hand, there is also large overlap between the absorption of rhodamin B and the absorption of the aggregates, which makes it impossible to excite the donor labels solely. There is always significant co-excitation of aggregates hampering the observation of enhanced fluorescence of aggregates due to energy transfer from the donor labels. Furthermore, the emission of rhodamin B is not only overlapping with the absorption of the aggregates, but also with the emission of the aggregates, leading to a mixing of the emission spectra.

Due to these spectral issues it is not possible to separately excite the rhodamin B donor and to analyse the aggregate acceptor-response, but one always has to consider a composition of donor- and aggregate emission. The best quantity to observe is the quenching of the donor-emission.

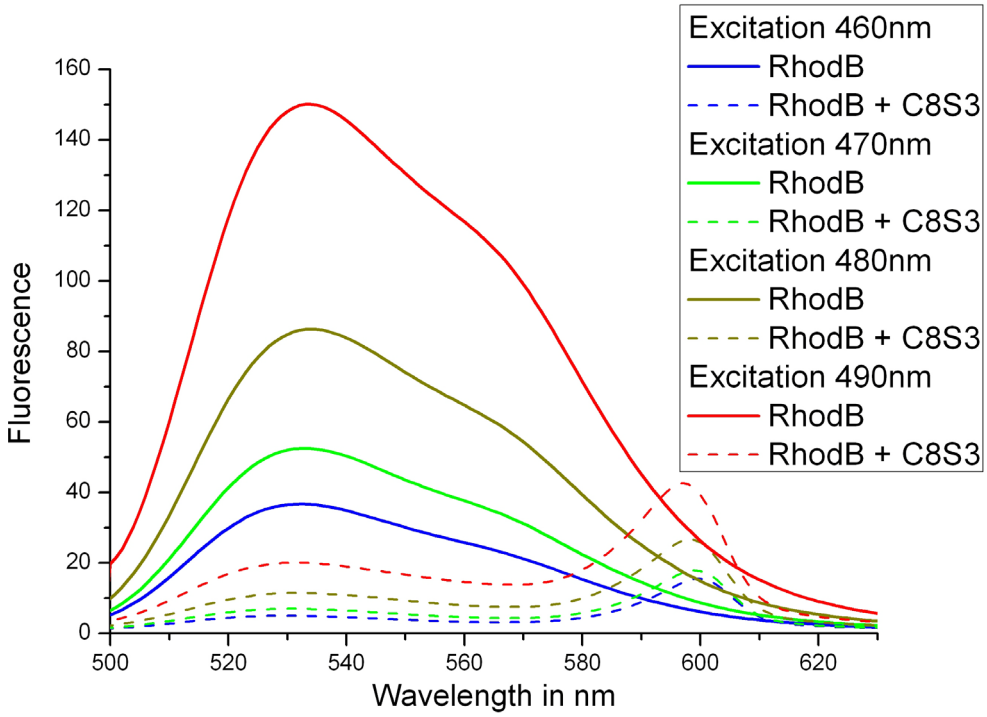

Figure 5-36:
Donor-fluorescence quenching: Fluorescence of rhodamin B labels on PDADMAC (without aggregate acceptor) compared with rhodamin B PDADMAC + C8S3-aggregates. Excitation wavelengths from 460 nm to 490 nm.

Figure 5-36 shows the fluorescence of rhodamin B labels on PDADMAC at various excitation wavelengths in solid-lines. The emission of pure rhodamin B PDADMAC and of aggregates wrapped with rhodamin B PDADMAC are shown in comparison. The dye-concentration was the same for both cases.

It is obvious that the fluorescence of rhodamin B is quenched when C8S3-aggregates are present. The rhodamin B-peak at 530 nm declines to 20% of the original emission intensity if the aggregate-acceptor is available. In absence of aggregates this peak is growing 4-times with a shift of the excitation from 460 to 490 nm. In presence of aggregate this growth factor is maintained, whereas the aggregate emission peak at 599 nm gains a factor of only 2.

The fluorescence decrease is due to effective quenching of the donor. The donor-labels are located in close proximity to the aggregate. The number of dye-labels, respectively the density of labels, has no impact on the quenching-efficiency. The quenching is only dependent on the distance to the acceptor molecules, which are present in the aggregate. The aggregate is in this case an omni-present acceptor.

The quenching of the donor due to the omni-present acceptor can be estimated by simple geometric considerations of label-density and –distribution in the aggregate-coating, depicted in Figure 5-37.

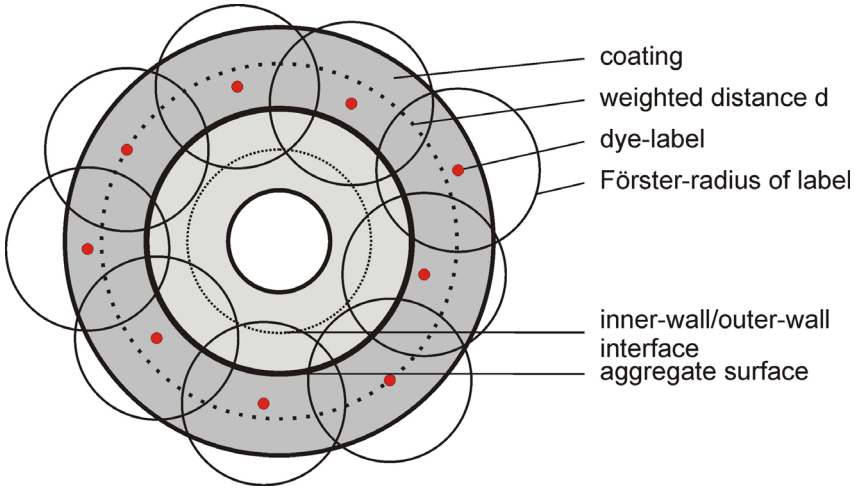

Figure 5-37:
Schematic view of coated aggregate in cross-section. Depicted dye-labels are shown with Förster-radius R_0. The averaged distance is drawn in dashed line within the coating. In the case of PDADMAC-coating with 10% label-ratio the number of dye-labels given equals a 1 nm segment.

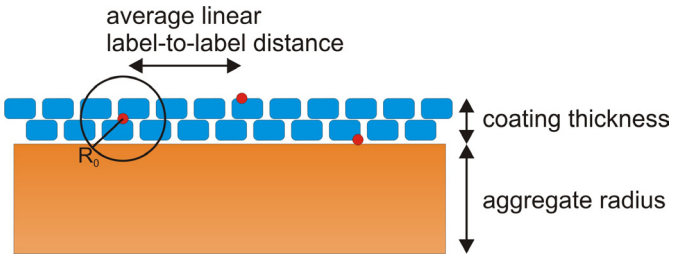

Figure 5-38:
Sketch of coated aggregate. Functional groups at various positions within the coating are depicted as red dots and a sphere with Förster radius R_0 are shown. The transfer efficiency is given by the cross section of this sphere with the surface of the aggregate.

The cryo-TEM images revealed for PDADMAC an average coating thickness of 4 nm. From the spectral overlap **J** of donor-emission and aggregate-absorption and with the assumption of statistical orientation of the molecules one derives a Förster-radius $\mathbf{R_0}$ of approximately 48 Å (± 7 Å) from eq. 2-36 (see appendix for more details). Namely, the Förster-radius is dependent on the spectral overlap **J**, the quantum yield $\mathbf{\Phi_D}$, the refractive index of the medium between donor and acceptor $\mathbf{n_D}$ and the geometry factor $\mathbf{\kappa^2}$.

$$R_0^6 \propto \frac{\Phi_D}{n^4} \kappa^2 \cdot J \qquad \text{(eq. 5-2)}$$

The geometry factor $\boldsymbol{\kappa^2}$ was taken for the case of static molecules with total random orientation, which is $\boldsymbol{\kappa^2} = 0.476$ [79]. The quantum efficiency of the donor $\boldsymbol{\Phi_D}$ and the refractive index of the environment $\mathbf{n_D}$ are less well known. Although the quantum efficiencies can be taken from literature values, the error may by rather high. Fortunately, due to the power of 1/6 the dependency on this quantity is weak. For that and because of technical reasons, $\boldsymbol{\Phi_D}$ was not measured directly.

The refractive index of the solvent, mostly water, is $\mathbf{n_D} = 1.33$. However, the donor molecules are embedded into a matrix of polyectrolyte and dye. The refractive index of polyelectrolyte multilayers as measured values are reported between 1.44 for layers swollen with water [140], 1.46 for sprayed films [141,142], and 1.55 for slightly different materials [143]. Additionally, the chromophores of the J-aggregate are within an environment that in total consists of π-electron systems. For that case, a dielectric constant of $\boldsymbol{\varepsilon} = 2.5$ was postulated [144] giving a refractive index of $\mathbf{n} = 1.58$. In conclusion, a reasonable value for the refractive index will be $\mathbf{n_D} = 1.5 \pm 0.1$.

From the label-ratio of 10% and the PDADMAC-monomer-volume one finds that approximately 83 dye-labels are located around the aggregate in the coating within a 1 nm long segment. Figure 5-37 reflects the high surface coverage with dye-labels. This sketch visualizes the conditions within the coated aggregate

In order to calculate the transfer-efficiency analytically, some simple assumptions are made. First of all, the distribution of dye-labels in the coating is assumed to be randomly but homogeneous. Second, the aggregate surface is assumed to be a flat 2-dimensional area. The latter is justified by the large radius of the aggregate compared to the distance of the donor-molecules, see also Figure 5-38.

For further analysis an average distance **<d>** is calculated with the condition, that the sum of **N** areas $\mathbf{A_i}$ underneath the dye labels is equal to **N** times the area of labels at the average distance, as indicated in Figure 5-39 and Figure 5-40.

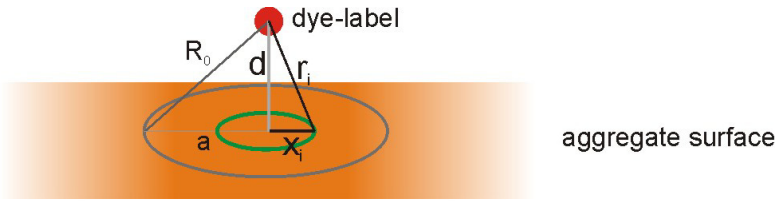

Figure 5-39:
Illustration of area underneath dye-label. The very center of the spot provides highest transfer-rates, the edge at distance R_0 from label enables 50% transfer-efficiency. The area A of this spot is given with the radius a.

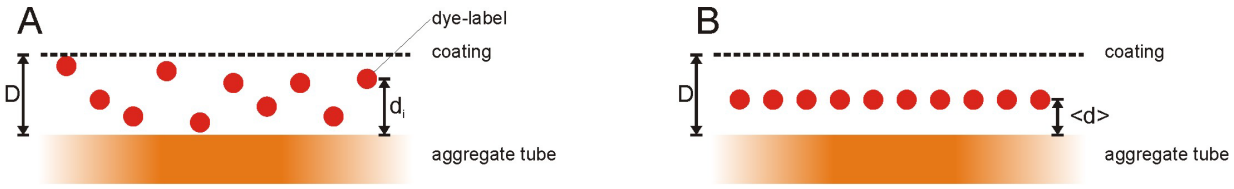

Figure 5-40:
Sketch of dye-labels distributed within the coating-layer of thickness **D**.
A) randomly distributed dye-labels at individual distances d_i.
B) dye-labels at averaged distance <d>.

For large number of donors the summation is replaced by integration and one finds for the average distance the condition.

$$A = \frac{1}{D}\int_0^D \pi r^2 dd = \frac{1}{D}\int_0^D \pi\left(R_0^2 - d^2\right)dd \qquad \text{(eq. 5-3)}$$

The sum of areas underneath has to be equal in both depicted cases Figure 5-40A and Figure 5-40B.

$$\frac{1}{D}\int_0^D \pi\left(R_0^2 - d^2\right)dd =: \frac{1}{D}\int_0^D \pi\left(R_0^2 - \langle d\rangle^2\right)dd \qquad \text{(eq. 5-4)}$$

One finds the relation for the weighted average distance **<d>** independent from $\mathbf{R_0}$.

$$\Leftrightarrow \frac{1}{\sqrt{3}} D = \langle d\rangle \qquad \text{(eq. 5-5)}$$

In the actual case of PDADMAC-coating with rhodamin B labels one derives from eq. 5-4 the value for **<d>** to be 2.31 nm. The circles of effective quenching on the aggregate surface have a radius of **a** = 3.27 nm.

The transfer-rates $\mathbf{k_{FT;planar}}$ from a donor-label to an acceptor-plane depends on distance **<d>** and the concentration of acceptor molecules $\mathbf{C_A}$ and is given by the following equation (taken from [145]):

$$k_{FT;planar} = \frac{\chi}{2} \cdot k_D \cdot C_A \cdot \pi \cdot R_0^2 \cdot \left(\frac{R_0}{\langle d \rangle} \right)^4 \qquad \text{(eq. 5-6)}$$

<d>: averaged distance between donor and acceptor

R_0 : Förster radius

k_D : luminescence-rate of donor in absence of acceptor

C_A : areal density of acceptors in plane underneath the donor

χ : correction factor for mutual polarization orientation of donor and acceptor

The fluorescence-rate $\mathbf{k_D}$ of rhodamin B can be derived from lifetime $\boldsymbol{\tau_D}$, taken from literature $\boldsymbol{\tau_{rhodamin\ B}}$ = 1,55 ns [146]. One finds the luminescence-rate $\mathbf{k_D}$ to be $\mathbf{k_D} = 6.45 \cdot 10^8\ s^{-1}$. The areal acceptor density $\mathbf{C_A}$ is given with the number of C8S3-monomers in the outer wall, which is assumed to be in the order of 0.15 nm^{-2}, which is in the range of typical literature values [147,148]. The correction factor $\boldsymbol{\chi}$ is assumed to be $\pi/4$, , which is the value for randomly distributed molecules within two planes [149]. With these numbers the transfer-rate is found to be

$$\mathbf{k_{FT;\ planar}} = (8.31 \pm 2.32) \cdot 10^{10}\ s^{-1}$$

The final transfer-efficiency $\boldsymbol{\eta_{FT;\ planar}}$ is derived from the relation of the Förster-rate $\mathbf{k_{FT;\ planar}}$ and the total rate **k** (taken from eq. 2-31).

$$\eta_{FT} = \frac{k_{FT}}{k_{FT} + k_{nr} + k_F} \qquad \text{(eq. 5-7)}$$

With

$$k_D = k_F + k_{nr} \qquad \text{(eq. 5-8)}$$

the relation for transfer-efficiency can be written as:

$$\eta_{FT} = \frac{1}{1 + \frac{k_D}{k_{FT}}} \qquad \text{(eq. 5-9)}$$

From equation 5-9 the total transfer-efficiency for rhodamin B labels to the aggregate surface is found to be

$$\eta_{FT;\ calculated} = (99.2 \pm 27.8)\ \%$$

From numerical consideration one derives a transfer-efficiency of 99.9%, see appendix, which agrees very well. This high transfer-efficiency is understood as a total quenching of the donor-dye-fluorescence, the rhodamin B labels. This calculated value of the transfer-efficiency η_{FT} is providing a very high tolerance, due to the dependence on the calculated Förster-radius $\mathbf{R_0}$, which is given itself with 14% tolerance. From this aspect, the calculated value for transfer-efficiency $\eta_{FT;\ calculated}$ includes the obtained value $\eta_{FT;\ obtained}$, from steady-state spectroscopy, shown in Figure 5-36, within the given tolerance.

5.3.1.3 Fluorescence-excess of acceptor

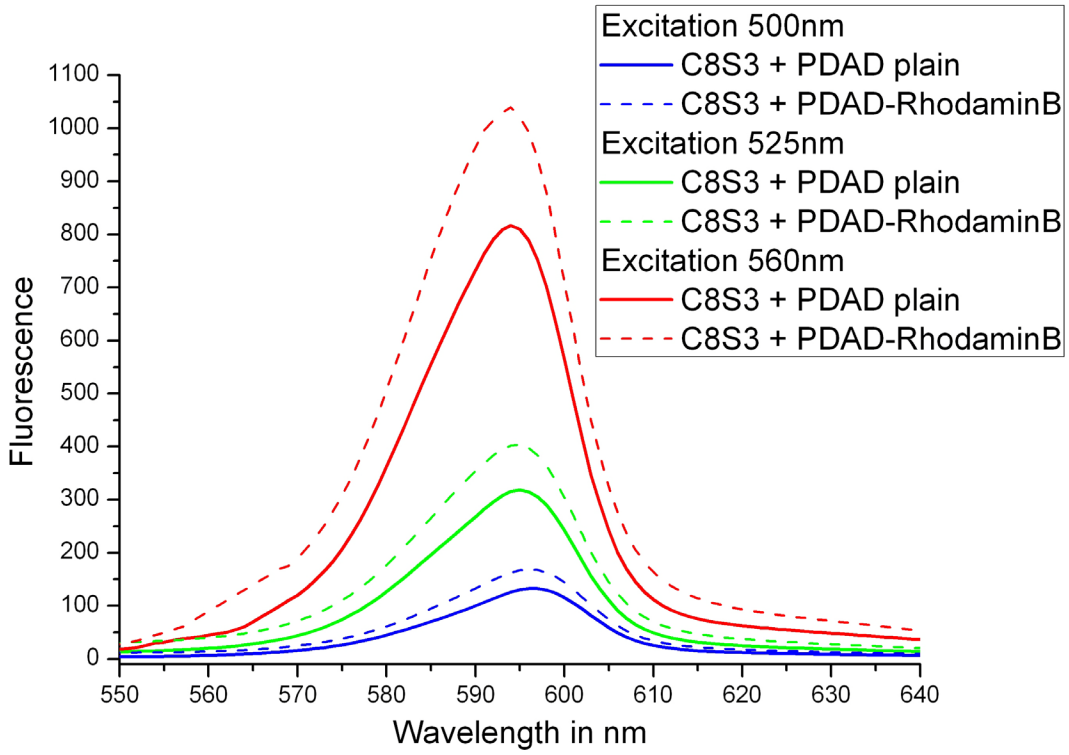

Figure 5-41:
Fluorescence-spectra of plain coated aggregates in comparison to functionalized aggregates. Both coatings made of PDADMAC.

The contribution of donor-dyes to the acceptor-fluorescence is revealed in comparison of fluorescence of plain-coated aggregates and functionalized aggregates. Both kinds of aggregates are coated with PDADMAC. Strain- and stress-

effects due to wrapping with polyelectrolyte occur in both species. Therefore, differences in fluorescence are solely due to the presence of donor-labels in the coating of the functionalized aggregates. These differences are plotted for three different excitation-wavelengths in Figure 5-41.

The direct comparison of both coatings, labelled and plain, reveals the fluorescence excess if labelled with donor-dyes. The excess is dependent on the excitation-wavelength.

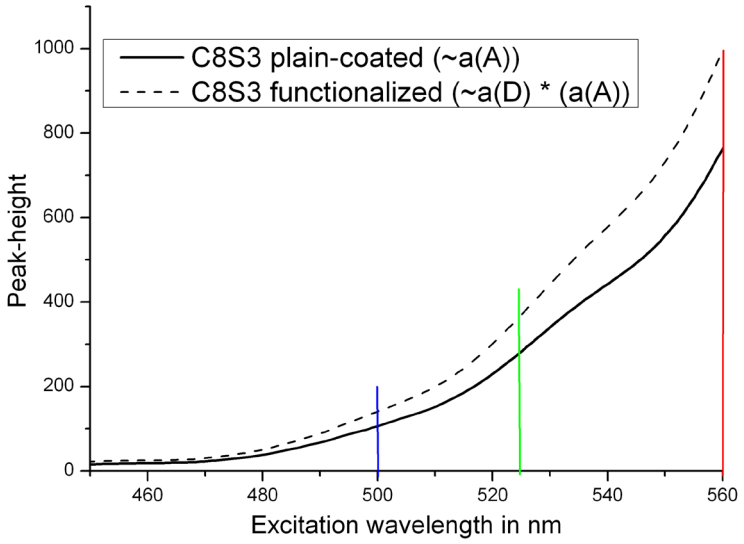

Figure 5-42:
Fluorescence-excitation-spectra of plain and functionalized C8S3-aggregates obtained at 591 nm emission. Compared are peak-heights of PDADMAC-coated aggregates with plain-coating (solid-line) and rhodamin B functionalized coating (dashed). Highlighted are the excitation-wavelength that have been shown in Figure 5-41.

The fluorescence-excess is recorded from the intensity at the major aggregate emission-peak, located at 591 nm. The emission peak-heights are plotted as a function of excitation-wavelength in Figure 5-42. This plot reveals the dependence on the excitation-wavelength.

The fluorescence-excess, though weak, is still observable. The weakness of the acceptor-response in contrast to the high expected transfer-efficiency is due to the weak absorber-strength of rhodamin B compared to C8S3. The contribution of excitation via rhodamin absorption is simply very week compared to the direct excitation of the aggregates. A non-normalized plot of rhodamin B and C8S3-absorbance shows the absorption-strength.

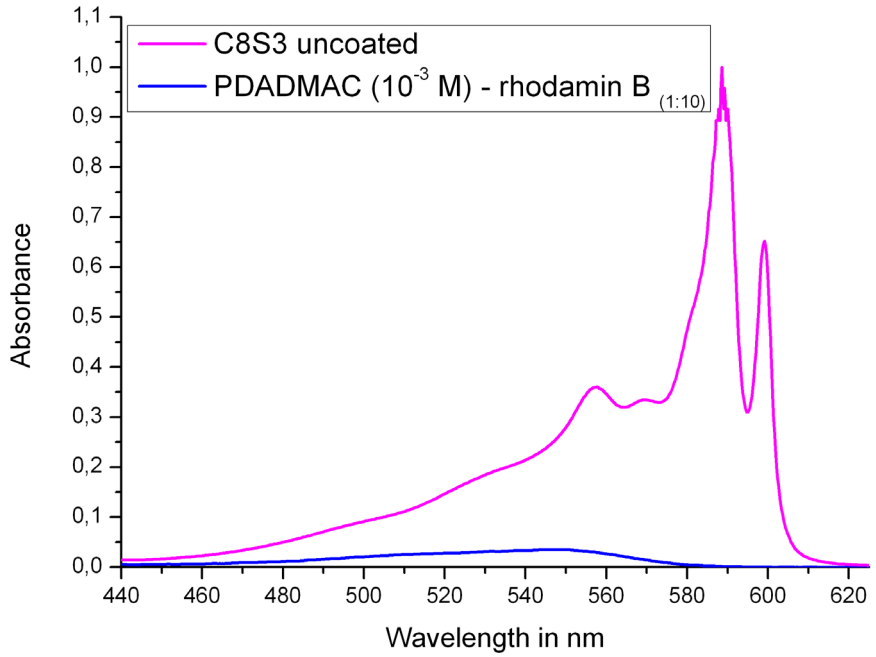

Figure 5-43:
Absorption spectra of uncoated C8S3-aggregates and rhodamin B as labels on PDADMAC. The 10% label-ratio of PDADMAC with rhodamin B causes a dye-concentration of 10^{-4} M.

Figure 5-43 shows the weak absorption of rhodamin B labels in comparison to C8S3-aggregates. Both, C8S3 monomers and dye-labels are shown in the same concentration-magnitude of 10^{-4} M, due to the label-ratio of 10% of the investigated 10^{-3} M PDADMAC-solution.

5.3.2 Aggregate-to-acceptor-FRET (Alexa631 as acceptor)

Energy transfer from the aggregate to an acceptor molecule was probed using PAH labelled with Alexa631 wrapping on C8S3-aggregates, as depicted in Figure 5-33B. In this constellation, the J-aggregates are donors, while the Alexa631 is acting as energy-acceptor. In this configuration the quenching of aggregate emission is probed as well as the emission of the Alexa-dye excited via energy transfer.

5.3.2.1 Structure of functionalized wrapping

Figure 5-44:
Typical TEM image of Alexa631-functionalized C8S3 aggregates in solidified solution. Wrapping with PAH (10^{-3} M). Cryo-TEM negative I376, 60 000x, defocus -1.3 µm, low-dose, bright-field.

The image in Figure 5-44 shows a typical TEM-image of Alexa631 functionalized aggregates. The appearance of the coating is similar to coating with plain PAH. The morphology of the underlying aggregates seems to be maintained. No significant changes to plain-wrapped aggregates with PAH coating are observable.

5.3.2.2 Fluorescence excess of acceptor (Alexa631)

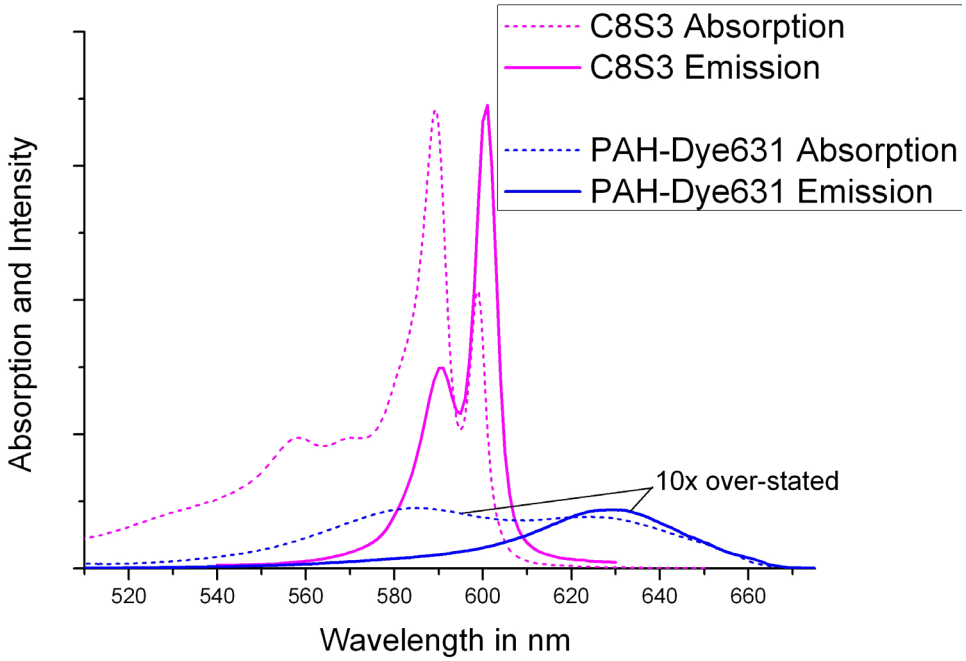

Figure 5-45:
Absorption and emission of Alexa631-labelled PAH and C8S3-aggregates. The graphs are pairwise normalized. For a better overview, the graphs of PAH-Alexa631 are 10-times magnified.

The spectra above show the absorption and emission of uncoated C8S3-aggregates and Alexa631-labelled PAH. In this figure one can clearly see the overlap of the aggregate emission with the dye-label-absorption. In this combination the aggregate is working as a donor, while the dye-labels are acceptors.

In this section we first investigate the emission of the dye label excited by energy transfer from the aggregate. Therefore, one has to be aware that the signal-strength of the dye-labels is very weak compared to the aggregates-signal. In Figure 5-45 the emission and absorption of the dye are not in scale but magnified for better view. Energetically, the dye-label emission-peak is separated from the emission-band of the aggregates. The challenge in signal separation is in this case not given by the peak-proximity of donor and acceptor, but by the weak signal-strength of the low concentrated dye-label. The Alexa631 has been labelled to the PAH wrapping with a label-ratio of 1%. This means, that on application of PAH at 10^{-4} M, which is the order of the C8S3 monomer-concentration, the concentration of dye-labels is 100-times lower than the concentration of C8S3 molecules in the aggregates.

Another challenge in spectroscopic investigation of this donor-acceptor-combination is the wide peak-broadening of the dye-label. The absorption of the dye labels begins

at 500 nm, although the absorption peak is located at 580 nm. This is overlapping with the aggregate absorption. Hence, excitation of aggregates is always connected with direct excitation of acceptor Alexa631. The Alexa631 fluorescence is not found directly, but indirect by revealing the difference in fluorescence signal-strength of plain-wrapped and functionalized aggregates.

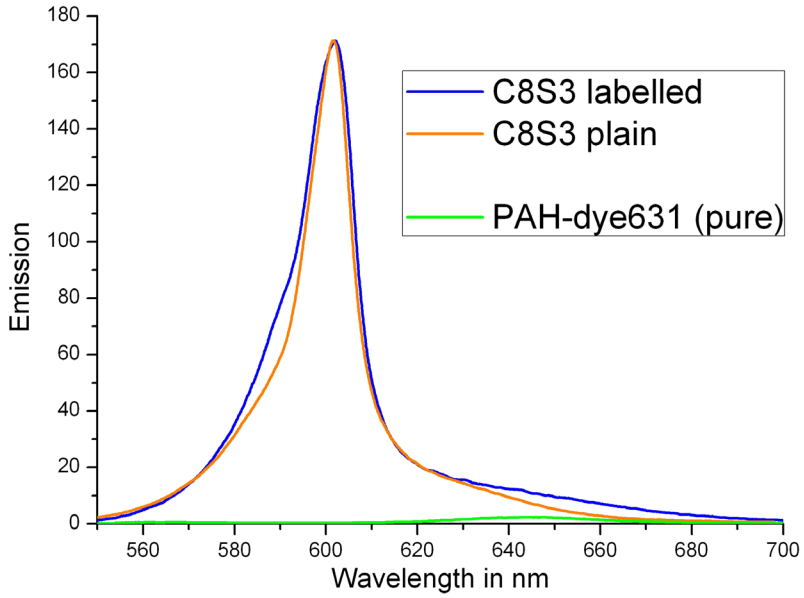

Figure 5-46:
Emission of plain C8S3 aggregates, Alexa631-labelled PAH (10^{-3} M) and C8S3 together with Alexa631-labelled PAH. Excitation @ 540 nm. The graph of pure C8S3 was normalized to the value of C8S3 with PAH-Alexa631.

Figure 5-46 shows the fluorescence from excitation at 540 nm. The green line is the emission of pure PAH-Alexa631, which shows the response from direct excitation. This response, from 610 nm up to 680 nm, is very weak compared to the aggregate signal. In comparison to this there are the plots of plain wrapped (only PAH without labels) and Alexa631-functionalized aggregates obtained under same conditions. To ease the comparability the graph of functionalized aggregates is normalized to equal peak-height of plain aggregates. Obviously, the typical appearance of J-band emission is still present. The characteristic double-peaks of the aggregates' J-band is not separable under these conditions.

Interestingly, the two graphs of wrapped aggregates differ, although the coating is in both cases PAH of same concentration. The difference reveals a small fluorescence excess of functionalized aggregates in the same wavelength-region as the response of pure PAH-Alexa631 appears. This part of the spectrum is analyzed in more details in Figure 5-47.

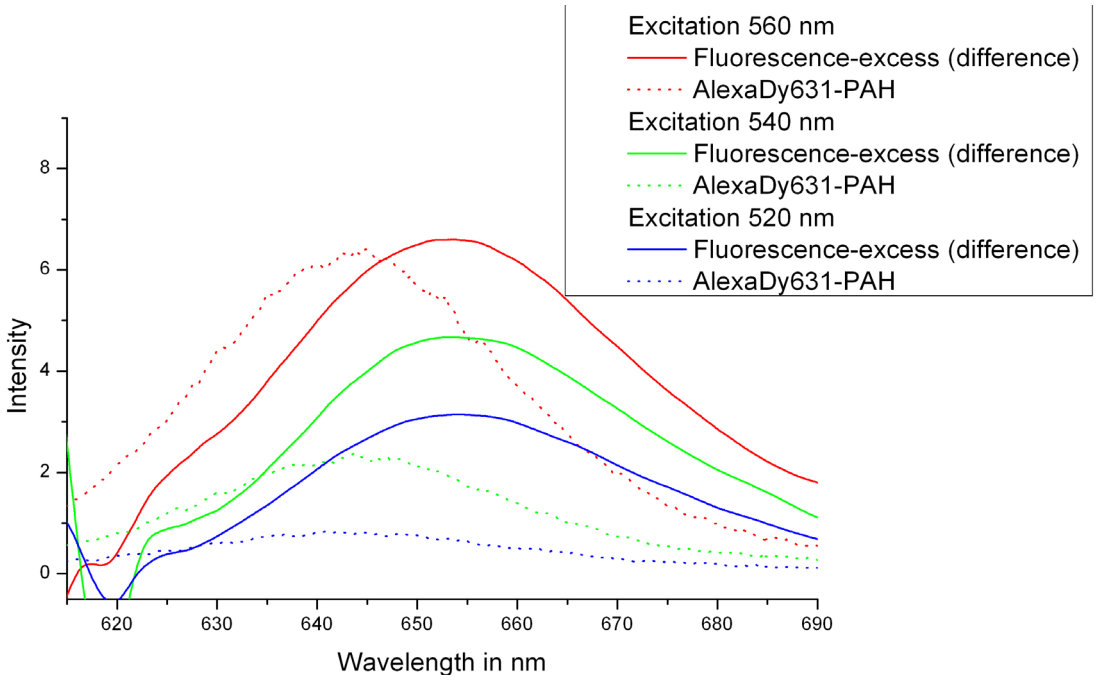

Figure 5-47:
Emissionspectra of pure Alexa631-labelled PAH (direct excitation) in comparison to fluorescence-excess revealed from difference of plain and functionalized C8S3-aggregates. Color-pairs are assigned to excitation wavelengths of 520, 540 and 560 nm.

The plots in the Figure 5-47 compare the direct excitation response of the dye labels, without aggregates (dashed lines), with the fluorescence excess of functionalized aggregates (solid lines). The fluorescence excess is calculated from the difference between spectra of aggregates wrapped with acceptor and aggregates wrapped with pure PAH as shown in Figure 5-46. Shown are comparisons at three different excitation wavelengths (520 nm, 540 nm, 560 nm).

The fluorescence-excess-plot shows a significant gain of intensity compared to the direct excitation of Alexa631. The excess-gain correlates with the absorbance of the C8S3 aggregates in the range of the excitation wavelength selected.

The absorption-spectra in Figure 5-48 show the respective absorbances in the highlighted range from 520-560 nm. The intensity of acceptor emission follows merely the absorbance of the aggregates for excitation at 520 nm and 540 nm. A high emission amplification by energy transfer is observed in Figure 5-47. The intensity for excitation at 560 nm has more contributions from direct excitation of the acceptor. Therefore, the amplification by energy transfer is only very week at this excitation wavelength.

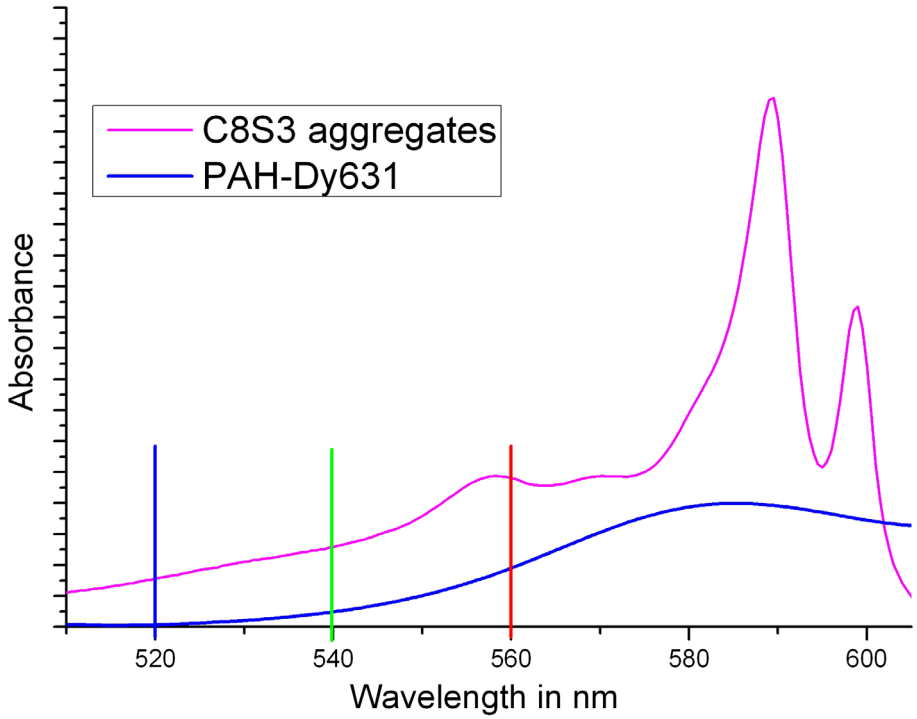

Figure 5-48:
Absorption of pure Alexa631-labelled PAH in comparison to naked C8S3-aggregates. The depicted excitation wavelengths from Figure 5-46 are highlighted.

Obtained fluorescence of Alexa631-labels can result from direct excitation and from energy-transfer, too. Determination of the energy-origin is achieved indirectly by considering the gain-rate with shifting excitation wavelength as depicted in Figure 5-48 .

5.3.2.3 Donor quenching

Since the fluorescence excess of the acceptor is hard to see, one considers the donor quenching to reveal the energy-transfer from aggregate to acceptor. Therefore the aggregate fluorescence is compared for plain-wrapped aggregates and Alexa631-labelled aggregates, see Figure 5-49.

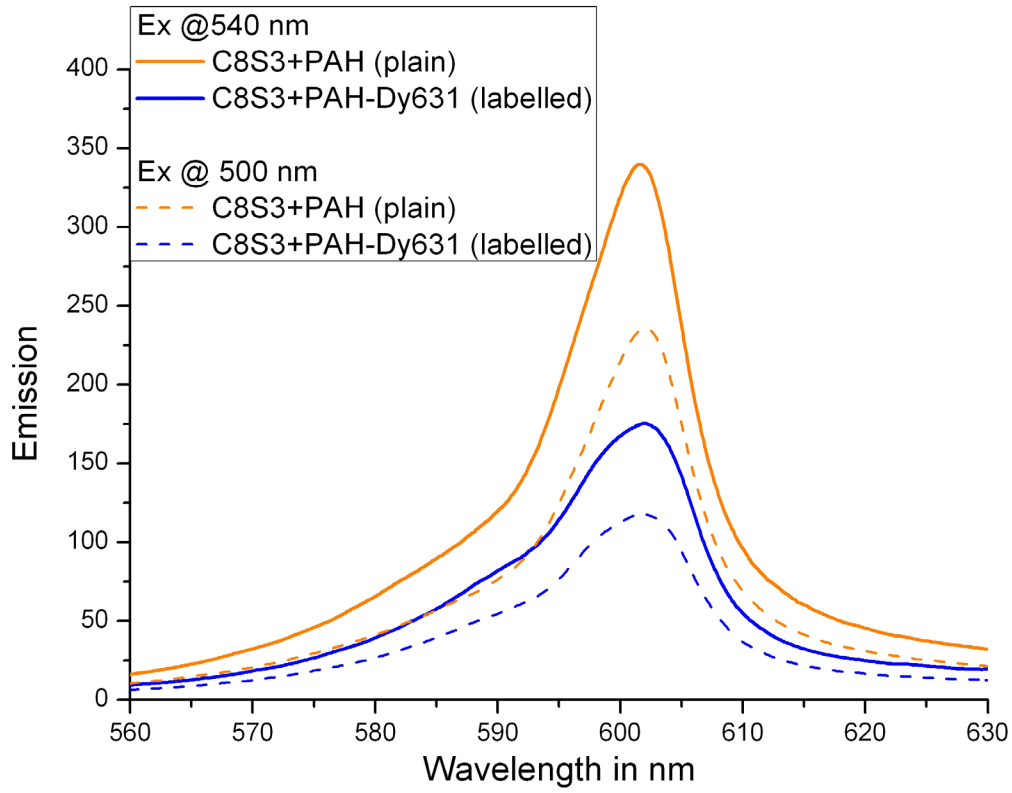

Figure 5-49:
Emission spectra of plain- and functionalized aggregates with PAH concentration of 10^{-3} M.

The loss of aggregate-fluorescence due to functionalization is significant, see Figure 5-49. The emission spectra of C8S3 are shown for plain wrapped (PAH) aggregates and functionalized (PAH-Alexa631) aggregates. The only difference is the presence of a FRET-acceptor-label in the coating. From comparison of the fluorescence-intensity of labelled- and plain-wrapped aggregates one derives the quenching-efficiency out of eq. 2-30, eq. 2-33 and eq. 2-34.

In this case the transfer-efficiency is found to be:

$$\eta_{FT} = 1 - \frac{I_{D+A}}{I_D} \qquad \text{(eq. 5-10)}$$

The maximum intensities are found at 540 nm excitation to be $\mathbf{I_{plain}} = 339\ (\pm\ 1)$, $\mathbf{I_{functionalized}} = 175\ (\pm\ 1)$. Hence, that the latter intensities are obtained from an

ensemble of functionalized, quenched, aggregates and uncoated aggregates. From prior cryo-TEM investigation it is already known, that even with the high-concentrated PE of 10^{-3} M, not all aggregates have been wrapped. The found coating-ratio had been determined to be 80%. Thus, the quenching revealed in steady-state spectroscopy appears weaker than it actually is, as 20% of the present aggregates remain uncoated and therefore contribute to the fluorescence unquenched. From this aspect, the orange-lines in Figure 5-49 are superpositions of fluorescence contributions from uncoated aggregates (20%) and functionalized aggregates (80%). To find the proper intensity $\mathbf{I_{D+A}}$ of donor in presence of an acceptor it is necessary to consider these coating-ratios. One may assign:

$$I_{functionalized} = 0{,}2 I_D + 0{,}8 I_{D+A}$$

$$\Leftrightarrow I_{D+A} = \frac{I_{functionalized} - 0{,}2 I_D}{0{,}8} \qquad \text{(eq. 5-11)}$$

The fluorescence of plain coated aggregates $\mathbf{I_{plain}}$ is assumed to provide the intensity of the donor in absence of an acceptor $\mathbf{I_D}$. One finds

$$\mathbf{I_{plain}} = \mathbf{I_D} = 339\ (\pm 1)$$

$$\mathbf{I_{D+A}} = 137\ (\pm 1)$$

With these values and eq. 5-10 one finds the transfer-efficiency obtained from steady-state spectroscopy to be

$$\boldsymbol{\eta}_{\mathbf{FT;\ steady}} = (59.6 \pm 0.5)\ \%$$

5.3.2.4 Energy decay of donor (aggregate)

A FRET is effecting the lifetime of the donor $\boldsymbol{\tau}_{\mathbf{D}}$, as to be seen in eq. 2-32 and 2-33. The investigation of the lifetime is performed with time-resolved spectroscopy. In the composition C8S3+PAH-Alexa631, the aggregate is meant to be an energy donor, while the Alexa631-labels act as acceptors. The time-resolved measurements, proceeded in the lab of Prof. Henneberger, are stated below.

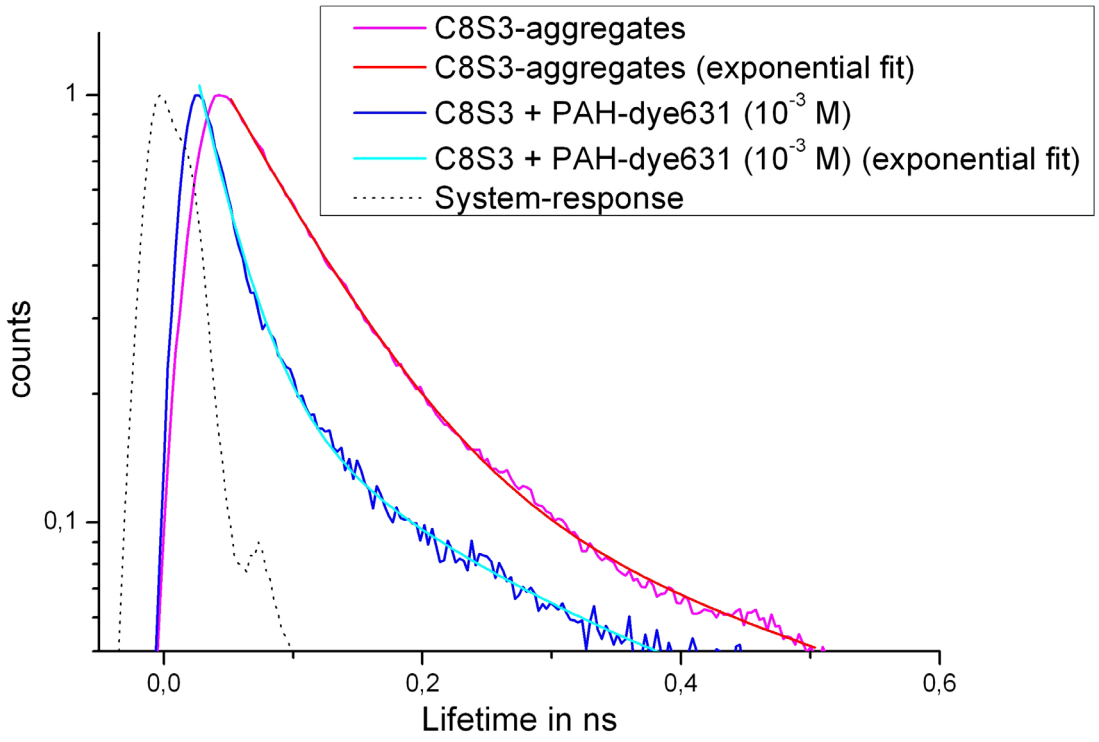

Figure 5-50:
Time-resolved spectroscopy of C8S3-aggregates and Alexa631-functionalized aggregates, obtained at 600 nm, 180s

Figure 5-50 shows the decay of excited states in the depicted solutions of C8S3-aggregates (magenta) and Alexa631-functionalized aggregates (blue). The logarithmic-plot reveals that the decay is not following a mono-exponential equation. The plots are therefore fitted with a function of type

$$f(t) = A_1 \cdot e^{-\frac{t}{\tau_1}} + A_2 \cdot e^{-\frac{t}{\tau_2}} \qquad \text{(eq. 5-12)}$$

The lifetimes τ is derived from the major decay-functions of these exponential fits ($\tau = \tau_1$ for **A1** > **A2**). The lifetimes of the donor and the donor in presence of an acceptor are found to be:

$\tau_{donor} = \tau_{C8S3} = 0.073$ ns ($\pm$ 0.005 ns)

$\tau_{donor+acceptor} = \tau_{C8S3+Alexa631} = 0.028$ ns ($\pm$ 0.005 ns)

In direct comparison of uncoated and functionalized C8S3-aggregates the lifetime of the excited states differ by a factor of ~2. Such a decreased lifetime is explained by the presence of a fluorescence quencher. The acceptor is acting as a quencher for the donor fluorescence.

From these lifetimes and eq. 2-33 one derives the transfer-efficiency $\eta_{FT,\ time\text{-}resolved}$ from aggregate to shell.

$$\eta_{FT;\ time\text{-}resolved} \cong 61.6\% (\pm 6.2\%)$$

The transfer-efficiency revealed in the preceeding chapter 5.3.2.2 was found through steady-state spectroscopy to be 59.6%, which agrees within the given tolerance. For further discussion the theoretical estimated value of $\eta_{FT,\ calculated}$ has to be found.

5.3.2.5 Theoretical transfer-efficiency

The vast spectral-overlap of aggregate emission and label-absorption, seen in Figure 5-45, causes a large Förster-radius $\mathbf{R_0}$. As depicted in eq. 2-36, the spectral overlap **J** is influencing directly the Förster-Radius $\mathbf{R_0}$.

The quantum-yield of C8O3-aggregates is known [150,151]. It is assumed to be same like that of C8S3, in this case the donor.

$$\Phi_D = 0.02 \pm 0.01$$

With these values $\mathbf{R_0}$ can be calculated, see appendix-chapter 7.2.3:

$$\mathbf{R_0} = (42 \pm 5)\ \text{Å}$$

This gives direct access to the transfer-efficiency of the Förster-transfer. The transfer efficiency is dependent on $\mathbf{R_0}$ and the average donor-acceptor distance **<d>**. This distance **<d>** is derived from eq. 5-4. It is found to be in this case:

$$\mathbf{<d>} = 1.44\ \text{nm}$$

The quenching of the donor, the aggregate, due to the acceptor-labels can be estimated by simple geometric considerations of label-density and –distribution in the aggregate-coating.

The cryo-TEM images revealed for PAH an average coating thickness of 2.5 nm. In order to calculate the transfer-efficiency analytically, assumptions are made in analogy to 5.3.1.2. The transfer efficiency is mainly given by an area $\mathbf{A} = \mathbf{a}^2\pi$ which is defined as the cross section between the aggregate surface and a sphere around the acceptor molecule with radius $\mathbf{R_0}$. This is sketched in Figure 5-51.

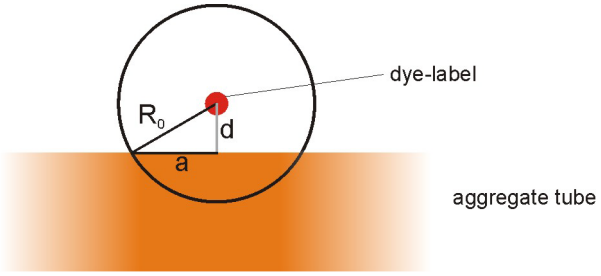

Figure 5-51:
Sketch of acceptor-dye in distance **d** to the aggregate-donor. The aggregate surface is idealized to be flat.

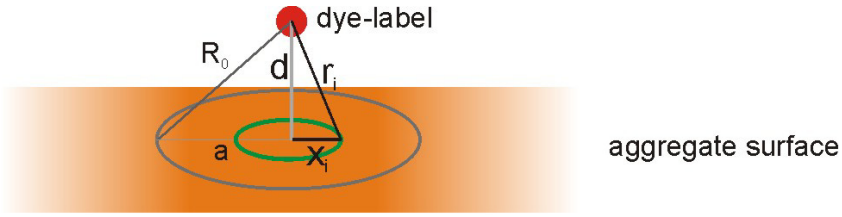

Figure 5-52:
Illustration of area underneath dye-label. The very center of the spot provides highest transfer-efficiency, the edge at distance R_0 from label enables 50% transfer-efficiency. Points with equal distance from label contribute with equal transfer-efficiency, forming circles of equal transfer-efficiency. Total transfer-ratio is derived by summation over all aequi-efficient circles.

Figure 5-51 and Figure 5-52 illustrate geomtric aspects for calculation of transfer-efficiencies from aggregate to acceptor-dyes in the PE-coating. The acceptor-labels drop a circular shadow of effective quenching onto the assumed flat surface of the aggregate. The size of these circles is limited through the Förster-horizon $\mathbf{R_0}$. From the geometric consideration in Figure 5-52, the averaged distance $\mathbf{<d>}$ and Förster-radius $\mathbf{R_0}$ one derives the radius **a** of the areas of effective energy-transfer.

$$\mathbf{a} = 3.95 \text{ nm}$$

The transfer-rate from donor to acceptor of a FRET-couple is given in eq. 2-32. The integration of the transfer-rates over the entire area within the Förster-horizon provides the total transfer-rate. This rate has to be normalized with the number of C8S3-monomer donating energy from within this area. The averaged transfer-rate $\mathbf{<k_{FT}>}$ is found:

$$\left\langle k_{FT} \right\rangle = C_D \int_0^{2\pi} \int_0^a k_D \left(\frac{R_0}{r} \right)^6 x dx d\varphi$$

$$\text{with } r = \sqrt{x^2 + \left\langle d \right\rangle^2}$$

$$\left\langle k_{FT} \right\rangle = 2\pi \cdot C_D k_D \int_0^a \frac{R_0^6}{\left(x^2 + \left\langle d \right\rangle^2 \right)^3} x dx \qquad \text{(eq. 5-13)}$$

The donor-density $\mathbf{C_D}$ is given with the number of C8S3-monomers in the outer wall of the tube per area, in analogy to the acceptor-density $\mathbf{C_A}$ of the previous chapter.

$$\mathbf{C_D} = 0.15 \text{ nm}^{-2}$$

The fluorescence-rate $\mathbf{k_D}$ of C8S3-aggregates can be derived from the lifetime $\boldsymbol{\tau_D}$, obtained in time-resolved measurements.

$$\boldsymbol{\tau_D} = (0.073 \pm 0.005) \text{ ns}$$

$$\mathbf{k_D} = (2.74 \pm 0.05) \cdot 10^8 \text{ s}^{-1}$$

The average areal transfer-rate is found to be

$$\mathbf{\langle k_{FT} \rangle} = (8.151 \pm 0.290) \cdot 10^{10} \text{ s}^{-1} \text{ nm}^{-2}$$

With eq. 5-9 one finds the averaged areal transfer-efficiency $\mathbf{\langle \eta_{FT} \rangle}$ of these spots underneath the label to be

$$\mathbf{\langle \eta_{FT} \rangle} = (99.7 \pm 9.9) \%$$

The evaluation of monomer-numbers in outer-wall of the aggregate and coating reveals also another fact – the label-density. On a 1 nm segment of coated aggregate the coating consists of 974 PAH-monomers. The label-ratio of the investigated PAH-Alexa631 is given with 1%. Therefore approximately 9.7 (~10) dye-labels are located in the aggregate-coating per 1 nm length of wrapped aggregate.

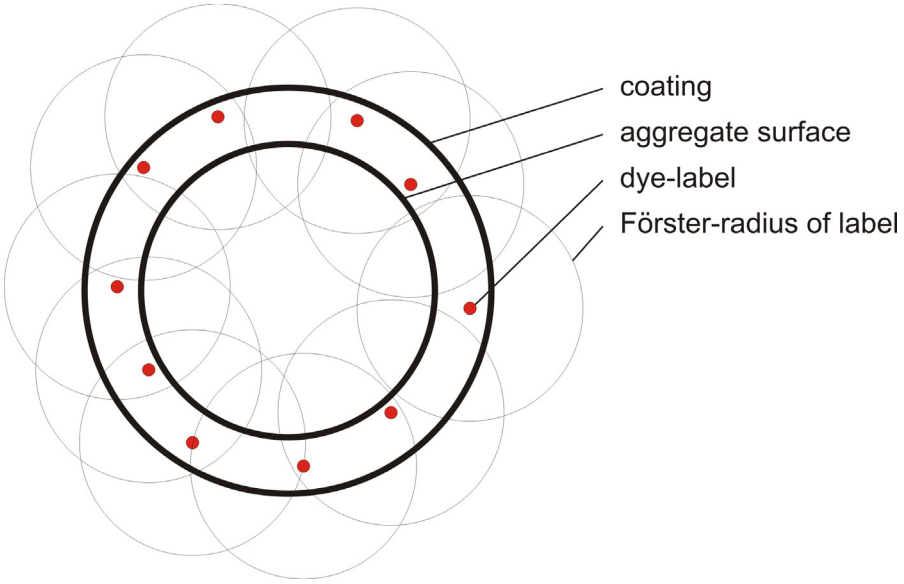

Figure 5-53:
Sketch of wrapped aggregate. Depicted dye-labels in coating are shown with range of effective quenching (Förster-radius).

Figure 5-53 shows the idealised cross-section of functionalized aggregates (of a 1 nm segment). The coating of PAH provides a thickness of 2.5 nm. Within a segment of 1 nm length ~10 labels are located in the coating. Obviously, the Förster-radii of the individual labels overlap. The found averaged transfer-efficiency $\langle\eta_{FT}\rangle$ has to be higher due to overlap of the areas of effective quenching. One assumes the value of $\langle\eta_{FT}\rangle = 99.7\%$ to be the least minimum, calculated value. This high value of $\langle\eta_{FT}\rangle$ is equipollent to entire quenching of the outer wall.

In contrast to this calculated efficiency-value the observed transfer-efficiency of 59.6% and 61.6%, respectively, lack behind by far. This enormous mismatch may be reduced by considering the impact on the inner-wall.

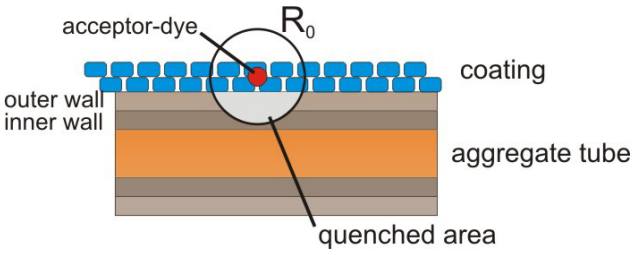

Figure 5-54:
Sketch of effective quenching of aggregate-fluorescence by dye-labels in coating. Although the quenching-efficiency is almost 100% on the outer-wall, the inner-wall is less affected.

As sketched in Figure 5-54, the Förster-radius of the acceptor-dye reaches into the inner-wall. This gives rise to a more detailed view of the aggregate-fluorescence. The total fluorescence intensity is cardinaly originating from the inner-wall. Average-distance between dye-labels and inner wall is larger than distance to outer wall and therefore the average transfer-efficiency from spots on the inner-wall to the labels is smaller. The averaged distance $\mathbf{<d>_{inner}}$ is found to be

$$\mathbf{<d>_{inner}} = \mathbf{<d>} + 2 \text{ nm} = 3.44 \text{ nm}$$

From geometric consideration one finds the radii of quenched spots on the inner wall:

$$\mathbf{a_{inner}} = 2.41 \text{ nm}.$$

The averaged transfer-rate from the inner wall is found to be:

$$\mathbf{<k_{FT}>_{inner}} = (1.3723 \pm 0.0490) \cdot 10^9 \text{ s}^{-1} \text{ nm}^{-2}$$

The areal quenching on these spots on the inner wall can be found:

$$\mathbf{<\eta_{FT}>_{inner}} = (83.6 \pm 8.4) \%.$$

But still, the areas of effective quenching overlap. The calculated value of quenching is assumed as least, minimum quenching on the inner-wall. Even though one assumes the major-fluorescence from the inner-tube, which is estimated by calculation to be quenched 83.6% (at least).

The approximation calculation to determine the estimated quenching-efficiencies from outer- and inner-wall can be supplemented with a numerical approach, see appendix-chapter 7.2.4. The numerical calculation enables a visualization of the quenching efficiency beneath the acceptor-labels.

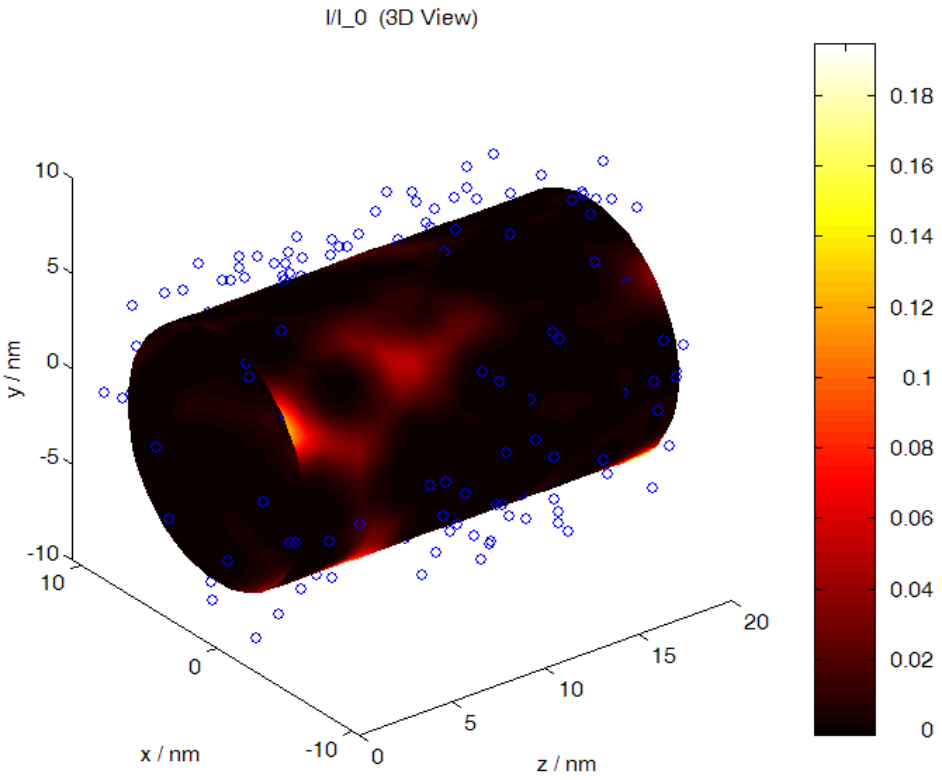

Figure 5-55:
Visualization of numerical calculation of quenching-efficiencies. Depicted is energy-transfer from C8S3-aggregate to Alexa631-acceptors. Shown is the impact of FRET-quenching to the outer wall of the aggregate.
Shown is the fluorescence-intensity I of aggregate-wall, which is 1-η. The overall numerical quenching efficiency $\eta_{numerical}$ = 99.5% is entirely quenching the outer wall.

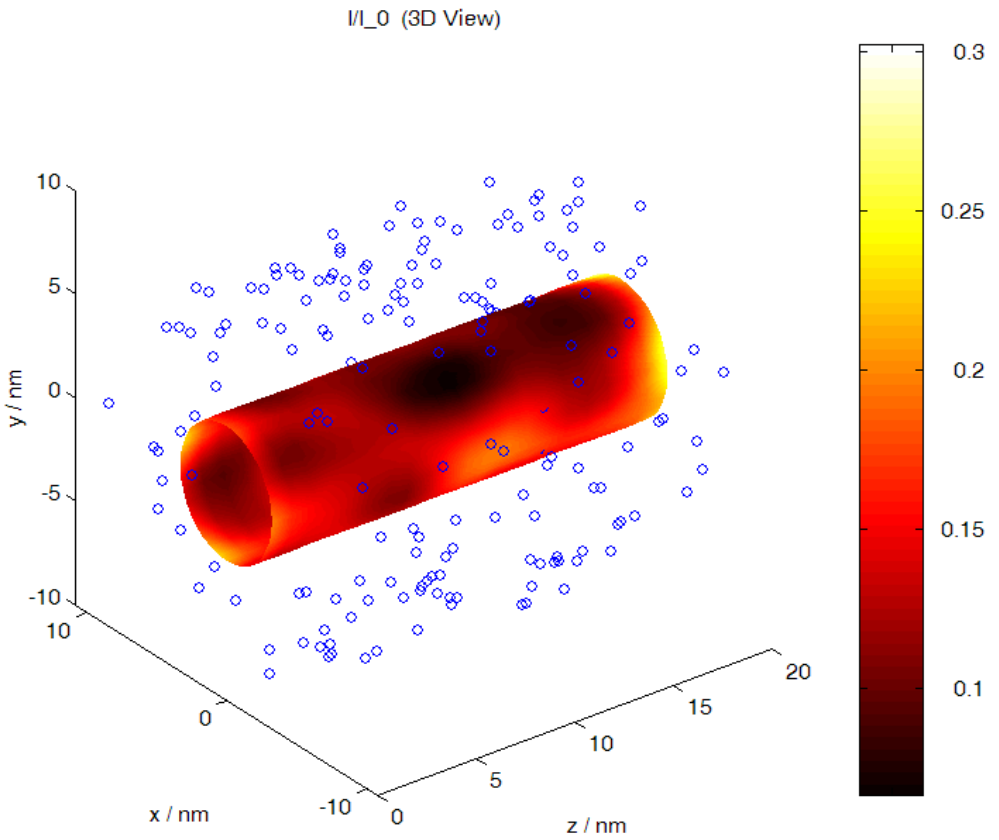

Figure 5-56:
Visualization of numerical calculation of quenching-efficiencies. Depicted is energy-transfer from C8S3-aggregate to Alexa631-acceptors. Shown is the impact of FRET-quenching to the inner wall of the aggregate.
Shown is the fluorescence-intensity I of aggregate-wall, which is 1-η. The overall averaged numerical quenching efficiency $\eta_{numerical,\ inner}$ = (87.5 $\pm$ 2) % is reducing the total fluorescence from the inner-wall to approximately 15% of the original intensity.

The numerical visualization from Figure 5-55 and Figure 5-56 reflect the fluorescence-conditions of the individual walls. The outer wall is assumed to be entirely quenched. No fluorescence is emitted from the outer wall, it appears dark. The inner-wall is only partwise quenched. The quenched areas beneath the acceptor-labels appear like dark shadows on the inner-wall. The total-fluorescence of the inner-wall is reduced to less than 20%. The comparison of the calculated and the numerical values for transfer or quenching-efficiencies η agree within the tolerances, as to be seen in Table 5.

Table 5:
Quenching efficiencies from individual aggregate wall to Alexa631 acceptor-labels

	Calculated $\eta_{calculated}$ in %	Numerical $\eta_{numerical}$ in %
Outer-wall	99.7 ± 9.9	99.5 ± 2.0
Inner-wall	83.6 ± 8.4	87.5 ± 2.0

The total-quenching of the aggregate is found from consideration of transfer-efficiencies from both walls, with respect to their individual contribution to overall aggregate-fluorescence. The combination of quenching-impact on outer- and inner-wall leads to the combined, averaged, least value $\langle\eta_{FT}\rangle_{combined}$.

$$\langle \eta_{FT} \rangle_{combined} = \frac{2 \cdot \langle \eta_{FT} \rangle_{outer} + 1 \cdot \langle \eta_{FT} \rangle_{inner}}{3} \qquad \text{(eq. 5-14)}$$

The total calculated quenching is found to be for the calculated values of inner and outer wall:

$$\langle\eta_{FT}\rangle_{combined} = (89.0 \pm 18.3)\ \%$$

The derived values for total transfer-efficiencies η from steady-state spectroscopy, time-resolved spectroscopy and calculation are given in Table 6.

Table 6:
Values of transfer-efficiency from C8S3-aggregate to Alexa631-acceptors derived by different methods.

Derive-method	Transfer-efficiency η in %
Steady-state spectroscopy	59.6 ± 0.5
Time-resolved spectroscopy	61.6 ± 6.2
Calculation	89.0 ± 18.3

From the comparison of the values for the transfer-efficiency, given in Table 6, it is seen, that both experimentally obtained transfer-efficiencies are almost within the relatively large tolerance of the calculated value. The two experimental results are in good agreement anyway.

Nevertheless, the calculated value exceeds the experimental results. This is due to the over-estimation of the Förster-radius $\mathbf{R_0}$. The calculation of $\mathbf{R_0}$ is dependent on the overlap-integral **J,** the refractive index **n** of the medium between donor and acceptor

and the quantum yield of the donor Φ_D. The latter two are not exactly determined and therefore provide inaccuracies that contribute to the tolerance of R_0, which is why the value of R_0 is possibly overestimated, causing the calculated transfer-efficiency $\eta_{calculated}$ to be overestimated as well.

Both refractive indices, PAH and C8S3-wall, are assumed to be much larger, than that of water [143]. As the Förster-radius R_0 is proportional to n^{-4} the calculated transfer-efficiency estimations are based on high values of R_0 that are actually smaller. The proper values of R_0 are sadly not feasible. Studies on the refractive index of PAH were carried out in ambient-atmosphere. These conditions are comparably dry in contrast to the wet and swollen conditions within the solution.
A comparison with the prior experiment, rhodamin B-donors quenched by the aggregate, is not solving this question. The prior experiment was performed with PDADMAC-wrapping, which ought to have a different refractive index than PAH. Furthermore, it was assumed, that even the outer wall is quenching the rhodamin B donors, which is why no refractive index for the outer-wall would be derived from this energy-transfer.

6 CONCLUSION AND OUTLOOK

الإنسان يحصل على علومه من سطح محيط المعرفة.
أعماق المحيط تبقى بعيدة المنال.

Mankind fetches its knowledge from the surface of the ocean of wisdom. The depth remains out of reach.

Arab locution

6.1 Conclusions

Investigation on uncoated aggregates revealed, that the electrostatic potential of the aggregate-surface can be utilized for further adsorption of PE.

The wrapping attempts with PDADMAC, PEI and PAH proofed the capability of C8S3-aggregates to be wrapped with PEs by electrostatic adsorption without disturbing the fragile aggregate-structure. In contrast to other membrane systems, such as vesicles or cells, the aggregates deliver a simple but sensitive sensor for disorder-effects on molecular-scale: UV/vis-spectroscopy.

Dependent on the individual properties of the wrapping PE the coating of C8S3-aggregates differed in coating-smoothness, length of coated-segments, coating-thickness and coating-ratio. It turned out, that PAH, if applied in high concentration (10^{-3} M), provides an entire coating of 80% of the C8S3-aggregates with an average coating-thickness of 2.5 nm. The spectroscopic changes due to this coating showed only small changes in the J-band, which indicates, that the excitonic energy-migration within the aggregate is maintained.

The application of dye-labelled PEs to wrap C8S3-aggregates delivered functionalized aggregates for energy-transfer measurments. These experiments demonstrate the applicability of the wrapping for build-up of well-defined and complex structures on the nano-scale by means of self-assembly. However, it also shows the limits with respect to spectroscopic investigations. The very asymmetric dye-ratio and the broad absorption with the log lasting tail of emission of the aggregates provides more difficulties than foreseen in the beginning. The spectroscopic investigation on these functionalized aggregates revealed the estimated FRET between dye-labels (rhodamin B) in the coating and the aggregate. It has been shown, that energy transfer from donor-labels in the coating to the C8S3-aggregate is possible and efficient. Energy-transfer from the aggregate to acceptor-labels (Alexa631) are possible, too.

6.2 Outlook

6.2.1 Functionalization with donors and acceptors

To establish a high integrated light-harvesting complex from functionalized C8S3-aggregates one would like to place donor-labels in high number and acceptors for charge-separation in relative low number in the wrapping of aggregates. Donors and acceptor ought to have no or at least weak spectral overlap, so that donors would collect light-energy and transfer it to the aggregate via FRET. This enables an effective extension of the absorption-range of the light-harvesting complex. Acceptor-labels on the aggregate would be pumped by this energy continuously through a second FRET-channel. These acceptors could utilize the donated energy for non-radiative processes, i.e. hydrolysis. Such a 2-channel-FRET complex would than be able to facilitate hydrogen from aqueous environment only through incident light. The complexes ought to form by self-assembly.

6.2.2 Multilayer coating

The polyelectrolyte adsorption on C8S3-aggregates has been performed in analogy to LbL coating of charged colloids. Anyway, the adsorption of one polyelectrolyte is yet only one layer. This gives rise to the adsorption of at least one more layer of an oppositely charged polyelectrolyte, for instance PSS. Such a second layer could increase the structural integrity of the wrapped aggregate and furthermore gives rise to another kind of functionalization, not only by optical means. The second-layer PE could carry a second type of functional groups, i.e. specialized receptors, that exclusively bind to certain ligands, so that functionalized aggregates could be "parked" on estimated positions on surfaces, etc.

6.2.3 Resonant aggregate and dye-label (texasred-PAH)

Another attempt of functionalization is the usage of texasRed-labelled PAH for wrapping of C8S3-aggregates. The spectra of texasred as label on PAH is given in the diagram below in comparison to the spectra of the C8S3-aggregates.

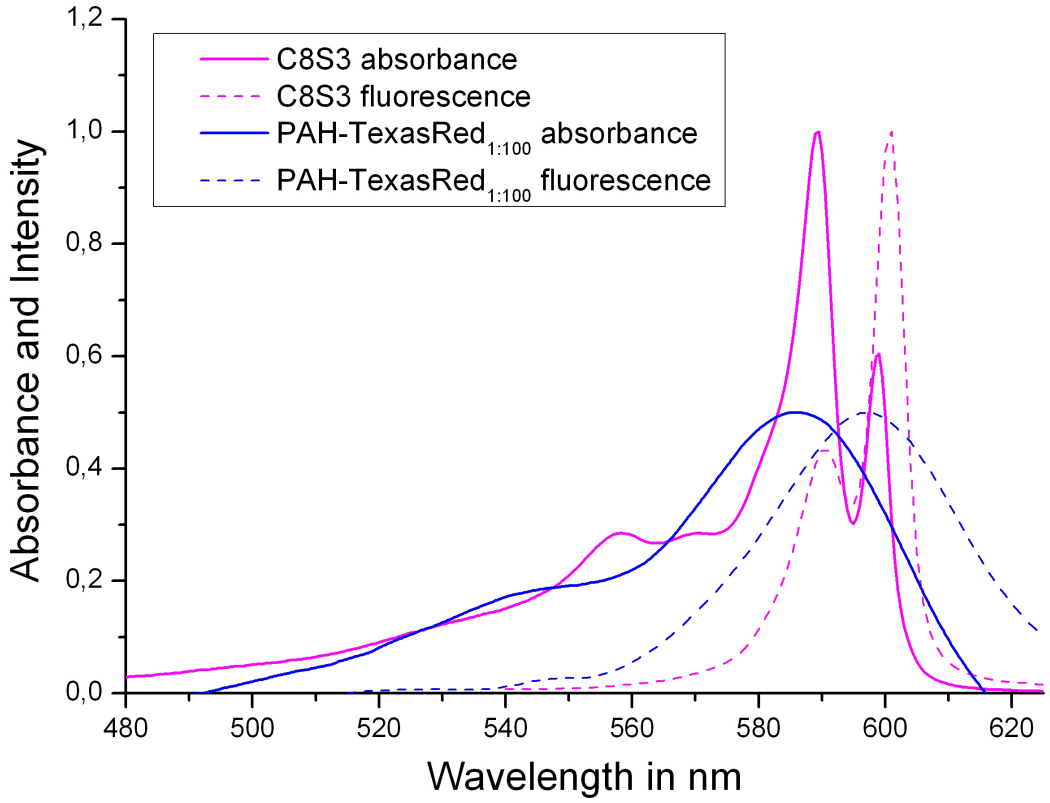

Figure 6-1:
Absorption and emission of uncoated C8S3 aggregates and texasred-labelled PAH (10^{-4} M). Graphs are normalized to 1 (C8S3) or 0,5 (TR), respectively.

As to be seen in Figure 6-1, the spectral overlap of labels and aggregate is entirely in absorption as well as in fluorescence. This leads to indistinguishability of the individual spectra if both species are combined in one solution. Separate excitation of dye-label or aggregate is impossible.

Furthermore label-emission overlaps with aggregate-absorption and aggregate-emission overlaps with label-absorption. This enables efficient energy-transfer from dye-labels to aggregate and at same time allows energy-transfer from aggregate emission to labels. With this aspect the labels are donor and acceptor to the aggregate at the same time.

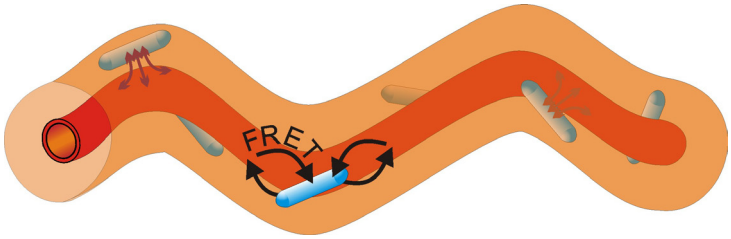

Figure 6-2:
Sketch of C8S3-aggregate with texasred-functionalized wrapping. Förster-transfer is enabled to and from aggregate to dye-labels.

Due to the highly overlapping absorption and emission spectra of C8S3-aggregates and the texasred-labels the transfer efficiency is also high. Excited aggregates pump the dye-labels that pump the aggregate in return.

Considering the very different life-times of the excited states one may assume that an excited aggregate once quenched by texasred-labels is highly probable to be reexcited by the label during the relatively long life-time of texasred. Thus, one should observe **delayed fluorescence** of the aggregate by this process.

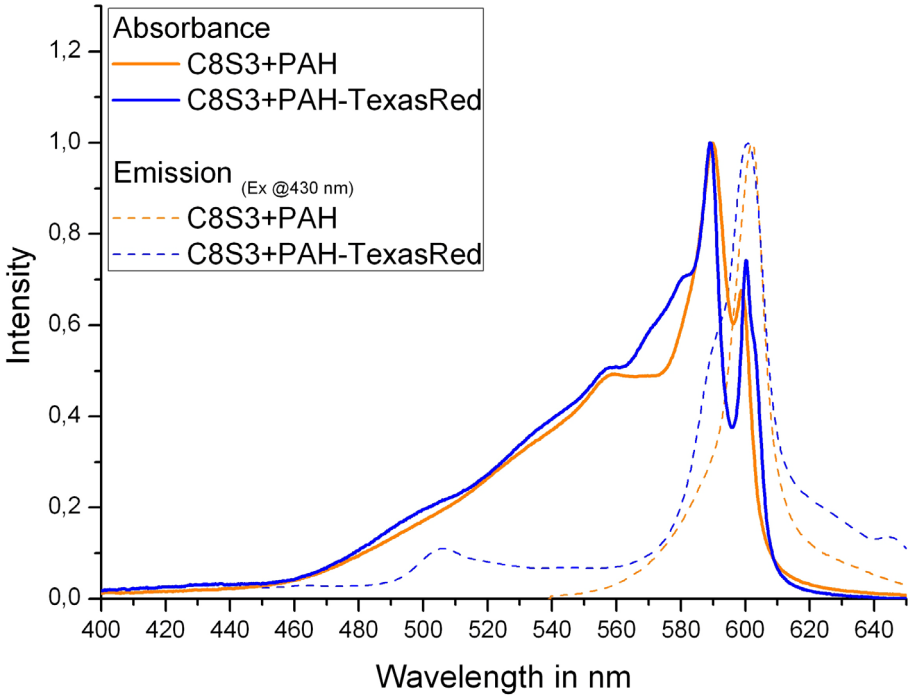

Figure 6-3:
Absorption and emission spectra of PAH-wrapped aggregates. Compared are plain PAH-wrapped aggregates (orange) and texasred functionalized aggregates (blue). Absorbances are given in solid lines, fluorescence is dashed. All spectra are normalized.

The absorbances of plain and functionalized aggregates are obtained with a PE-concentration of 10^{-4} M. Broadening in the J-band peaks on functionalized aggregates are assumed to be due to bundling effects. A small dip at 495 nm on functionalized aggregates might origin from label-fragments that are leftover from label-synthesis.

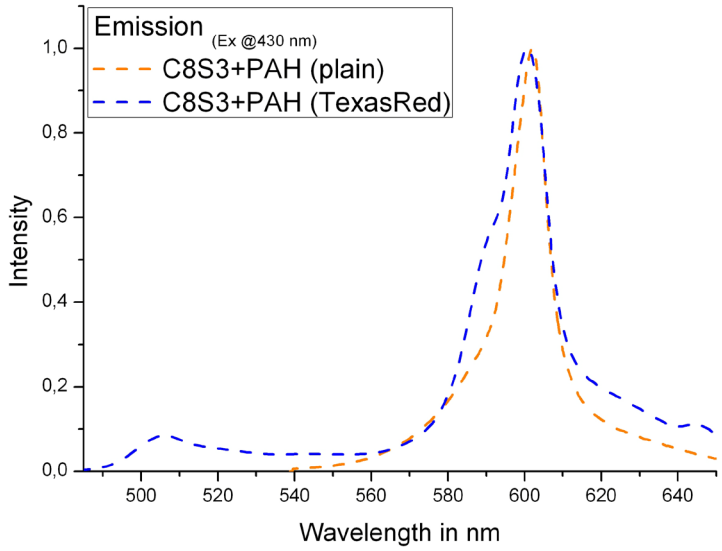

Figure 6-4:
Fluorescence of plain and texasred-functionalized aggregates

The resulting fluorescence of texasred-functionalized aggregates shows a small peak at 505 nm, that is strongly excitation-wavelength dependent, which is assumed to be caused by dye-fragments in the solution. The J-band peak at 599 nm shows a significant shoulder, a possible secondary peak at 590 nm.

A spectral separation of label and aggregate absorption in ensemble is impossible. To proof the assumption of texasred-functionalized aggregates being a self-absorbing complex, one has to perform time-resolved spectroscopy. If the complex of C8S3-aggregates and texasred-labels is indeed self-absorbing, the lifetimes of the excited states of the complex are altered from the individual lifetimes. Although spectrally indistinguishable, the texasred-functionalized aggregate provides a certain ensemble-lifetime. In comparison with lifetime-measurements in absence of an acceptor, investigation of pure solutions, the ensemble would have to show a significant change of excited state lifetime. Excitations from aggregates are carried in the complex from long-life texasred and shortlife (0,15 ns) aggregate. The ensemble lifetime is assumed to be longer than that of pure aggregates, but significantly shorter than pure texasred lifetime, which is in the order of 1 ns.

Anyway, the combination of texasred and aggregates is not assumed to establish a proper donor-acceptor-couple. Investigation concerning energy-transfer from aggregate to label, respectively vice versa, exceeds the frame of this work and remains open question for further investigation.

7 APPENDIX

Сделал дело,
гуляй смело!

If the work is done, you may celebrate!

Russian locution

7.1 Citations

[1] Würthner, Frank; Kaiser, Theo E. and Saha-Möller, Chantu R. (2011): J-Aggregate: von ihrer zufälligen Entdeckung bis zum gezielten supramolekularen Aufbau funktioneller Farbstoffmaterialien, Angew. Chem. (vol. 123), No. 15, pp. 3436-3473. URL: http://dx.doi.org/10.1002/ange.201002307

[2] Jelly, E. E. (1936): Spectral Absorption and Fluorescence of Dyes in the Molecular State, Nature (vol. 138), p. 2.

[3] Jelly, E. E. (1937): Molecular, Nematic and Crystal States of I: I-Diethyl--Cyanine Chloride, Nature (vol. 138), p. 2.

[4] Scheibe, G.; Kandler, L. and Ecker, H. (1937): Polymerisation und polymere Adsorption als Ursache neuartiger Absorptionsbanden von organischen Farbstoffen, Naturwissenschaften (vol. 25), No. 5, pp. 75-75. URL: http://dx.doi.org/10.1007/BF01493278

[5] Scheibe, G. (1937): Über die Veränderlichkeit der Absorptionsspektren in Lösungen und die Nebenvalenzen als ihre Ursache, Angew. Chem. (vol. 50), No. 11, pp. 212-219. URL: http://dx.doi.org/10.1002/ange.19370501103

[6] Scheibe, G.; Schöntag, A. and Katheder, F. (1939): Fluoreszenz und Energiefortleitung bei reversibel polymerisierten Farbstoffen, Naturwissenschaften (vol. 27), No. 29, pp. 499-501. URL: http://dx.doi.org/10.1007/BF01488245

[7] Scheibe, G. (1938): Reversible Polymerisation als Ursache neuartiger Absorptionsbanden von Farbstoffen, Colloid & Polymer Science (vol. 82), No. 1, pp. 1-14. URL: http://dx.doi.org/10.1007/BF01509409

[8] Frenkel, J. (1931): On the Transformation of Light into Heat in Solids. II, Phys. Rev. (vol. 37), No. 10, pp. 1276-1294. URL: http://link.aps.org/doi/10.1103/PhysRev.37.1276

[9] Franck, James and Teller, Edward (1938): Migration and Photochemical Action of Excitation Energy in Crystals, J. Chem. Phys. (vol. 6), No. 12, pp. 861-872. URL: http://link.aip.org/link/?JCP/6/861/1

[10] Knapp, E.W. (1984): Lineshapes of molecular aggregates, exchange narrowing and intersite correlation, Chemical Physics (vol. 85), No. 1, pp. 73-82. URL: http://www.sciencedirect.com/science/article/pii/S0301010484851745

[11] de Boer, Steven; Vink, Kees J. and Wiersma, Douwe A. (1987): Optical dynamics of condensed molecular aggregates: An accumulated photon-echo and hole-burning study of the J-aggregate, Chem. Phys. Lett (vol. 137), No. 2, pp. 99-106. URL: http://www.sciencedirect.com/science/article/pii/0009261487803123

[12] Spano, Francis C. and Mukamel, Shaul (1989): Nonlinear susceptibilities of molecular aggregates: Enhancement of $\chi^{(3)}$ by size, Phys. Rev. A (vol. 40), No. 10, pp. 5783-5801. URL: http://link.aps.org/doi/10.1103/PhysRevA.40.5783

[13] de Boer, Steven and Wiersma, Douwe A. (1990): Dephasing-induced damping of superradiant emission in J-aggregates, Chem. Phys. Lett (vol. 165), No. 1, pp. 45-53. URL: http://www.sciencedirect.com/science/article/pii/000926149087010O

[14] Fidder, Henk; Knoester, Jasper and Wiersma, Douwe A. (1991): Optical properties of disordered molecular aggregates: A numerical study, J. Chem.

Phys. (vol. 95), No. 11, pp. 7880-7890. URL: http://link.aip.org/link/?JCP/95/7880/1

[15] Knoester, Jasper (1993): Nonlinear optical line shapes of disordered molecular aggregates: Motional narrowing and the effect of intersite correlations, J. Chem. Phys. (vol. 99), No. 11, pp. 8466-8479. URL: http://link.aip.org/link/?JCP/99/8466/1

[16] Knoester, Jasper (1993): Third-order optical response of molecular aggregates. Disorder and the breakdown of size-enhancement, Chem. Phys. Lett (vol. 203), No. 4, pp. 371-377. URL: http://www.sciencedirect.com/science/article/pii/000926149385583A

[17] von Berlepsch, H.; Böttcher, C. and Dähne, L. (2000): Structure of J-Aggregates of Pseudoisocyanine Dye in Aqueous Solution, J. Phys. Chem. B (vol. 104), No. 37, pp. 8792-8799. URL: http://dx.doi.org/10.1021/jp000085q

[18] Wennerström, Håkan and Lindman, Björn (1979): Micelles. Physical chemistry of surfactant association, Physics Reports (vol. 52), No. 1, pp. 1-86. URL: http://www.sciencedirect.com/science/article/pii/0370157379900875

[19] Lindman, B. and Wennerstrom, H. (1980): Miceles. Amphiphile aggregation in aqueous solution, Top. Curr. Chem. (vol. 87), pp. 1-87. URL: http://www.ncbi.nlm.nih.gov/pubmed/6987777

[20] Kirstein, Stefan; von Berlepsch, Hans; #246 and ttcher, Christoph (2006): Photo-induced reduction of Noble metal ions to metal nanoparticles on tubular J-aggregates, International Journal of Photoenergy (vol. 2006). URL: http://dx.doi.org/10.1155/IJP/2006/47917

[21] Nakahara, Hiroo; Fukuda, Kiyoshige; Moebius, Dietmar and Kuhn, Hans (1986): Two-dimensional arrangement of chromophores in J aggregates of long-chain merocyanines and its effect on energy transfer in monolayer systems, J. Phys. Chem. (vol. 90), No. 23, pp. 6144-6148. URL: http://dx.doi.org/10.1021/j100281a019

[22] Nakano, Atsushi; Shimizu, Shigeo; Takahashi, Teruo; Nakahara, Hiroo and Fukuda, Kiyoshige (1988): The spectroscopic behaviour of J-aggregates of cyanine dyes without long chains incorporated in the monolayer assemblies, Thin Solid Films (vol. 160), No. 1-2, pp. 303-310. URL: http://www.sciencedirect.com/science/article/pii/0040609088900740

[23] Pawlik, Andreas; Kirstein, Stefan; De Rossi, Umberto and Daehne, Siegfried (1997): Structural Conditions for Spontaneous Generation of Optical Activity in J-Aggregates, J. Phys. Chem. B (vol. 101), No. 29, pp. 5646-5651. URL: http://dx.doi.org/10.1021/jp9708308

[24] Tanford, Charles (1979): Interfacial free energy and the hydrophobic effect, Proc. Natl. Acad. Sci. USA (vol. 76), No. 9, pp. 4175-4176. URL: http://www.pnas.org/content/76/9/4175.abstract

[25] lin; Pugžlys, Audrius; Hania, P. Ralph; von Berlepsch, Hans; Duppen, Koos and Knoester, Jasper (2004): Structure, Spectroscopy, and Microscopic Model of Tubular Carbocyanine Dye Aggregates, J. Phys. Chem. B (vol. 108), No. 39, pp. 14976-14985. URL: http://dx.doi.org/10.1021/jp048288s

[26] von Berlepsch, Hans; Kirstein, Stefan; Hania, P. Ralph; Pugžlys, Audrius and Böttcher, Christoph (2007): Modification of the Nanoscale Structure of the J-Aggregate of a Sulfonate-Substituted Amphiphilic Carbocyanine Dye through Incorporation of Surface-Active Additives, J. Phys. Chem. B (vol. 111), No. 7, pp. 1701-1711. URL: http://dx.doi.org/10.1021/jp065826n

[27] von Berlepsch, Hans; Kirstein, Stefan and Böttcher, Christoph (2003): Controlling the Helicity of Tubular J-Aggregates by Chiral Alcohols, J. Phys. Chem. B (vol. 107), No. 36, pp. 9646-9654. URL: http://dx.doi.org/10.1021/jp0302212

[28] von Berlepsch, H.; Kirstein, S.; Hania, R.; Pugzlys, A. and Bottcher, C. (2007): Modification of the nanoscale structure of the J-aggregate of a sulfonate-substituted amphiphilic carbocyanine dye through incorporation of surface-active additives, J Phys Chem B (vol. 111), No. 7, pp. 1701-11. URL: http://www.ncbi.nlm.nih.gov/pubmed/17261059

[29] Eisele, D. M.; Knoester, J.; Kirstein, S.; Rabe, J. P. and Vanden Bout, D. A. (2009): Uniform exciton fluorescence from individual molecular nanotubes immobilized on solid substrates, Nat. Nanotechnol. (vol. 4), No. 10, pp. 658-63. URL: http://www.ncbi.nlm.nih.gov/pubmed/19809457

[30] lin; Klugkist, Joost A. and Knoester, Jasper (2002): Optical Properties of Helical Cylindrical Molecular Aggregates: The Homogeneous Limit, J. Phys. Chem. B (vol. 106), No. 44, pp. 11474-11486. URL: http://dx.doi.org/10.1021/jp026217s

[31] rthe M.; Berlepsch, Hans v; B rgen P. (2010): Photoinitiated Growth of Sub-7 nm Silver Nanowires within a Chemically Active Organic Nanotubular Template, J. Am. Chem. Soc. (vol. 132), No. 7, pp. 2104-2105. URL: http://dx.doi.org/10.1021/ja907373h

[32] **Larsen, J.; Brüggemann, B.; Andersson, J.; Polivka, T.; Sundström, V. and Akesson, E. (2005): Artificial Antenna Complexes, http://www.chemphys.lu.se/old/kfresearch/den-antennas.html**

[33] Möbius, D. and Kuhn, H. (1979): Monolayer Assemblies of Dyes to Study the Role of Thermal Collisions in Energy Transfer, Israel J. Chem. (vol. 18), pp. 375-384.

[34] Yonezawa, Yoshiro; Kurokawa, Hiroyuki and Sato, Tomoo (1993): Excitation energy transfer between J-aggregates of cyanine dyes in mixed monolayer assemblies, Journal of Luminescence (vol. 54), No. 5, pp. 285-295. URL: http://www.sciencedirect.com/science/article/pii/0022231393900874

[35] Kuhn, H. (1983): Functionalized monolayer assembly manipulation, Thin Solid Films (vol. 99), No. 1-3, pp. 1-16. URL: http://www.sciencedirect.com/science/article/pii/0040609083903528

[36] Berlepsch, Hans v; Ludwig, Kai; Kirstein, Stefan and Böttcher, Christoph (2011): Mixtures of achiral amphiphilic cyanine dyes form helical tubular J-aggregates, Chemical Physics (vol. 385), No. 1-3, pp. 27-34. URL: http://www.sciencedirect.com/science/article/pii/S0301010411001467

[37] De Rossi, Umberto; Dähne, Siegfried; Meskers, Stefan C. J. and Dekkers, Harry P. J. M. (1996): Spontane Bildung von optischer Aktivität in J-Aggregaten mit Davydov-Aufspaltung, Angew. Chem. (vol. 108), No. 7, pp. 827-830. URL: http://dx.doi.org/10.1002/ange.19961080720

[38] Krol, S.; Diaspro, A.; Magrassi, R.; Ballario, P.; Grimaldi, B.; Filetici, P.; Ornaghi, P.; Ramoino, P. and Gliozzi, A. (2004): Nanocapsules: coating for living cells, IEEE Trans Nanobioscience (vol. 3), No. 1, pp. 32-8. URL: http://www.ncbi.nlm.nih.gov/pubmed/15382641

[39] Caruso, Frank; Yang, Wenjun; Trau, Dieter and Renneberg, Reinhard (2000): Microencapsulation of Uncharged Low Molecular Weight Organic Materials

by Polyelectrolyte Multilayer Self-Assembly†, Langmuir (vol. 16), No. 23, pp. 8932-8936. URL: http://dx.doi.org/10.1021/la000401s

[40] Donath, Edwin; Sukhorukov, Gleb B.; Caruso, Frank; Davis, Sean A. and Möhwald, Helmuth (1998): Neuartige Polymerhohlkörper durch Selbstorganisation von Polyelektrolyten auf kolloidalen Templaten, Angew. Chem. (vol. 110), No. 16, pp. 2323-2327. URL: http://dx.doi.org/10.1002/(SICI)1521-3757(19980817)110:16<2323::AID-ANGE2323>3.0.CO;2-Z

[41] Sukhorukov, Gleb B.; Donath, Edwin; Davis, Sean; Lichtenfeld, Heinz; Caruso, Frank; Popov, Victor I. and Möhwald, Helmuth (1998): Stepwise polyelectrolyte assembly on particle surfaces: a novel approach to colloid design, Polymers for Advanced Technologies (vol. 9), No. 10-11, pp. 759-767. URL: http://dx.doi.org/10.1002/(SICI)1099-1581(1998100)9:10/11<759::AID-PAT846>3.0.CO;2-Q

[42] Sukhorukov, Gleb B.; Donath, Edwin; Lichtenfeld, Heinz; Knippel, Eberhard; Knippel, Monika; Budde, Axel and Möhwald, Helmuth (1998): Layer-by-layer self assembly of polyelectrolytes on colloidal particles, Colloids and Surfaces A: Physicochemical and Engineering Aspects (vol. 137), No. 1-3, pp. 253-266. URL: http://www.sciencedirect.com/science/article/pii/S0927775798002131

[43] Caruso, Frank; Lichtenfeld, Heinz; Giersig, Michael and Möhwald, Helmuth (1998): Electrostatic Self-Assembly of Silica Nanoparticle−Polyelectrolyte Multilayers on Polystyrene Latex Particles, J. Am. Chem. Soc. (vol. 120), No. 33, pp. 8523-8524. URL: http://dx.doi.org/10.1021/ja9815024

[44] Thomas, James L. and Tirrell, David A. (1992): Polyelectrolyte-sensitized phospholipid vesicles, Accounts of Chemical Research (vol. 25), No. 8, pp. 336-342. URL: http://dx.doi.org/10.1021/ar00020a003

[45] Tiourina, O. P.; Radtchenko, I.; Sukhorukov, G. B. and Möhwald, H. (2002): Artificial Cell Based on Lipid Hollow Polyelectrolyte Microcapsules: Channel Reconstruction and Membrane Potential Measurement, Journal of Membrane Biology (vol. 190), No. 1, pp. 9-16. URL: http://dx.doi.org/10.1007/s00232-002-1018-4

[46] Troutier, Anne-Lise and Ladavière, Catherine (2007): An overview of lipid membrane supported by colloidal particles, Advances in Colloid and Interface Science (vol. 133), No. 1, pp. 1-21. URL: http://www.sciencedirect.com/science/article/pii/S0001868607000346

[47] Antonietti, Markus; Kaul, Antje and Thuenemann, Andreas (1995): Complexation of lecithin with cationic polyelectrolytes: "Plastic membranes" as models for the structure of the cell membrane?, Langmuir (vol. 11), No. 7, pp. 2633-2638. URL: http://dx.doi.org/10.1021/la00007a050

[48] Grecco, H. E.; Lidke, K. A.; Heintzmann, R.; Lidke, D. S.; Spagnuolo, C.; Martinez, O. E.; Jares-Erijman, E. A. and Jovin, T. M. (2004): Ensemble and single particle photophysical properties (two-photon excitation, anisotropy, FRET, lifetime, spectral conversion) of commercial quantum dots in solution and in live cells, Microsc. Res. Techniq. (vol. 65), No. 4-5, pp. 169-179. URL: http://dx.doi.org/10.1002/jemt.20129

[49] Spitz, Chistian; Dähne, Siegfried; Ouart, André and Abraham, Hans-Werner (2000): Proof of Chirality of J-Aggregates Spontaneously and Enantioselectively Generated from Achiral Dyes, J. Phys. Chem. B (vol. 104), No. 36, pp. 8664-8669. URL: http://dx.doi.org/10.1021/jp001805w

[50] Althoff, Helga; Bornowski, Barbara and Dähne, Siegfried (1977): Elektrocyclische Synthese von aromatischen Aldehyden aus kettenförmigen Polymethinfarbstoffen, Journal für Praktische Chemie (vol. 319), No. 6, pp. 890-894. URL: http://dx.doi.org/10.1002/prac.19773190609

[51] Markov, R V; Plekhanov, A I; Ivanova, Z M; Orlova, N A and Shelkovnikov, Vladimir V (2001): Resonance absorber based on thin films of pseudoisocyanine J-aggregates, Quantum Electronics (vol. 31), No. 12, pp. 1063-1066.

[52] Israelachvili, Jacob N.; Mitchell, D. John and Ninham, Barry W. (1976): Theory of self-assembly of hydrocarbon amphiphiles into micelles and bilayers, J. Chem. Soc. Farad T 2 (vol. 72), pp. 1525-1568. URL: http://dx.doi.org/10.1039/F29767201525

[53] Israelachvili, J. N.; Mitchell, D. J. and Ninham, B. W. (1977): Theory of self-assembly of lipid bilayers and vesicles, Biochim. Biophys. Acta (vol. 470), No. 2, pp. 185-201. URL: http://www.ncbi.nlm.nih.gov/pubmed/911827

[54] von Berlepsch, H.; Böttcher, C.; Ouart, A.; Burger, C.; Dähne, S. and Kirstein, S. (2000): Supramolecular Structures of J-Aggregates of Carbocyanine Dyes in Solution, J. Phys. Chem. B (vol. 104), No. 22, pp. 5255-5262. URL: http://dx.doi.org/10.1021/jp000220z

[55] von Berlepsch, H.; Böttcher, C.; Ouart, A.; Regenbrecht, M.; Akari, S.; Keiderling, U.; Schnablegger, H.; Dähne, S. and Kirstein, S. (2000): Surfactant-Induced Changes of Morphology of J-Aggregates: Superhelix-to-Tubule Transformation, Langmuir (vol. 16), No. 14, pp. 5908-5916. URL: http://dx.doi.org/10.1021/la000014i

[56] von Berlepsch, H.; Kirstein, S. and Böttcher, C. (2002): Effect of Alcohols on J-Aggregation of a Carbocyanine Dye, Langmuir (vol. 18), No. 20, pp. 7699-7705. URL: http://dx.doi.org/10.1021/la0203640

[57] Davydov, Alexander Sergeevich (1971): Theory of Molecular Excitons, Plenum, New York.

[58] Kirstein, S. and Mohwald, H. (1995): Herringbone structure in two-dimensional single crystals of cyanine dyes. II. Optical properties, The Journal of Chemical Physics (vol. 103), No. 2, pp. 826-833. URL: http://link.aip.org/link/?JCP/103/826/1

[59] **Knoester, Jasper (2002): Proceedings of the International School of Physics "Enrico Fermi" Course SXLIX**

[60] Davydov, Alexander Sergeevich (1964): THE THEORY OF MOLECULAR EXCITONS, Soviet Physics Uspekhi (vol. 7), No. 2, p. 145. URL: http://stacks.iop.org/0038-5670/7/i=2/a=R01

[61] Hochstrasser, Robin M. and Kasha, Michael (1964): APPLICATION OF THE EXCITON MODEL TO MONO-MOLECULAR LAMELLAR SYSTEMS*, Photochem. Photobiol. (vol. 3), No. 4, pp. 317-331. URL: http://dx.doi.org/10.1111/j.1751-1097.1964.tb08155.x

[62] Hochstrasser, Robin M. and Whiteman, John D. (1972): Exciton Band Structure and Properties of a Real Linear Chain in a Molecular Crystal, J. Chem. Phys. (vol. 56), No. 12, pp. 5945-5958. URL: http://link.aip.org/link/?JCP/56/5945/1

[63] Didraga, Cătălin and Knoester, Jasper (2002): Exchange narrowing in circular and cylindrical molecular aggregates: degenerate versus nondegenerate states, Chemical Physics (vol. 275), No. 1-3, pp. 307-318. URL: http://www.sciencedirect.com/science/article/pii/S0301010401005146

[64] lin; Knoester, Jasper and Duppen, Koos (2004): Cylindrical Aggregates of TDBC: Linear and Nonlinear Optical Properties Versus Morphology, Solid State Phenomena (vol. Self-Formation Theory and Applications), pp. 201-206.

[65] Grover, M. and Silbey, R. (1971): Exciton Migration in Molecular Crystals, J. Chem. Phys. (vol. 54), No. 11, pp. 4843-4851. URL: http://link.aip.org/link/?JCP/54/4843/1

[66] Silbey, R (1976): Electronic Energy Transfer in Molecular Crystals, Annu. Rev. Phys. Chem. (vol. 27), No. 1, pp. 203-223. URL: http://www.annualreviews.org/doi/abs/10.1146/annurev.pc.27.100176.001223

[67] Friend, R. H.; Gymer, R. W.; Holmes, A. B.; Burroughes, J. H.; Marks, R. N.; Taliani, C.; Bradley, D. D. C.; Santos, D. A. Dos; Bredas, J. L.; Logdlund, M. and Salaneck, W. R. (1999): Electroluminescence in conjugated polymers, Nature (vol. 397), No. 6715, pp. 121-128. URL: http://dx.doi.org/10.1038/16393

[68] Wohlgenannt, M.; Tandon, Kunj; Mazumdar, S.; Ramasesha, S. and Vardeny, Z. V. (2001): Formation cross-sections of singlet and triplet excitons in [pi]-conjugated polymers, Nature (vol. 409), No. 6819, pp. 494-497. URL: http://dx.doi.org/10.1038/35054025

[69] Möbius, Dietmar (1995): Scheibe Aggregates, Adv. Mater. (vol. 7), No. 5, pp. 437-444. URL: http://dx.doi.org/10.1002/adma.19950070503

[70] Kühn, Oliver; Renger, Thomas and May, Volkhard (1996): Theory of exciton-vibrational dynamics in molecular dimers, Chemical Physics (vol. 204), No. 1, pp. 99-114. URL: http://www.sciencedirect.com/science/article/pii/0301010495004483

[71] Muthukumar, M. (1987): Adsorption of a polyelectrolyte chain to a charged surface, The Journal of Chemical Physics (vol. 86), No. 12, pp. 7230-7235. URL: http://link.aip.org/link/?JCP/86/7230/1

[72] Muthukumar, M.; Ober, C. K. and Thomas, E. L. (1997): Competing Interactions and Levels of Ordering in Self-Organizing Polymeric Materials, Science (vol. 277), No. 5330, pp. 1225-1232. URL: http://www.sciencemag.org/content/277/5330/1225.abstract

[73] Muthukumar, M. (1996): Double screening in polyelectrolyte solutions: Limiting laws and crossover formulas, The Journal of Chemical Physics (vol. 105), No. 12, pp. 5183-5199. URL: http://link.aip.org/link/?JCP/105/5183/1

[74] Kunze, K.-K. and Netz, R. R. (2002): Morphologies of semiflexible polyelectrolyte complexes, EPL (Europhysics Letters) (vol. 58), No. 2, p. 299. URL: http://stacks.iop.org/0295-5075/58/i=2/a=299

[75] Shafir, Adi; Andelman, David and Netz, Roland R. (2003): Adsorption and depletion of polyelectrolytes from charged surfaces, Chemical Physics (vol. 119), No. 4, pp. 2355-2362. URL: http://link.aip.org/link/?JCP/119/2355/1

[76] Gössl, I. M. (2003): Supramolecular structures of dendronized polymers and DNA on solid substrates, Ph.D. , Humboldt-Universität zu Berlin.

[77] Cantor, Charles R. and Schimmel, Paul Reinhard (1980): Biophysical Chemistry, Part 2, 1st edition ed., Techniques for the Study of Biological Structure and Function (Pt. 2), W. H. Freeman and Company; 1st edition (April 15, 1980), ISBN: 0716711907.

[78] Förster, Th (1948): Zwischenmolekulare Energiewanderung und Fluoreszenz, Annalen der Physik (vol. 437), No. 1-2, pp. 55-75. URL: http://dx.doi.org/10.1002/andp.19484370105

[79] Richter, Bernd and Kirstein, Stefan (1999): Excitation energy transfer between molecular thin layers of poly(phenylene vinylene) and dye labeled poly(allylamine) in layer-by-layer self-assembled films, The Journal of Chemical Physics (vol. 111), No. 11, pp. 5191-5200. URL: http://link.aip.org/link/?JCP/111/5191/1

[80] Inacker, O. and Kuhn, H. (1974): Energy transfer from dye to specific singlet or triplet energy acceptors in monolayer assemblies, Chem. Phys. Lett (vol. 27), No. 3, pp. 317-321. URL: http://www.sciencedirect.com/science/article/pii/0009261474902322

[81] De Broglie, L. (1923): Waves and quanta, Nature (vol. 112), pp. 540-540. URL: <Go to ISI>://WOS:000188272400252

[82] Reimer, L. (1989): Transmission electron microscopy: physics of image formation and microanalysis, 2. ed., Springer-Verlag, Berlin, New York.

[83] **PLANO (2006): Zubehör für Elektronenmikroskopie (PLANO Katalog Nummer 9), GmbH, Plano.**

[84] Bogaerts, Annemie; Neyts, Erik; Gijbels, Renaat and van der Mullen, Joost (2002): Gas discharge plasmas and their applications, Spectrochim. Acta Part B (vol. 57), No. 4, pp. 609-658. URL: http://www.sciencedirect.com/science/article/pii/S0584854701004062

[85] Dubochet, Jacques; Adrian, Marc; Lepault, Jean and McDowall, Alasdair W. (1985): Emerging techniques: Cryo-electron microscopy of vitrified biological specimens, Trends in Biochemical Sciences (vol. 10), No. 4, pp. 143-146. URL: http://www.sciencedirect.com/science/article/pii/0968000485901501

[86] Luscher, C.; Balasa, A.; Fröhling, A.; Ananta, E. and Knorr, D. (2004): Effect of High-Pressure-Induced Ice I-to-Ice III Phase Transitions on Inactivation of Listeria innocua in Frozen Suspension, Appl. Environ. Microbiol. (vol. 70), No. 7, pp. 4021-4029. URL: http://aem.asm.org/content/70/7/4021.abstract

[87] Poole, Peter H.; Essmann, Ulrich; Sciortino, Francesco and Stanley, H. Eugene (1993): Phase diagram for amorphous solid water, Phys. Rev. (vol. 48), No. 6, pp. 4605-4610. URL: http://link.aps.org/doi/10.1103/PhysRevE.48.4605

[88] Dubochet, Jacques; Richter, K.; Roy, H. V. and McDowall, Alasdair W. (1991): Freezing: facts and hypothesis, Scanning Microsc. Suppl. (vol. 5), No. 4, pp. S11-5; discussion S15-6. URL: http://www.ncbi.nlm.nih.gov/pubmed/1822020

[89] Dubochet, Jacques (2007): The physics of rapid cooling and its implications for cryoimmobilization of cells, Methods Cell Biol. (vol. 79), pp. 7-21. URL: http://www.ncbi.nlm.nih.gov/pubmed/17327150

[90] Studer, D.; Michel, M.; Wohlwend, M.; Hunziker, E. B. and Buschmann, M. D. (1995): Vitrification of articular cartilage by high-pressure freezing, Journal of Microscopy (vol. 179), No. 3, pp. 321-322. URL: http://dx.doi.org/10.1111/j.1365-2818.1995.tb03648.x

[91] Al-Amoudi, Ashraf; Chang, Jiin-Ju; Leforestier, Amelie; McDowall, Alasdair; Salamin, Lauree Michel; Norlen, Lars P. O.; Richter, Karsten; Sartori Blanc, Nathalie ; Studer, Daniel and Dubochet, Jacques (2004): Cryo-electron microscopy of vitreous sections, EMBO J (vol. 23), No. 18, pp. 3583-3588. URL: http://dx.doi.org/10.1038/sj.emboj.7600366

[92] Dubochet, Jacques; Chang, Jiin-Ju; Freeman, R.; Lepault, Jean and McDowall, Alasdair W. (1982): Frozen aqueous suspensions,

Ultramicroscopy (vol. 10), No. 1-2, pp. 55-61. URL: http://www.sciencedirect.com/science/article/pii/0304399182901875

[93] Lobban, C.; Finney, J. L. and Kuhs, W. F. (1998): The structure of a new phase of ice, Nature (vol. 391), No. 6664, pp. 268-270. URL: http://dx.doi.org/10.1038/34622

[94] Siegel, D. P.; Green, W. J. and Talmon, Y. (1994): The mechanism of lamellar-to-inverted hexagonal phase transitions: a study using temperature-jump cryo-electron microscopy, Biophysical Journal (vol. 66), No. 2, Part 1, pp. 402-414. URL: http://www.sciencedirect.com/science/article/pii/S0006349594807908

[95] Stark, Holger; Zemlin, Friedrich and Boettcher, Christoph (1996): Electron radiation damage to protein crystals of bacteriorhodopsin at different temperatures, Ultramicroscopy (vol. 63), No. 2, pp. 75-79. URL: http://www.sciencedirect.com/science/article/pii/0304399196000459

[96] Siegel, B. M. and Beaman, D. R. (1975): Physical Aspects of Electron Microscopy and Microbeam Analysis 1 st. ed., Wiley, ISBN: 0471790206.

[97] Dubochet, Jacques; Adrian, Marc; Chang, Jiin-Ju; Homo, Jean-Claude; Lepault, Jean; McDowall, Alasdair and Schultz, Patrick (1988): Cryo-electron microscopy of vitrified specimens, Q. Rev. Biophys. (vol. 21), No. 2, pp. 129-228. URL: http://www.ncbi.nlm.nih.gov/pubmed/3043536

[98] Grubb, D. T. (1974): Radiation damage and electron microscopy of organic polymers, Mater. Sci. (vol. 9), No. 10, pp. 1715-1736. URL: http://dx.doi.org/10.1007/BF00540772

[99] Sartori Blanc, Nathalie; Studer, D.; Ruhl, K. and Dubochet, Jacques (1998): Electron beam-induced changes in vitreous sections of biological samples, Journal of Microscopy (vol. 192), No. 2, pp. 194-201. URL: http://dx.doi.org/10.1046/j.1365-2818.1998.00420.x

[100] Egerton, Ray F.; Li, P. and Malac, M. (2004): Radiation damage in the TEM and SEM, Micron (vol. 35), No. 6, pp. 399-409. URL: http://www.sciencedirect.com/science/article/pii/S0968432804000381

[101] Zemlin, F. (1998): Image Formation in High-Resolution Electron Microscopy, Cryst. Res. Technol. (vol. 33), No. 7-8, pp. 1097-1111. URL: http://dx.doi.org/10.1002/(SICI)1521-4079(199810)33:7/8<1097::AID-CRAT1097>3.0.CO;2-X

[102] Scherzer, O. (1949): The Theoretical Resolution Limit of the Electron Microscope, J. Appl. Phys. (vol. 20), No. 1, pp. 20-29. URL: http://link.aip.org/link/?JAP/20/20/1

[103] **Böttcher, Christoph (2006): Kryo-Elektronenmikroskopie und 3D-Rekonstruktion von Makromolekülen, Berlin**

[104] Jin, Q.; Wilkinson, D. S. and Weatherly, G. C. (1998): Determination of Grain-Boundary Film Thickness by the Fresnel Fringe Imaging Technique, Journal of the European Ceramic Society (vol. 18), No. 15, pp. 2281-2286. URL: http://www.sciencedirect.com/science/article/pii/S095522199800140X

[105] Stelzle, M.; Miehlich, R. and Sackmann, E. (1992): Two-dimensional microelectrophoresis in supported lipid bilayers, Biophysical Journal (vol. 63), No. 5, pp. 1346-1354. URL: http://www.sciencedirect.com/science/article/pii/S0006349592817125

[106] Beckman, Alexander L. and Eisenman, Joseph S. (1970): Microelectrophoresis of Biogenic Amines on Hypothalamic Thermosensitive Cells, Science (vol. 170), No. 3955, pp. 334-336. URL: http://www.sciencemag.org/content/170/3955/334.abstract

[107] **ZetaMeter Zeta Potential: A Complete Course in 5 Minutes**
[108] Doane, T. L.; Chuang, C. H.; Hill, R. J. and Burda, C. (2011): Nanoparticle zeta -Potentials, Acc Chem Res. URL: http://www.ncbi.nlm.nih.gov/pubmed/22074988
[109] Seaman, G. V. F. and Heard, D. H. (1961): Methods: A Microelectrophoresis Chamber of Small Volume for Use with Biological Systems, Blood (vol. 18), No. 5, pp. 599-604. URL: http://bloodjournal.hematologylibrary.org/content/18/5/599.abstract
[110] **JASCO (2006): FP-6500 Spectrofluorometer Hardware Manual, GmbH, JASCO.**
[111] **SHIMADZU (1992): Instruction Manual UV-2101/3101PC**
[112] Flissikowski, T.; Hundt, A.; Lowisch, M.; Rabe, M. and Henneberger, F. (2001): Photon Beats from a Single Semiconductor Quantum Dot, Phys. Rev. Lett. (vol. 86), No. 14, pp. 3172-3175. URL: http://link.aps.org/doi/10.1103/PhysRevLett.86.3172
[113] Gomes, A. S. L. and Taylor, J. R. (1986): Direct measurement of the picosecond decay time of the J aggregate of pseudoisocyanine iodide using an optically compressed frequency-doubled continuous wave Nd—YAG laser and a synchronously operating streak camera, J. Photochem. (vol. 32), No. 3, pp. 325-330. URL: http://www.sciencedirect.com/science/article/pii/0047267086870794
[114] Feilitzsch, T. (2004): On the mechanism of photoinduced electron transfer in bridged donor-acceptor systems: ferrocenophane-nileblue and rhodamine6G endcapping the DNA duplex, Ph.D, Technische Universität, München. URL: http://books.google.com/books?id=dW_yPAAACAAJ
[115] Blumstengel, S.; Sadofev, S.; Xu, C.; Puls, J.; Johnson, R. L.; Glowatzki, H.; Koch, N. and Henneberger, F. (2008): Electronic coupling in organic-inorganic semiconductor hybrid structures with type-II energy level alignment, Physical Review B (vol. 77), No. 8, p. 085323. URL: http://link.aps.org/doi/10.1103/PhysRevB.77.085323
[116] Kirstein, Stefan and Daehne, Siegfried (2006): J-aggregates of amphiphilic cyanine dyes: Self-organization of artificial light harvesting complexes, International Journal of Photoenergy (vol. 2006). URL: http://dx.doi.org/10.1155/IJP/2006/20363
[117] lin; Pugžlys, Audrius and Böttcher, Christoph (2003): Stabilization of Individual Tubular J-Aggregates by Poly(vinyl alcohol), J. Phys. Chem. B (vol. 107), No. 51, pp. 14176-14184. URL: http://dx.doi.org/10.1021/jp030526g
[118] **FEW, FEW Chemicals, Wolfen.**
[119] Dupuis, Marc; Denis-Mize, Kimberly; Woo, Carolyn; Goldbeck, Cheryl; Selby, Mark J.; Chen, Minchao; Otten, Gillis R.; Ulmer, Jeffrey B.; Donnelly, John J.; Ott, Gary and McDonald, Donald M. (2000): Distribution of DNA Vaccines Determines Their Immunogenicity After Intramuscular Injection in Mice, J. Immunol. (vol. 165), No. 5, pp. 2850-2858. URL: http://jimmunol.org/content/165/5/2850.abstract
[120] Wischerhoff, E.; Glatzel, S.; Uhlig, K.; Lankenau, A.; Lutz, J. F. and Laschewsky, A. (2009): Tuning the thickness of polymer brushes grafted from nonlinearly growing multilayer assemblies, Langmuir (vol. 25), No. 10, pp. 5949-56. URL: http://www.ncbi.nlm.nih.gov/pubmed/19358594
[121] **Wischerhoff, E. and Laschewsky, A. (2009), 031111-4L and 031118-4L**
[122] **AOKIN (2009), Lot 09/01-10**

[123] Hong, H.; Davidov, D.; Chayet, H.; Faraggi, E. Z.; Tarabia, M.; Avny, Y.; Neumann, R. and Kirstein, S. Blue luminescence induced by confinement in self-assembled films, Supramolecular Science (vol. 4), No. 1-2, pp. 67-73. URL: http://www.sciencedirect.com/science/article/pii/S0968567796000429

[124] Lvov, Yuri; Antipov, Alexei A.; Mamedov, Arif; Möhwald, Helmuth and Sukhorukov, Gleb B. (2001): Urease Encapsulation in Nanoorganized Microshells, Nano Letters (vol. 1), No. 3, pp. 125-128. URL: http://dx.doi.org/10.1021/nl0100015

[125] Netz, Roland R. and Andelman, David (2003): Neutral and charged polymers at interfaces, Physics Reports (vol. 380), No. 1-2, pp. 1-95. URL: http://www.sciencedirect.com/science/article/pii/S0370157303001182

[126] Schmitt, J.; Mächtle, P.; Eck, D.; Möhwald, H. and Helm, C. A. (1999): Preparation and Optical Properties of Colloidal Gold Monolayers, Langmuir (vol. 15), No. 9, pp. 3256-3266. URL: http://dx.doi.org/10.1021/la981078k

[127] Lowack, K. and Helm, C. A. (1998): Molecular Mechanisms Controlling the Self-Assembly Process of Polyelectrolyte Multilayers, Macromolecules (vol. 31), No. 3, pp. 823-833. URL: http://dx.doi.org/10.1021/ma9614454

[128] Schlenoff, J. B.; Rmaile, A. H. and Bucur, C. B. (2008): Hydration contributions to association in polyelectrolyte multilayers and complexes: visualizing hydrophobicity, J. Am. Chem. Soc. (vol. 130), No. 41, pp. 13589-97. URL: http://www.ncbi.nlm.nih.gov/pubmed/18798621

[129] Schlenoff, J. B. (2009): Retrospective on the future of polyelectrolyte multilayers, Langmuir (vol. 25), No. 24, pp. 14007-10. URL: http://www.ncbi.nlm.nih.gov/pubmed/19670891

[130] Eisfeld, A.; Vlaming, S. M.; Malyshev, V. A. and Knoester, Jasper (2010): Excitons in molecular aggregates with Levy-type disorder: anomalous localization and exchange broadening of optical spectra, Phys. Rev. Lett. (vol. 105), No. 13, p. 137402. URL: http://www.ncbi.nlm.nih.gov/pubmed/21230810

[131] Weber, C. M. (2008): Oxidation of double-walled tubular J-aggregates, Diploma, Institute of Pyhsics, Humboldt Universität, Berlin.

[132] Schön, S. (2009): Grundlegende Untersuchungen zur anorganischen Umhüllung amphiphiler Cyaninfarbstoffaggregate, Diploma, Institute of Physics, Humboldt Universität, Berlin.

[133] Kirstein, Stefan; von Berlepsch, Hans; Böttcher, Christoph; Burger, Christian; Ouart, Andre; Reck, Günter and Dähne, Siegfried (2000): Chiral J-Aggregates Formed by Achiral Cyanine Dyes, ChemPhysChem (vol. 1), No. 3, pp. 146-150. URL: http://dx.doi.org/10.1002/1439-7641(20001103)1:3<146::AID-CPHC146>3.0.CO;2-Y

[134] Evans, F. D. and Wennerström, H. (1999): The Colloidal domain : where physics, chemistry and biology meet, 2 nd. ed., Wiley, ISBN: 978-0-471-24247-5.

[135] **Poblenz, E. (2009): Bundling of Aggregates**

[136] Caruso, Frank; Trau, Dieter; Möhwald, Helmuth and Renneberg, Reinhard (2000): Enzyme Encapsulation in Layer-by-Layer Engineered Polymer Multilayer Capsules, Langmuir (vol. 16), No. 4, pp. 1485-1488. URL: http://dx.doi.org/10.1021/la991161n

[137] Radtchenko, Igor L.; Sukhorukov, Gleb B.; Leporatti, Stefano; Khomutov, Gennady B.; Donath, Edwin and Möhwald, Helmuth (2000): Assembly of Alternated Multivalent Ion/Polyelectrolyte Layers on Colloidal Particles. Stability of the Multilayers and Encapsulation of Macromolecules into

Polyelectrolyte Capsules, J. Colloid Interf. Sci. (vol. 230), No. 2, pp. 272-280. URL: http://www.sciencedirect.com/science/article/pii/S0021979700970681

[138] Caruso, Frank and Möhwald, Helmuth (1999): Preparation and Characterization of Ordered Nanoparticle and Polymer Composite Multilayers on Colloids, Langmuir (vol. 15), No. 23, pp. 8276-8281. URL: http://dx.doi.org/10.1021/la990426v

[139] Tedeschi, C.; Mohwald, H. and Kirstein, S. (2001): Polarity of layer-by-layer deposited polyelectrolyte films as determined by pyrene fluorescence, J Am Chem Soc (vol. 123), No. 5, pp. 954-60. URL: http://www.ncbi.nlm.nih.gov/pubmed/11456630

[140] Wong, John E.; Rehfeldt, Florian; Hänni, Peter; Tanaka, Motomu and Klitzing, Regine v (2004): Swelling Behavior of Polyelectrolyte Multilayers in Saturated Water Vapor, Macromolecules (vol. 37), No. 19, pp. 7285-7289. URL: http://dx.doi.org/10.1021/ma0351930

[141] Izquierdo, A.; Ono, S. S.; Voegel, J. C.; Schaaf, P. and Decher, G. (2005): Dipping versus Spraying: Exploring the Deposition Conditions for Speeding Up Layer-by-Layer Assembly, Langmuir (vol. 21), No. 16, pp. 7558-7567. URL: http://dx.doi.org/10.1021/la047407s

[142] Porcel, Claudine; Lavalle, Philippe; Ball, Vincent; Decher, Gero; Senger, Bernard; Voegel, Jean-Claude and Schaaf, Pierre (2006): From Exponential to Linear Growth in Polyelectrolyte Multilayers, Langmuir (vol. 22), No. 9, pp. 4376-4383. URL: http://dx.doi.org/10.1021/la053218d

[143] Nolte, A. J.; Rubner, M. F. and Cohen, R. E. (2004): Creating effective refractive index gradients within polyelectrolyte multilayer films: molecularly assembled rugate filters, Langmuir (vol. 20), No. 8, pp. 3304-10. URL: http://www.ncbi.nlm.nih.gov/pubmed/15875862

[144] Czikkely, V.; Försterling, H. D. and Kuhn, H. (1970): Light absorption and structure of aggregates of dye molecules, Chemical Physics Letters (vol. 6), No. 1, pp. 11-14. URL: http://www.sciencedirect.com/science/article/pii/0009261470800628

[145] Itzhakov, Stella; Buhbut, Sophia; Tauber, Elad; Geiger, Thomas; Zaban, Arie and Oron, Dan (2011): Design Principles of FRET-Based Dye-Sensitized Solar Cells with Buried Quantum Dot Donors, Adv. Energy Mater. (vol. 1), No. 4, pp. 626-633. URL: http://dx.doi.org/10.1002/aenm.201100110

[146] Periasamy, N.; Doraiswamy, S.; Maiya, G. B. and Venkataraman, B. (1988): Diffusion controlled reactions: Fluorescence quenching of cationic dyes by charged quenchers, The Journal of Chemical Physics (vol. 88), No. 3, pp. 1638-1651. URL: http://link.aip.org/link/?JCP/88/1638/1

[147] Ushiroda, S.; Ruzycki, N.; Lu, Y.; Spitler, M. T. and Parkinson, B. A. (2005): Dye Sensitization of the Anatase (101) Crystal Surface by a Series of Dicarboxylated Thiacyanine Dyes, J. Am. Chem. Soc. (vol. 127), No. 14, pp. 5158-5168. URL: http://dx.doi.org/10.1021/ja044001t

[148] Yum, Jun-Ho; Baranoff, Etienne; Hardin, Brian E.; Hoke, Eric T.; McGehee, Michael D.; Nuesch, Frank; Gratzel, Michael and Nazeeruddin, Md Khaja (2010): Phosphorescent energy relay dye for improved light harvesting response in liquid dye-sensitized solar cells, Energy Environ. Sci. (vol. 3), No. 4, pp. 434-437. URL: http://dx.doi.org/10.1039/B925473K

[149] Vaubel, G.; Baessler, H. and Möbius, D. (1971): Reaction of singlet excitons at an anthracene/metal interface: Energy transfer, Chem. Phys. Lett (vol. 10),

No. 3, pp. 334-336. URL: http://www.sciencedirect.com/science/article/pii/0009261471803020

[150] Pugžlys, Audrius; Hania, P. Ralph; Augulis, Ramunas; Duppen, Koos and van Loosdrecht, Paul H. M. (2006): Cylindrical aggregates of 5,5',6,6'-tetrachlorobenzimida-carbocyanine amphiphilic derivatives: Structure-related optical properties and exciton dynamics, International Journal of Photoenergy (vol. 2006). URL: http://dx.doi.org/10.1155/IJP/2006/29623

[151] Spitz, C. (1999): Excitons in Cylindrical J-Aggregates of Organic Dyes, Dissertation, Physics, Freie Universität Berlin, Berlin.

7.2 Additional Resources

7.2.1 Calculation of Förster-radii

The Förster radii are calculated according to formula (2-36) and 2-37), namely,

$$R_0^6 = \frac{\kappa^2 \Phi_D}{n^4} \cdot C_0 = \frac{\kappa^2 \Phi_D}{n^4} \cdot \frac{9000 \cdot \ln(10)}{128 \pi^5 N_A} \int_0^\infty f_D(\nu) \varepsilon_A(\nu) \nu^{-4} d\nu \qquad \text{(eq. 7-1)}$$

Where $\mathbf{f_D}$ is the fluorescence spectrum of the donor, normalized to the total intensity, ε_A is the absorbance of the acceptor in mol·l^{-1}·cm^{-1}, $\boldsymbol{\nu}$ is the wavenumber in cm^{-1}, and $\mathbf{N_A}$ is Avogadro's number. The spectra are interpolated to equidistant values $\boldsymbol{\nu}$ with step size $\Delta\boldsymbol{\nu}$ = 2 cm^{-1}. The integral was then evaluated by direct summation which is sufficiently accurate.

The geometry factor $\boldsymbol{\kappa^2}$ was taken to for the case of static molecules with total random orientation, which is $\boldsymbol{\kappa^2}$ = 0.476 [79].

The Quantum efficiency of the donor $\boldsymbol{\Phi_D}$ and the refractive index of the environment $\mathbf{n_D}$ are less well known. Although the quantum efficiencies can be taken from literature values, the error may by rather high. Fortunately, due to the power of 1/6 the dependency on this quantity is weak. For that and because of technical reasons, $\boldsymbol{\Phi_D}$ was not measured directly.

The refractive index of the solvent, mostly water, is $\mathbf{n_D}$ = 1.33. However, the donor (or acceptor) molecules are embedded into a matrix of polyelectrolyte and dye. The refractive index of polyelectrolyte multilayers as measured values are reported between 1.44 for layers swollen with water [140], 1.46 for sprayed films [141,142], and 1.55 for slightly different materials [143]. Additionally, the chromophores within the J-aggregate are within an environment that in total consists of π-electron systems. For that case, a dielectric constant of $\boldsymbol{\varepsilon}$ = 2.5 was postulated [144] giving a refractive index of $\mathbf{n}$ = 1.58. In conclusion, a reasonable value for the refractive index will be $\mathbf{n_D}$ = 1.5 ± 0.1.

In the following, $\mathbf{R_0}$ is calculated under the assumption of certain ranges of $\boldsymbol{\Phi_D}$ and $\mathbf{n_D}$.

7.2.2 Spectral overlap of rhodamin B and aggregate

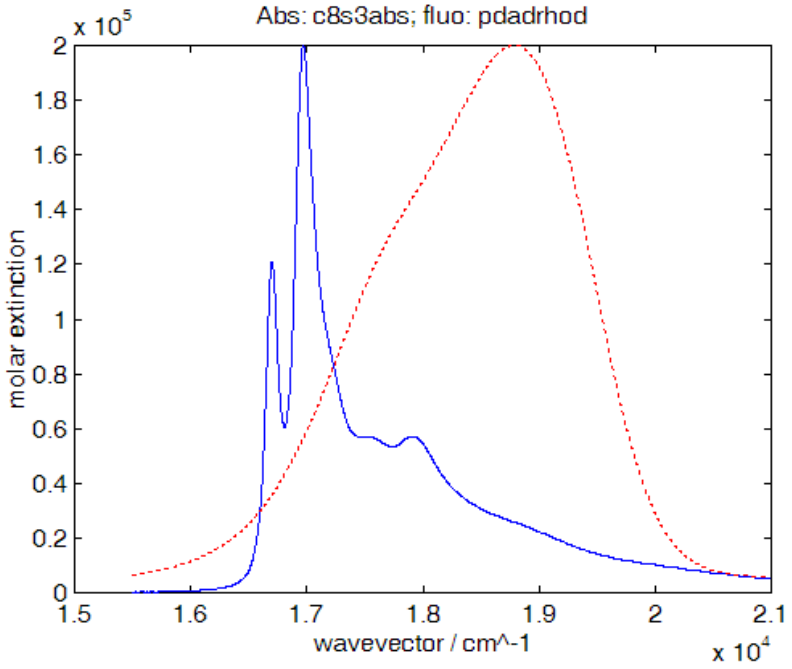

Figure 7-1:
Spectra used for calculation of the overlap integral J: normalized fluorescence emission of rhodamin B on PDADMAC, blue emission (dotted line, red) and absorption spectrum of C8S3 J-aggregates (solid line, blue). The absorbance is given in units of the molar extinction (l mol^{-1} cm^{-1}), the fluorescence is normalized to the maximum of the absorption for better presentation. The product of the spectra weighted by $1/\nu^{-4}$ is shown in the next figure.

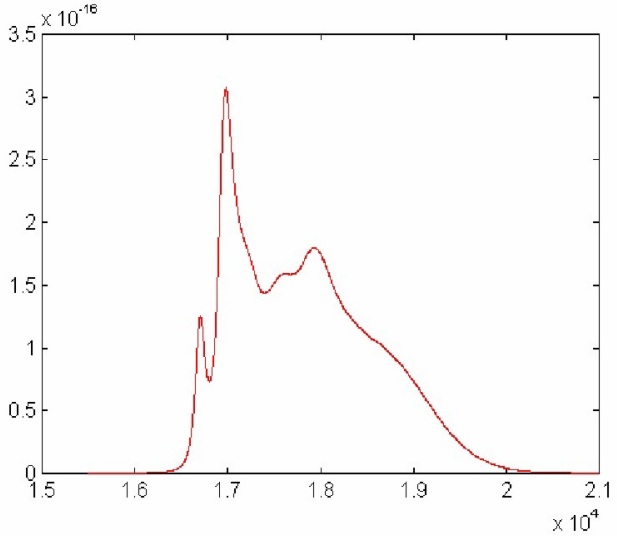

Figure 7-2:
The product of the spectra weighted by $1/\nu^{-4}$.

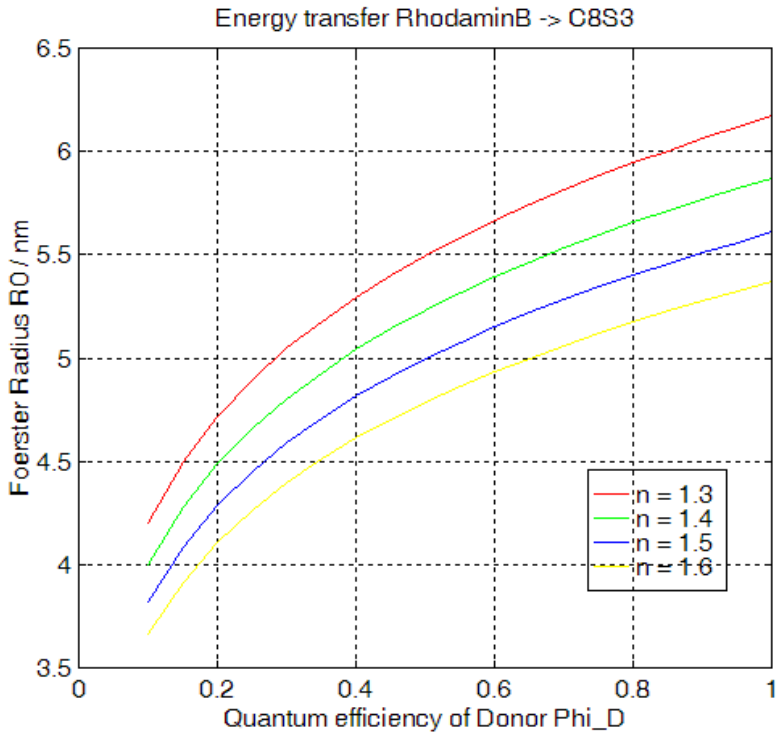

Figure 7-3:
Förster radius R_0 for various values of refractive index, drawn versus the quantum efficiency of the donor molecule. Realistic values are given by Φ_D = 0.2 ... 0.7 and n_D = 1.4 ... 1.6.

Resume:

$$\mathbf{C_0} = 3.3086 \cdot 10^{-37}$$

For the interval of $\mathbf{\Phi_D}$ = 0.2 ... 0.7 for rhodamin B and $\mathbf{n_D}$ = 1.4 ... 1.6 we obtain:

$$\mathbf{R_0} = 4.1 \ldots 5.5 \cong 4.8 \pm 0.7 \text{ nm}$$

7.2.3 Spectral overlap of aggregate and Alexa631

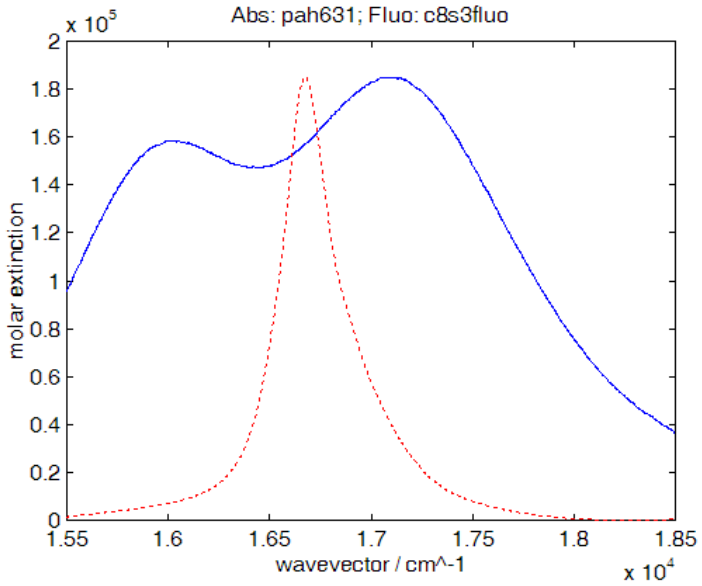

Figure 7-4:
Spectra used for calculation of the overlap integral J: normalized fluorescence emission of C8S3 (dotted line, red) and absorption spectrum of Alexa631 dye (solid line, blue). The absorbance is given in units of the molar extinction (l mol^{-1} cm^{-1}), the fluorescence is normalized to the maximum of the absorption for better presentation.

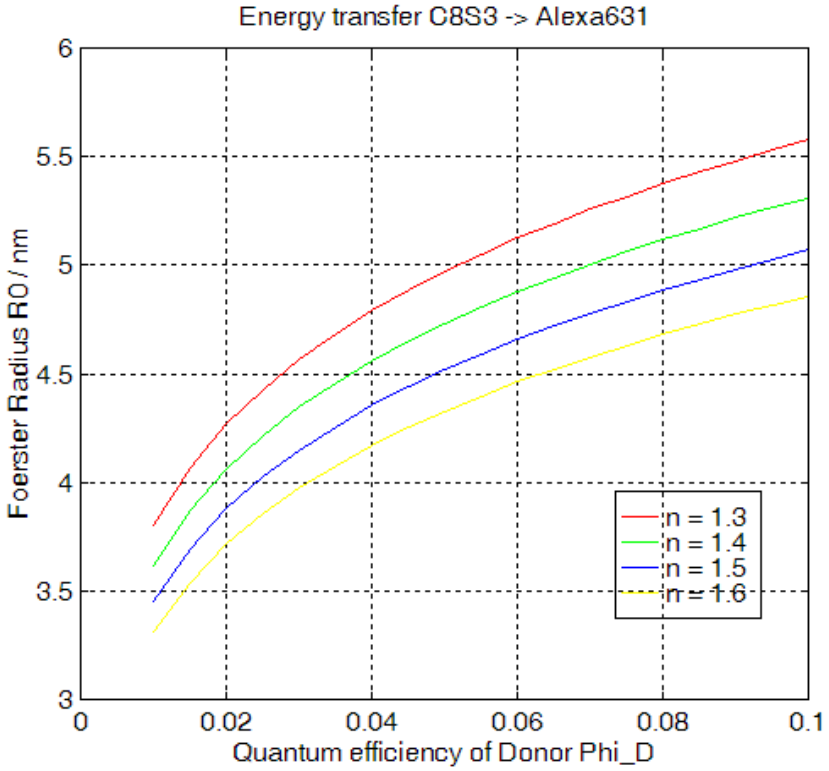

Figure 7-5:
Förster radius R_0 for various values of refractive index, drawn versus the quantum efficiency of the donor molecule. Realistic values are given by Φ_D = 0.02 ... 0.05 for C8S3 aggregates and n_D = 1.4 ... 1.6.

Resume:

$$\mathbf{C_0} = 1.8089 \cdot 10^{-36}$$

For the interval of $\mathbf{\Phi_D}$ = 0.02 ... 0.05 for C8S3 aggregates and $\mathbf{n_D}$ = 1.4 ... 1.6 we obtain:

$$\mathbf{R_0} = 3.7 \ldots 4.7 \cong 4.2 \pm 0.5 \text{ nm}$$

7.2.4 Numerical simulation of transfer efficiencies

The energy transfer between dye labels in the external shell and the tubular J-aggregate were simulated numerically. A simple model was used where the cyanine dyes of the tubular J-aggregate are placed on a cylindrical mesh surface and the dye labels of the polyelectrolyte shell are randomly distributed within a shell of given thickness. For every dye label the Förster transfer rate to all cyanine dyes is calculated and these rates are summed over the whole aggregate. For the purpose of visualization, the intensity of the aggregate emission is calculated from the transfer efficiencies and indicated by colours.
In more detail the model is built as described in the following paragrphs.

7.2.4.1 Modelling of the aggregate

Two intercalated tubes as a model for the double-layer wall of the aggregate is taken as a base. It is assumed that the double layer wall contains 108 Molecules per nanometer length, where 2/3 of them belong to the outer wall and 1/3 belong to the inner wall. The radii of the tubes are 13/2 nm and 6.5/2 nm, respectively. The transition dipoles of the molecules are assumed to be located within these tubes.
Mathematically, a tube is build from a rectangular mesh such that the mesh density equals the physical area density of dye molecules in the inner or outer wall, respectively. This model does not reflect any orientational order of the dye molecules as present in the real system. The mesh density is adjusted using a mesh size of 1 nm along the *z*-direction and an angular distance of $\Delta\theta = 360/\mathbf{N_{tub}}$ along the perimeter, where $\mathbf{N_{tub}}$ denotes the number of molecules per nm length.

7.2.4.2 Distribution of acceptor molecules

The acceptor molecules are distributed homogeneously within a shell of thickness $\mathbf{D_{shell}}$ between radii $\mathbf{r_a}$ and $\mathbf{r_b}$ around the outer tube of the aggregate. The random distribution is generated from uniformly distributed random numbers **RAND** of the interval [0,1]. The distribution of the radial component ρ is then calculated by:

$$\rho = \sqrt{r_a^2 + \left(r_b^2 - r_a^2\right) \cdot RAND} \qquad \text{(eq. 7-2)}$$

These are allocated to uniformly distributed values of angle φ and axial distance **z**:

$$\varphi = 2\pi \cdot RAND \qquad \text{(eq. 7-3)}$$

$$z = z_{\max} \cdot RAND \qquad \text{(eq. 7-4)}$$

The resulting positions of the acceptor molecules in the polyelectrolyte shell are then given by:

$$D = \left(\rho \cdot \cos(\varphi), \rho \cdot \sin(\varphi), z\right) \qquad \text{(eq. 7-5)}$$

7.2.4.3 Calculation of transfer efficiencies

For the evaluation of the normalized transfer rate between a dye from the tubular aggregate and a dye within the shell the Förster radius is taken as a measure. This radius was used as calculated in section 7.2.4.1 under the assumption that the orientational factor, the refractive index, and the quantum efficiency of the respective donor are included. The transfer rate used here is given by dimensionless number, i.e. it is measured in units of the donor lifetime:

$$k_f = \left(\frac{R_0}{r}\right)^6 \qquad \text{(eq. 7-6)}$$

This rate is calculated for every lattice point on the cylindrical aggregate surface towards all acceptor molecules and from the sum of the rates the transfer efficiency of an aggregate molecule is given by:

$$\eta = \frac{1}{1 + \frac{1}{k_f}} \qquad \text{(eq. 7-7)}$$

From these efficiencies the normalized luminescence intensity is given by 1 - η and this quantity is drawn in false colours on top of the cylindrical aggregate surface. For better visualisation, the mesh grid is interpolated.

The total fluorescence of the aggregates in presence of acceptors $\mathbf{I_{D+A}}$ compared to the intensity without acceptors $\mathbf{I_D}$ is then simply evaluated by the average of 1 - $\langle\eta\rangle$ for a large amount of molecules. Here, typically aggregates with a length of 100 nm are simulated, giving approximately 1000 acceptor molecules and 6400 aggregate molecules. These numbers deliver a statistical significance better than 1%, which is sufficient for the investigations here.

7.2.4.4 Aggregate as donor vs. aggregate as quencher

In case where donor molecules are placed in the shell around the aggregate, the calculation is done exactly with the same formalism. In this case, the quenching of the donors is calculated at the position of the aggregate surface. The mean transfer efficiency then is again calculated by the same averaging procedure and delivers the mean quenching efficiency of the donor molecules. The images then provide a mapping of areas where to the energy is transferred most efficiently.

7.2.5 MATLAB code for numerical simulation

```
% fretcyl.m
%
% code to simulate Foerster Resonance Energy Transfer (FRET)
% from tubular J-aggregate to acceptor molecules in surrounding
% polyelectrolyte shell.
%

% ----- Geometrical parameters
%     all Dimensions in nm

% R0 is Foerster Radius, contains all other constants
%    (quantum yield, geometrical factor, refactive index)

R0=4.2;     % as obtained for C8S3 -> Alexa631
R02=R0*R0;  % we need square of it ...

dlabel=10;  % label density, as acceptors per nm aggregate length
Nouter=round(108*2/3);  % cyanine dyes in outer aggregate tube
Ninner=round(108/3);    % cyanine dyes in inner aggregate tube
Ntub=Ninner;            % use inner tube here, comment otherwise
% Ntub=Nouter;          % use outer tube here, comment otherwise

zmax=20;    % extension of cylindrical aggregate along z
deltaz=1;   % mesh width

Rta=13/2;   % radius of aggregates, outer tube
Rti=6.5/2;  % radius of aggregatse, inner tube

Ra=Rta;           % inner radius of PE shell = radius of outer tube
Dshell=2.5;       % thickness of shell

%R=Rti;           % use inner tube, comment otherwise
 R=Rta;           % use outer tube, comment otherwise
Nd=dlabel*zmax;   % total number of acceptor molecules in shell


% ----- Create cylinder surface as a mesh grid

dth=360/Ntub;
th=[0:dth:360];   % dye density is adjusted by delta_theta
th=th';           % we want column vector
th=th.*pi/180;    % transform degree to rad

xx=[]; yy=[];  zz=[];   % matrix xx, yy, zz contain the coordinates
of the mesh points
zdummy=ones(size(th));
Rc=R.*cos(th);
Rs=R.*sin(th);

for z=0:deltaz:zmax,
  xx=[xx,Rc];
  yy=[yy,Rs];
  zi=zdummy.*z;
  zz=[zz,zi];
end;


% ----- Create random positions of acceptor molecules
```

```
ra=Ra+0.2;  % start at distance 0.2 nm away from outer tube of
aggregate
rb=Ra+Dshell;     % end at outer radius of shell
Dd = sqrt(ra*ra+(rb*rb-ra*ra)*rand(Nd,1));     % gives distribution
according to r*D(r)dr

Dphi=rand(Nd,1).*(2*pi);                  % gives uniform
distribution along phi
Dxy=[Dd.*cos(Dphi), Dd.*sin(Dphi)];
Dz=zmax.*rand(Nd,1);                      % gives uniform
distribution along z


% ----- Calculate transfer efficiencies

kf=zeros(size(xx));                 % one efficiency for every mesh
point on the aggregate surface
for Di=1:Nd,                        % loop over all donors
  kfi=[];                     % efficiency for one acceptor
  rho=[Rc-Dxy(Di,1), Rs-Dxy(Di,2)]; % distance acceptor to all dyes
in a circle (xy-plane)
  for z=0:deltaz:zmax,
      r=[rho,zdummy.*(z-Dz(Di))];   % distance including z
      r2=r.*r;
      r2=(sum(r2'))';               % now square of distance
      kfii=(R02./r2).^3;            % transfer-rate
      kfi=[kfi,kfii];               % kfi is mapping of rates on tube
mesh for acceptor i
  end;      % z loop
  kf=kf+kfi;                        % kf is mapping of rates of all
acceptors
end;  % Di loop

eta=1./(1+1./kf);             % eta is now mapping of transfer
efficiency
Inorm=ones(size(eta))-eta;          % Inorm is normalized intensity
of aggregate (=donor) emission


% ----- Calculate mean value of transfer efficiency
% mean efficiency: average along the tube!
% sum all eta values of every lattice point (= dye)

[n,m]=size(eta);
eta_avg=sum(sum(eta))/(n*m);
eta_avg=eta_avg*100                 % percentage


% ----- Create figures

% creat inverse colormap of hot: --> "coal"

colormap(hot);
cc=colormap;
nn=65-[1:64]';
[snn,nni]=sort(nn);
coal(:,:)=cc(nni,:);


figure(1);        % delivers top view (xz-plane)
whitebg('w');
colormap(coal);
surf(zz,xx,yy,eta)
```

```
%shading interp
colorbar
axis('equal')
view(2)
title ('Transfer efficiency eta (Top View)');
xlabel('z / nm');
ylabel('x / nm');
zlabel('y / nm');
title('Transfer efficiency eta');
hold on
plot3(Dz,Dxy(:,1),Dxy(:,2),'ob');
hold off
shading interp

figure(2);        % delivers 3D view of efficiency
whitebg('w');
colormap(coal);
surf(zz,xx,yy,eta);
colorbar;
axis('equal');
view(3);
title ('Transfer efficiency eta (3D View)');
xlabel('z / nm');
ylabel('x / nm');
zlabel('y / nm');
hold on;
plot3(Dz,Dxy(:,1),Dxy(:,2),'ob');
hold off;
shading interp;

figure(3);        % delivers view on front edge, to see acceptor
distribution
whitebg('w');
colormap(jet);
surf(zz,xx,yy,eta)
colorbar
axis('equal')
view([90,0]);
title ('Front edge');
xlabel('z / nm');
ylabel('x / nm');
zlabel('y / nm');
hold on
plot3(Dz,Dxy(:,1),Dxy(:,2),'ob');
hold off
shading interp

figure(4);        % like Figure(2), but donor intensity
whitebg('w');
colormap(hot);
surf(zz,xx,yy,Inorm);
colorbar;
axis('equal');
view(3);
title ('I/I_0  (3D View)');
xlabel('z / nm');
ylabel('x / nm');
zlabel('y / nm');
hold on;
plot3(Dz,Dxy(:,1),Dxy(:,2),'ob');
hold off;
shading interp;
```

7.3 Acknowledgment

First of all I would like to thank Dr. Stefan Kirstein for his endless patience answering my questions and giving me advices on all those innumerable versions of my thesis, for the fruitful discussions and for the opportunity to participate on this project – the wonderful amphiphilc J-aggregates.

Prof. Rabe and Prof. Möhwald own my honest thanks for funding me all over this time and of course for the great opportunity to work in their groups.

The group of Prof. Rabe was a pleasant environment for scientific work and social life. Constans Weber, Ai Min, Sebastian Schön, Manuel Gensler, Liang Hua and Dr. Nikolai Severin have been always interesting discussion partners in physics and chemistry. Lothar Geyer additionally found always time for my IT-issues and helped my to stay connected with HU, FU, TU and MPI. Evi Poblenz, caring for the lab-equipment, was seriously supporting me, with providing master-solutions and having always at least one “proper” cuvette in spare. Philipp Lange, Vitalij Scenev, Wei Zhuang and Martin Dorn constantly had open ears for my thoughts on physics, world-politics and life in general and therefore own my very special thanks.

Dr. Christoph Böttcher instructed me on handling a TEM and how to understand the obtained images. For procuring these skills and for the continuative discussions I gratefully thank him. Jürgen Gatzmann constantly supported my work with cryo-TEM and helped me out of every single pitty mistake I made on the CM12. Hans von Berlepsch, Kai Ludwig, Boris Schade and Andrea Schulz were always available for urgent questions on TEM and TEM-sample preparation.

Dr. Puls and Prof. Henneberger I would like to thank for the opportunity to achieve data of time-resolved measurements from their lab.
Prof. Dr. Andre Laschewsky from University of Potsdam and Dr. Frank Mallwitz from AOKIN I gratefully thank for providing me dye-labelled polyelectrolytes, that helped me perform the core of my thesis.

I would like to thank my friends for their support and grasp during the “hot-phase” of my thesis, especially I would like to thank Kristijan Posilovic and Wiebke Fischer for reading my thesis; Claudia Garman, Manuela Klaus and Christoph Zömisch for magically conjure a smile on my face, though period was sad; Kai Hodek and Karsten Schork for motivate me to continue and move on, though aspects are depressing.

Overall, I would like to thank my father, for all his support, knowledge and wisdom that inspired me to head for a goal, but always keeping a view above the rim.